Alma Mater Studiorum – Università di Bologna

DOTTORATO DI RICERCA IN
MECCANICA E SCIENZE AVANZATE DELL'INGEGNERIA

Ciclo XXXII

Settore Concorsuale: 09/A1

Settore Scientifico Disciplinare: ING-IND/04

Crack growth in adhesively bonded joints under quasi-static and fatigue loading

Presentata da: Nicola Zavatta

Coordinatore Dottorato

Prof. Marco Carricato

Supervisore

Prof. Enrico Troiani

Esame finale anno 2020

Abstract

Adhesively bonded joints are attracting increasing interest in the aerospace industry. However, incomplete knowledge of fatigue crack growth in adhesive bonds is a major concern to their application. This thesis investigates several aspects of crack growth in adhesively bonded joints. The influence of adhesive thickness on fatigue crack growth under mode I loading was addressed by a combination of experimental tests and numerical simulations. Increased crack growth was found in thicker specimens. This was explained as a result of increased energy available for crack growth in thicker adhesives, while the crack growth resistance was found not to be affected by the thickness. Formation of micro-cracks promoted by increased plasticity is thought to be the source of increased crack growth. Cohesive zone models were applied to the study of mode I and mode II quasi-static crack growth. A strong dependence on the input parameters was observed. In particular, the effect of viscous regularization on the solution was investigated. A proof of consistency of the viscous solution was proposed. It was shown that a low value of viscosity is needed to obtain consistent results. Finally, disbond arrest in bonded GLARE was studied by means of fatigue tests on bolted cracked lap shear specimens. The experiments evidenced a moderate decrease of the crack growth rate near the bolt. This was further investigated by numerical computations, which showed a significant change of the strain energy release rate around the bolt from mixed mode I/II to almost pure mode II. Outside this region, good predictions of the fatigue crack growth rate could be obtained by a combination of existing models from the literature. Extensive adherent cracking was observed, which led to the conclusion that crack arrest in GLARE comes from a balance of adhesive crack growth retardation and adherent cracking.

ii

Ringraziamenti

Ringrazio innanzitutto il mio supervisore, Prof. Enrico Troiani, per l'opportunità che mi ha offerto accettandomi come suo dottorando. Vorrei spendere un ringraziamento particolare nei suoi confronti per aver condiviso con me ben più di quanto i semplici doveri accademici richiedano.

Ringrazio i miei genitori per la loro costante presenza e la fiducia nei miei confronti.

Ringrazio infine la mia ragazza, Claudia, che mi ha supportato fin dal primo giorno del dottorato e che, in ultimo, ha contribuito personalmente alla correzione di questa tesi.

A voi dedico i miei ringraziamenti più sentiti.

Contents

List of Figures

List of Tables

Chapter 1

Introduction

Adhesively bonded joints have gained increasing interest in the aerospace industry. Their capability to offer significant weight reduction compared to conventional riveted joints makes them much attractive for a sector in which words like 'green' and 'light' are being increasingly used. Moreover, adhesive bonds allow joining of components without the need for holes and pins, which come at the cost of high stress concentration factors and are detrimental to fatigue life. For instance, a survey of serious aircraft accidents involving fatigue published in 1984 reported that fasteners and holes alone account for about 40% of the total crashes, being respectively the first and second most common initiation sites of fatigue cracks [1]. Even though these figures should be put into perspective, as the advent of damage tolerant design has resulted in dramatic improvements on safety, they give a measure of how critical proper joint design is for structural integrity.

1.1 Thesis motivation

As good as they might be, adhesively bonded joints are not immune to fatigue: geometric discontinuities associated to thickness changes may well result in stress concentrations at the edges. Even worse, incomplete adhesion could occur during the manufacturing process in bonded and co-bonded structures, which substantially impairs the joint's capability to withstand external loads. At present, non-destructive inspection techniques can detect the presence of disbonded areas within the component, but are not able to detect so-called weak bonds, i.e. bonds in which incomplete adhesion does not produce a distinct interface layer [2]. From the certification's point of view, this means that adhesive bonds are currently acceptable in aircraft structures only on the condition that disbonding does not grow to the point

that critical design loads can not be sustained.

This indeed poses the main questions of this thesis: "How effectively can we predict crack growth in adhesive bonds? And to which extent can existing prediction methods be applied to situations different from the one they were developed for?"

Pascoe [3] already pointed out that most of the existing works on adhesive bonds focus on prediction methods more than on understanding the causes of fatigue disbonding and deriving prediction methods accordingly. Put it differently, many studies on fatigue crack growth in adhesive bonds are phenomenological, i.e. based on empirical observation of the specific phenomenon, rather than being based on knowledge of the mechanisms implied.

In present author's view, this has a strong practical consequence: knowledge on fatigue in adhesive bonds is fragmentary, with many different methods applied to problems which should indeed be strictly interconnected to one another. Incomplete knowledge of how fatigue crack growth varies according to the fracture mode is a good example of this.

1.2   Thesis objectives

This research started in continuation of a previous work investigating the effect of thickness on fatigue crack growth in adhesively bonded joints [4]. Experimental evidence suggested an effect opposite to that reported in other works in the literature, i.e. increased adhesive thickness resulted in faster crack growth. Thus, the first question that was addressed was what mechanism is responsible for the effect of thickness. In particular, we investigated how varying the thickness affects plasticity in the adhesive and how this relates to the observed thickness effect.

Answering this question involved numerical modelling of the fracture region. Further modelling of the crack propagation resulted in the development of a cohesive zone model for mode I and mode II crack growth under quasistatic conditions. By comparing the numerical results to the experimental ones, it was apparent that the input parameters of the model play a key role in the computed output. In spite of this, only some of these parameters have received attention in the literature. Most remarkably, only a few studies were found, dealing with the effect of the viscous numerical scheme used to stabilize the solution on the solution itself, despite it being widely adopted in finite element solvers. This motivated a more in-depth study of the effect of viscous regularization on the numerical solution of a cohesive model.

Finally, we investigated the effect of a bolted disbond arrest feature on fatigue crack growth in bonded cracked lap shear specimens made of GLARE.

While the material was different from that used until that point, e.g. Al 2024 aluminium alloy, this activity was motivated by the opportunity to extend our study of fatigue crack growth to loading conditions which are more representative of those encountered in aerospace applications.

1.3 Thesis outline

The thesis is structured as follows:

Chapter 2 investigates the effect of adhesive thickness on fatigue crack growth under mode I loading.

Chapter 3 deals with the application of cohesive zone models to computation of crack growth in mode I and mode II. The influence of viscous regularization on the numerical solution is also discussed.

Chapter 4 presents the study of disbond arrest features in bonded GLARE.

Chapter 5 concludes the thesis by summarizing the main findings of the research.

Appendix A contains a proof of consistency of the viscous solution.

References

1. Campbell, G. S. & Lahey, R. A survey of serious aircraft accidents involving fatigue fracture. *International Journal of Fatigue* **6,** 25–30 (1984).

2. Kruse, T., Körwien, T., Ruzek, R., Hangx, R. & Rans, C. *Fatigue behavior and damage tolerant design of bonded joints for aerospace application on Fiber Metal Laminates and composites* in *29th ICAF Symposium - Nagoya* (2017), 7–9.

3. Pascoe, J. A. *Characterisation of Fatigue Crack Growth in Adhesive Bonds.* PhD thesis (Delft University of Technology, 2016), 147. `http://doi.org/10.4233/uuid:ebbf552a-ce98-4ab6-b9cc-0b939e12ba8b`.

4. Zavatta, N. *Influence of adhesive thickness on adhesively bonded joints under fatigue loading* Master thesis (Università di Bologna, 2015). `http://amslaurea.unibo.it/9713/1/zavatta%7B%5C_%7Dnicola%7B%5C_%7Dtesi.pdf.pdf`.

Chapter 2

Influence of adhesive thickness on fatigue crack growth of adhesively bonded joints

This chapter deals with the topic of fatigue disbonding in metallic bonded joints. In particular, we discuss the influence of the adhesive thickness on fatigue disbonding of aluminium-epoxy specimens in mode I. First the issues related to the study of disbonding are briefly introduced and contextualized within a literature review on this subject. Then, the findings of our study are presented and discussed critically by comparison with existing results. Finally, we put forward an hypothesis to explain the observed results.

Part of the work presented here was carried out in collaboration with Dr. John-Alan Pascoe and Prof. René Alderliesten of TU Delft, that the author gratefully acknowledges. No criticism should be directed at them for any of the opinions expressed by the present author.

2.1   Introduction

Adhesive bonding has seen an increasing diffusion in weight-critical applications. Although bonded joints allow to reduce the stress concentrations compared to riveted or bolted structures, they are susceptible to cracking along the bondline. This can occur either in the form of a crack developing inside the adhesive layer, i.e. cohesive failure, or disbonding at interface between the adhesive and the adherent, i.e. adhesive failure. The presence of a crack propagating in a thin layer surrounded by bulk material is somewhat different from crack growth in metals and bears some similarities to the phenomenon of delamination in composite materials.

Much effort is still needed to understand the fatigue crack growth behaviour in bonded joints. Many prediction methods have been proposed in the past, but these are mostly based on empirical correlations rather than an understanding of the physics [1]. That physical understanding of the fatigue phenomenon is more than a mere speculation is also debated in Alderliesten et al. [2], with reference to fatigue in fibre-reinforced polymers.

Pascoe et al. [3, 4] have suggested that more insight into the underlying physics can be gained by measuring the dissipation of strain energy during the crack growth process. They showed that correlating the crack growth rate to the measured strain energy dissipation per cycle ($\frac{\mathrm{d}U}{\mathrm{d}N}$), rather than to the strain energy release rate (SERR), could account for most of the effect of the stress ratio. A small stress ratio effect was still observed. It was suggested that this might be caused by non-linearity of the force-displacement curve [4]. However, further examination has shown that the force-displacement curve remains linear throughout the fatigue test [5]. An alternative hypothesis is that the observed difference in energy dissipation at different stress ratios, for a given crack growth rate, is caused by differences in the stress state and amount of plasticity at the crack tip. It is known from previous works, e.g. [6–10], that the adhesive thickness affects these parameters and thereby the fracture toughness.

Various studies on the effect of adhesive thickness on fatigue crack growth have been published [11–19]. While these works identify the effect of thickness, a clear explanation of this effect is still lacking.

Thus we investigated the effect of different bondline thicknesses on the fatigue disbonding behaviour in FM94 epoxy adhesive, as a way of gaining more understanding of the effect of the crack-tip plastic zone on crack growth behaviour. This is done by comparing results from crack growth experiments on Double Cantilever Beam (DCB) specimens with different adhesive thicknesses with numerical modelling to determine the amount of plasticity. Before presenting the results of this work, a review of the existing literature on the effect of adhesive thickness on crack growth is discussed.

2.2   Literature review

Several studies on the effect of adhesive layer thickness on fatigue crack growth are available in the literature. A concise review of the effect of thickness on fracture (under quasi-static load) has been provided by Azari et al [11].

In general, these works report that higher thickness results in lower fatigue crack growth rates and also higher fracture toughness [11–13, 15–17,

19], which is ascribed to the effect of constraint (provided by the adherends) on the plastic zone size in the adhesive layer. Removal of constraint (by increasing thickness) is thought to result in more plasticity, which then increases the crack resistance, thus reducing the fatigue crack growth.

In contrast, Krenk et al. [14] reported no effect of thickness in a single-lap joint with a two-part cold-cured epoxy (9323, manufactured by 3M). Schmueser [18] found an increase of fatigue crack growth rate for increasing adhesive thickness in a Cracked Lap Shear (CLS) specimen, with a one-part epoxy (Ciba-Geigy Araldite XB-3131). In this case it should be noted that the loading mode-mix was different for the different adhesive thicknesses.

Chai [13] investigated two brittle epoxies (Namco 5208 and Hercules 3502) and one tough resin (PEEK) and found different behaviours. For the brittle epoxies the fracture toughness increased for increasing thickness. For PEEK, however, at low thicknesses ($t < 0.038$ mm) the fracture toughness first decreased with increasing thicknesses, and only at higher thicknesses did the toughness increase with increasing thickness.

Detailed studies explaining how bond line thickness affects fracture have been mainly confined to quasi-static loading. Nevertheless, these studies may also shed light on the fatigue behaviour. Kinloch and Shaw [6] identified that the effect on fracture toughness is non-monotonic. Up to an optimum thickness t_{m} the fracture toughness G_{Ic} increased with increasing thickness. Above t_{m}, an increase of the adhesive thickness resulted in a reduction of the fracture toughness.

Kinloch and Shaw explained this behaviour with the work of Bascom et al. [7] and Wang et al. [8], who studied the plastic zone and the stress fields ahead of the crack tip. Based on those works, Kinloch and Shaw argued that for $t < t_{\mathrm{m}}$ the adherends restrict the full development of the plastic zone. This reduces the capacity of the adhesive to dissipate energy by mechanisms other than fracture, resulting in a lower fracture toughness. The lower t, the greater the restrictive effect of the adherends, and therefore the lower the fracture toughness will be. For $t > t_{\mathrm{m}}$, the dominant effect according to Kinloch and Shaw is the amount of constraint in the adhesive. As the thickness increases, the degree of constraint reduces. The reduction in constraint causes the plastic zone to extend less far ahead of the crack tip. This reduces the volume of the plastic zone, resulting in a reduction of fracture toughness.

These constraint effects were further investigated by Daghyani et al. [9], eventually leading Yan et al. [10] to propose a model involving two different mechanisms. Yan et al. propose that a reduction in thickness increases the constraint on the adhesive, resulting in a reduction of the plastic zone size, and therefore a decrease of the fracture toughness. This is the primary

mechanism when $t < t_\mathrm{m}$. When the thickness is greater than the optimum thickness, an increase in thickness will allow increased crack tip blunting to occur, resulting in increased void-crack coalescence, and therefore a lower fracture toughness.

In contrast to the findings of Kinloch and Shaw and Yan et al., a recent study by Azari et al. [20] found no evidence of an optimum thickness, reporting a linear increase of the toughness with adhesive thickness for all the tested thicknesses. This suggests that the Kinloch-Shaw and Yan et al. models may be material dependant. It is also possible that for the adhesive tested by Azari et al. the optimum thickness is larger than the maximum value investigated.

Pardoen et al. [21] investigated the effect of thickness based on a work of fracture approach. Their findings were in line with the models of Kinloch-Shaw and Yan et al., but did highlight a number of important considerations. First of all, Pardoen et al. performed a fractographic investigation, which identified that the fracture mechanisms (for the adhesive they investigated) takes place on a length scale on the order of 100-200 μm. This means that, at low adhesive thicknesses, not only the plastic zone but also the fracture mechanisms themselves may be constrained by the adherents. Furthermore, Pardoen et al. pointed out that the intrinsic work of fracture of the adhesive, which is not affected by the plasticity, may itself also depend on the local stress state, and thereby on the adhesive thickness.

The works mentioned above all quantified the effect of thickness on the fracture toughness, i.e. the resistance to crack growth. However, the adhesive thickness might also affect the driving force for crack growth. That is, for the same applied far-field loading, a different thickness might result in a different driving force. Chiu and Jones [22] investigated the case of an undamaged bond, and found that the adhesive thickness affected the stress distribution. Gleich et al. [23, 24] and Lenwari et al. [25] looked specifically at the stress intensity factor at the bi-material interface at the end of the bondline and found that the stress intensity factor increased for increasing adhesive thickness. It is unclear whether these results also hold for a cohesive crack within the adhesive layer. Nevertheless, they could help explain the apparent decrease of fracture toughness for increasing adhesive thickness reported in the papers mentioned above. After all, the fracture toughness there was measured based on the applied load. So, an increase in crack driving force for the same applied load would produce the impression of a lowered fracture toughness.

From the available studies one can conclude that in general, up to a certain optimum, a greater adhesive thickness will produce more plastic deformation, and as a result lower crack growth rates. The precise effects will

however depend on the adhesive and geometry under consideration.

Compared to most of the literature (with the exception of Chai [13] and to a certain extent also Azari et al. [11] and Mall and Ramamurthy [16]), this research focused on lower thicknesses, considering a maximum thickness on the order of 0.3 mm.

2.3 Materials

For this research double cantilever beam specimens consisting of two Al 2024-T3 arms bonded with FM94K.03AD epoxy film adhesive were used. This adhesive comes in the form of a film supported by a polyester carrier mat, which allows for better control of the thickness. Three types of specimens with different nominal adhesive thicknesses were investigated.

As a baseline, fatigue crack growth data from specimens containing a single layer of adhesive film with polyester carrier were used. This data had been collected previously and published by Pascoe as part of his PhD thesis [26]. In the online datasets [5] these are referred to as series B through E. In the following they will collectively be denoted as 1l specimens, as they contained 1 layer of adhesive.

Two further types of specimens were manufactured. One type contained two layers of adhesive film (both with polyester carrier) and was denoted series G. Here these samples will collectively be referred to as 2l specimens. The third type of specimens contained approximately 1.5 layers of adhesive film and was called series H. Here we will refer to them as the 1.5l specimens. Having '1.5 layers' of adhesive film was achieved during manufacturing by making an adhesive layer consisting of one layer of FM94K.03AD adhesive with carrier and then placing strips of FM94-U-06 adhesive film without carrier on top of this, over approximately half the surface area. This is shown in Figure 2.1. During curing the epoxy without carrier will flow, resulting in an adhesive layer thickness in between that of the single and the double layer specimens.

Accurate thickness control cannot be achieved with this manufacturing strategy. However, the adhesive thickness of each 1.5l and 2l specimen was measured before testing, in order to take into account the expected thickness variation. Another concern with this manufacturing strategy is that the different adhesive layers will not bond. Figure 2.2 illustrates two pictures of the adhesive bondline in a 1.5l specimen and in a 2l one, which were used to measure the effective thickness. The pictures were taken from the side of the specimens with an optical microscope with 10x magnification factor. They clearly show that the FM94-U-06 strips had indeed flowed enough during
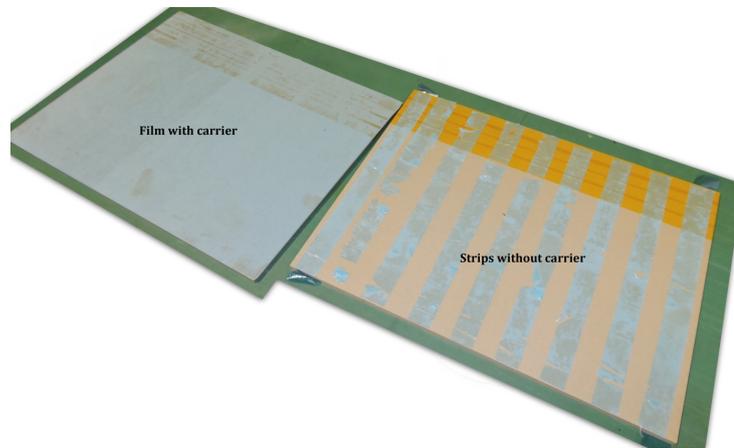
Figure 2.1: Manufacturing of 1.5l specimens. The plate on the left is entirely covered by a sheet of epoxy film, the plate on the right is covered with strips of adhesive over approximately half of its surface area. The plates are then placed on top of each other, with the adhesive in the middle of the resulting stack [26].

the bonding process to produce a uniform thickness layer, confirming that the layers bonded indeed during manufacturing. The presence of a second carrier mat in the 2l specimens might also be expected to influence the results. However, it had previously been shown by Bürger that in mode I the effect of a single carrier mat is negligible [27]. In the present research no results were found that suggested the second mat had an influence, but this could be further investigated in future research.

The specimens were manufactured by bonding two plates of aluminium together for each specimen type. The aluminium plates had been pre-treated by chromic acid anodisation and application of BR-127 primer. A lay-up was created of the two plates, with the uncured epoxy film in between. This stack was then placed in a vacuum bag and cured in an autoclave according to the manufacturer's specifications (120°C for 1 hour at 6 bar with a 2°C/min heating and cooling rate). After curing, the plates were cut into strips, which were then milled down to a nominal width of 25 mm. Each of the aluminium arms had a nominal thickness of 6 mm, resulting in a nominal total thickness of 12 mm plus the adhesive thickness. The 1l specimens were 300 mm long and the 1.5l and 2l specimens were 270 mm long (in both cases based on the available adherend stock). As for all tests the crack never got closer than 100 mm to the end of the specimen, the difference in specimen lengths should not have any effect. The measured final dimensions of each specimen can be found in the online datasets [5, 28].
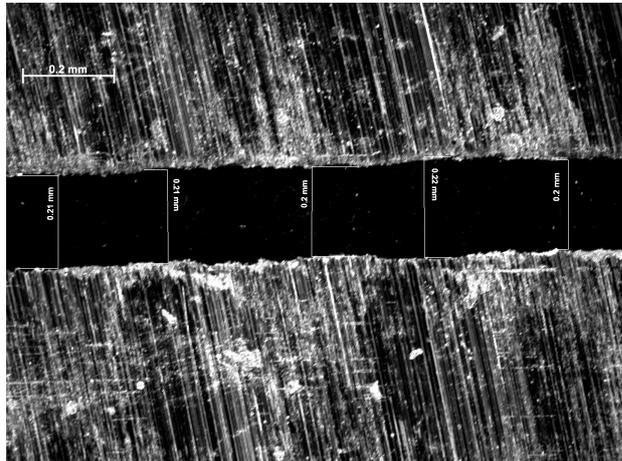
(a) 1.5l specimen

(b) 2l specimen

Figure 2.2: Microscopic pictures of the adhesive layer in two specimens with different nominal thickness. The pictures were taken from the side of the specimen after manufacturing.

Type	Specimen ID	Thickness [mm]
1 layer	Average	0.07
1.5 layers	H-002	0.195 ± 0.005
	H-003	0.135 ± 0.005
	H-004	0.245 ± 0.015
	H-006	0.220 ± 0.010
	H-008	0.210 ± 0.010
2 layers	G-002	0.275 ± 0.015
	G-006	0.275 ± 0.005
	G-008	0.275 ± 0.005
	G-009	0.265 ± 0.015
	G-010	0.285 ± 0.005

Table 2.1: Adhesive thickness at the mid-point of the specimen, as measured with the optical microscope. Only the average thickness is available for single layer specimens.

Polyester adhesive tape was placed over a portion of the aluminium plates before bonding, in order to provide a pre-crack length of 50 mm, as measured from the load application points.

For the single layer specimens, the average bond line thickness was 0.07 mm. As the 1l specimens had been tested in an earlier research project, individual measurements of the adhesive thickness of each specimen are not available. The adhesive thickness as measured at the mid-point of the specimen length for the 1.5l specimens and the 2l specimens is reported in Table 2.1.

Since in most cases multiple fatigue test were conducted on the same specimen, the tests were labelled with the scheme: [letter]-[number]-[Roman numeral], where the letter refers to the specimen series, the number to the specimen number in that series, and the Roman numeral refers to the number of the test on that specimen. For instance, E-003-II refers to the second test conducted on specimen 003 of series E. Due to issues with the test set-up (e.g. in one case the loading block became detached from the fatigue machine), not all tests produced valid crack growth data. Only the tests that produced valid data have been included in the following.
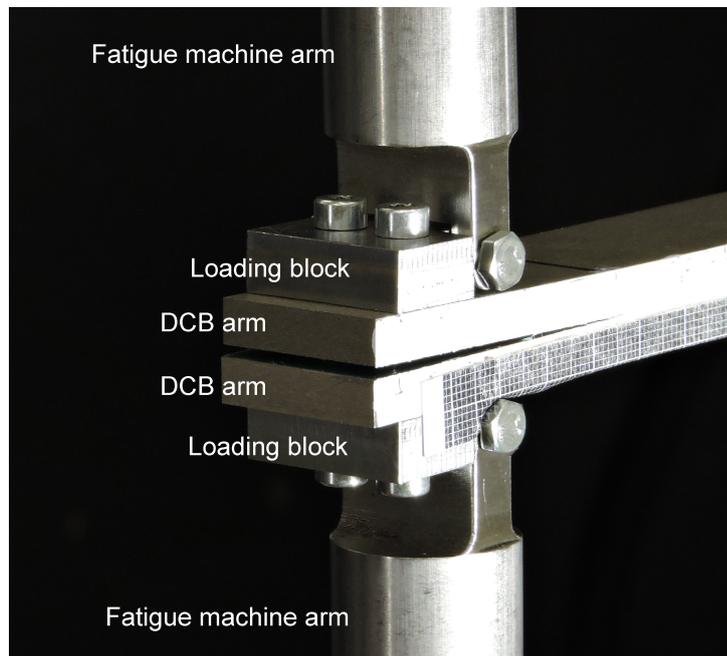
Figure 2.3: Loading blocks used to connect the specimens to the fatigue machine.

2.4   Test set-up

Fatigue tests were performed on an MTS 10 kN fatigue testing machine at a frequency of 5 Hz under displacement control. Force and displacement were measured by the fatigue bench and crack lengths were measured using a camera aimed at the side of the specimen. A strip of scale paper was fixed at the side of the specimen to allow measurement of the crack. The resolution of image used to determine the crack length was approximately 20 pixels/mm.

The specimens were connected to the fatigue machine using loading blocks that were attached to the specimen by bolts, as shown in Figure 2.3. Prior to each fatigue test, the specimens were quasi-statically loaded in displacement control, until crack propagation was observed visually. This ensured that the specimens contained an actual cohesive pre-crack in the adhesive layer. Even though the crack starters were placed at the adhesive/adherent interface, the quasi-static loading caused the crack to jump into the bulk of the adhesive layer. This was also verified by post-mortem inspection of the fracture surfaces of a number of specimens.

As mentioned above, the single layer results were collected by Pascoe et al. during a previous test programme [3, 4]. Initially tests were conducted

to obtain certain ratios of $\Delta G/G_{\max}$ (series B and C). This resulted in four different force ratios $R_{\mathrm{p}} = \frac{P_{\min}}{P_{\max}}$: 0.036, 0.29, 0.61 and 0.86. These ratios were used as displacement ratios $R_{\mathrm{d}} = \frac{d_{\min}}{d_{\max}}$ in the tests on the 1.5l and 2l specimens. To be able to compare that data with the data on single layer specimens, follow up tests on the 1l specimens were performed using these four values of the displacement ratio. As the force-displacement curve did not pass exactly through the origin, the force ratios were not exactly equal to the displacement ratios. The obtained force ratios are shown in Table 2.2, which gives an overview of all experiments discussed in this paper. For clarity of presentation the tests are grouped according to the four target R-ratios.

For $R_{\mathrm{p}} = 0.86$ the amount of crack growth produced for the 1.5l and 2l specimens was too small to be able to take accurate measurements, so the results for those experiments will not be presented here. For more information on the specimens and on the test set-up we refer the reader to the work of Pascoe [26] and to the master thesis of the present author [29].

2.5   Methods

The crack length was measured visually from the pictures taken by the side camera. The crack growth rate was then determined by fitting a power-law equation through the a vs N data and taking the derivative.

According to the ASTM standard [30], three methods are acceptable for measuring the mode I fracture toughness in composites. Since an equivalent standard does not exist for adhesively bonded specimens and given that the double cantilever beam geometry we used is similar to that described by ASTM, we refer to those standard test methods for computing the strain energy release rate. The three methods are:

- Modified Beam Theory Method (MBT);

- Compliance Calibration Method (CC);

- Modified Compliance Calibration Method (MCC).

The modified beam theory method is based on the hypothesis that the DCB specimen is equivalent to a double cantilever beam clamped at the crack tip, which allows no relative rotation of the upper and bottom adherents at the crack tip. The formula for the SERR under these conditions is:

$$G_{\mathrm{I}} = \frac{3Pd}{2wa} \qquad\qquad (2.1)$$

Type	Experiment	R_d	R_p	Group
1 layer	B-001-II	0.1	0.036	0.036
	B-002-I	0.88	0.86	0.86
	B-002-II	0.74	0.61	0.61
	C-001-I	0.33	0.29	0.29
	C-002-D	0.67	0.61	0.61
	D-002-I	0.29	0.29	0.29
	E-001-I	0.29	0.24	0.29
	E-001-II	0.29	0.27	0.29
	E-002-I	$2.3 \cdot 10^{-4}$	-0.022	0.036
	E-002-II	$-9.3 \cdot 10^{-5}$	0.014	0.036
	E-003-I	0.61	0.60	0.61
	E-003-II	0.61	0.62	0.61
1.5 layers	H-002-I	0.036	0.0054	0.036
	H-002-II	0.033	-0.0070	0.036
	H-003-I	0.29	0.24	0.29
	H-003-II	0.29	0.25	0.29
	H-004-I	0.61	0.56	0.61
	H-006-I	0.61	0.56	0.61
	H-008-I	0.86	0.83	0.86
2 layers	G-002-I	0.29	0.25	0.29
	G-002-II	0.29	0.23	0.29
	G-006-III	0.036	$-3.1 \cdot 10^{-4}$	0.036
	G-008-I	0.61	0.47	0.61
	G-009-I	0.61	0.56	0.61
	G-010-I	0.86	0.83	0.86
	G-010-II	0.033	-0.039	0.036

Table 2.2: Summary of the experiments and their corresponding R-ratios. The tests are grouped according to the R-ratio used, as shown in the last column.

where w is the width of the specimen, P and d are the applied load and displacement respectively, and a is the crack length. Because the two adherents can actually rotate at the crack tip, the value of G_I computed by Equation (2.1) tends to be slightly overestimated.

The compliance calibration method differs from the MBT method in that it directly includes the decrease of stiffness consequent from crack growth. The compliance $C = \frac{d}{P}$ is plotted against the measured crack length on a log-log diagram. A straight line (on the logarithmic scale) is then fit through the data by using a least-squares fitting algorithm, and the slope of the line, n is computed. The strain energy release rate is then calculated according to:

$$G_I = \frac{nPd}{2wa} \tag{2.2}$$

In the modified compliance calibration method, a constant A is computed as the slope of a straight line fitting, in a least squares sense, the plot of $\frac{a}{h}$ versus $C^{\frac{1}{3}}$ generated from the data, where h is the specimen thickness. The resulting formula for computing the SERR is:

$$G_I = \frac{3(PC^{\frac{1}{3}})^2}{2Awh} \tag{2.3}$$

None of the three methods above is clearly superior to the others; ASTM standard [30] indicates a difference of 3.1% in the value of the toughness computed by Equations (2.1), (2.2) and (2.3). In this research, the compliance calibration method was applied. The compliance was calculated as $C = \frac{d_{max} - d_{min}}{P_{max} - P_{min}}$, where P_{max}, d_{max} and P_{min}, d_{min} are respectively the maximum and minimum load and displacement applied in each cycle. The value n was determined for each experiment individually.

Following the method previously presented by Pascoe et al. [4], the energy dissipation per cycle $\frac{dU}{dN}$ was computed by taking the derivative of a power-law fit through the total strain energy U vs N data. The energy U was calculated as:

$$U = \frac{1}{2}P_{max}(d_{max} - d_0) \tag{2.4}$$

where d_0 is the displacement for which the recorded force was zero.

Similarly to Equation (2.4), we can define the cyclic energy U_{cyc} as:

$$U_{cyc} = \frac{1}{2}(P_{max}d_{max} - P_{min}d_{min}) \tag{2.5}$$

This expression, which holds under the assumption that the load-displacement curve is linear, can be used to quantify the energy stored in the specimen

during each fatigue cycle. In fact, as the cyclic energy calculated by Equation (2.5) is a measure of the work done by the test machine in a cycle, by the first law of thermodynamics it must be equal to the increase of internal energy of the specimen plus the energy spent to create new fracture surfaces. By noting this, we can also estimate the amount of cyclic energy which goes in the adhesive layer, $U_{\text{cyc, adh}}$, as:

$$U_{\text{cyc, adh}} = \int_{t_{\text{min}}}^{t_{\text{max}}} \int_{V_{\text{adh}}} \boldsymbol{\sigma} : \dot{\boldsymbol{\varepsilon}} \, dV \, dt \tag{2.6}$$

where V_{adh} is the volume of the adhesive layer, $\boldsymbol{\sigma}$ is the stress tensor, $\dot{\boldsymbol{\varepsilon}}$ is the strain rate and t_{min} and t_{max} are the time instants corresponding to d_{min} and d_{max}.

The energy dissipated by plasticity can be computed as:

$$U_{\text{pl}} = \int_{V_{\text{adh}}} \boldsymbol{\sigma} : \boldsymbol{\varepsilon}_{\text{pl}} \, dV \tag{2.7}$$

where $\boldsymbol{\varepsilon}_{\text{pl}}$ is the plastic strain. If the adherents start yielding, this formula must be modified by extending the integral to the whole volume of the specimen. However, since in this work no plasticity was observed in the adherents, we will refer to Equation (2.6) to compute the plastic dissipation.

A way of examining the resistance to fatigue crack growth is by looking at the amount of energy dissipated per unit of crack growth, G^*, which was calculated according to:

$$G^* = \frac{1}{w} \frac{\frac{\text{d}U}{\text{d}N}}{\frac{\text{d}a}{\text{d}N}} \tag{2.8}$$

Equation (2.8) reduces to:

$$G^* = \frac{1}{w} \frac{\text{d}U}{\text{d}a} \tag{2.9}$$

which is equal to the expression for the strain energy release rate. However, it should be noted that the SERR as defined by Irwin [31, 32] is a proper derivative in the mathematical sense, whereas G^* is an average over one fatigue cycle.

As G^* represents the amount of energy dissipated per unit of crack growth, it can be seen as a measure of the crack growth resistance. More energy dissipation per unit of crack growth means it is harder for the crack to grow. Thus G^* can be used to investigate whether the crack resistance is constant, and if not, what factors influence it. It should be noted however, that G^* measures all forms of energy dissipation. Therefore it can only be used to say something about the crack resistance if there are no other dissipative mechanisms active that are unrelated to crack growth.
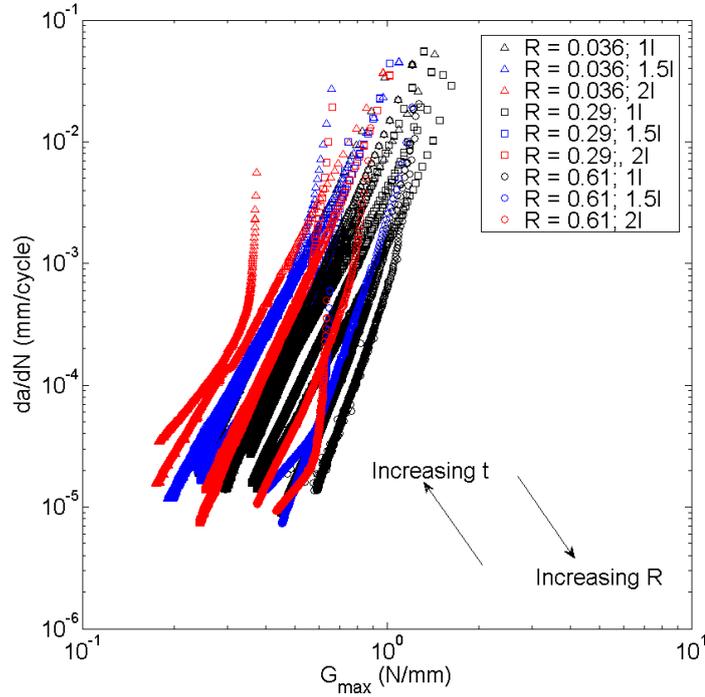
Figure 2.4: Crack growth rate vs maximum strain energy release rate. All test data are plotted together to explicitly show the dependence of the curves on the R-ratio.

2.6   Experimental results

Figure 2.4 shows the crack growth rate plotted against the maximum strain energy release rate, following the conventional method. The results for all adhesive thicknesses are shown in the picture. An R-ratio effect is clearly visible: higher R-ratios mean a lower crack growth rate. This is to be expected, as a higher R-ratio means a lower ΔG for the same $G_{\max}$.

The data already illustrated are plotted again in Figure 2.5, this time divided according to their R-ratio, so to explicitly highlight the effect of the adhesive thickness. Another way to look at this is shown in Figure 2.6, which indicates for each experiment the $G_{\max}$ that results in a crack growth rate of 10^{-4} mm/cycle, as a function of bondline thickness. In Figure 2.6, linear fits through the data are shown, one for each R-ratio, as a guide to the eye. However, given what is known about the effect of thickness, it is likely that the actual dependence of $G_{\max}$ on t for a given $\frac{\mathrm{d}a}{\mathrm{d}N}$ is non-linear. There is a clear effect of adhesive thickness: increasing the thickness from one layer causes an increase in crack growth rate for the same load cycle. The effect
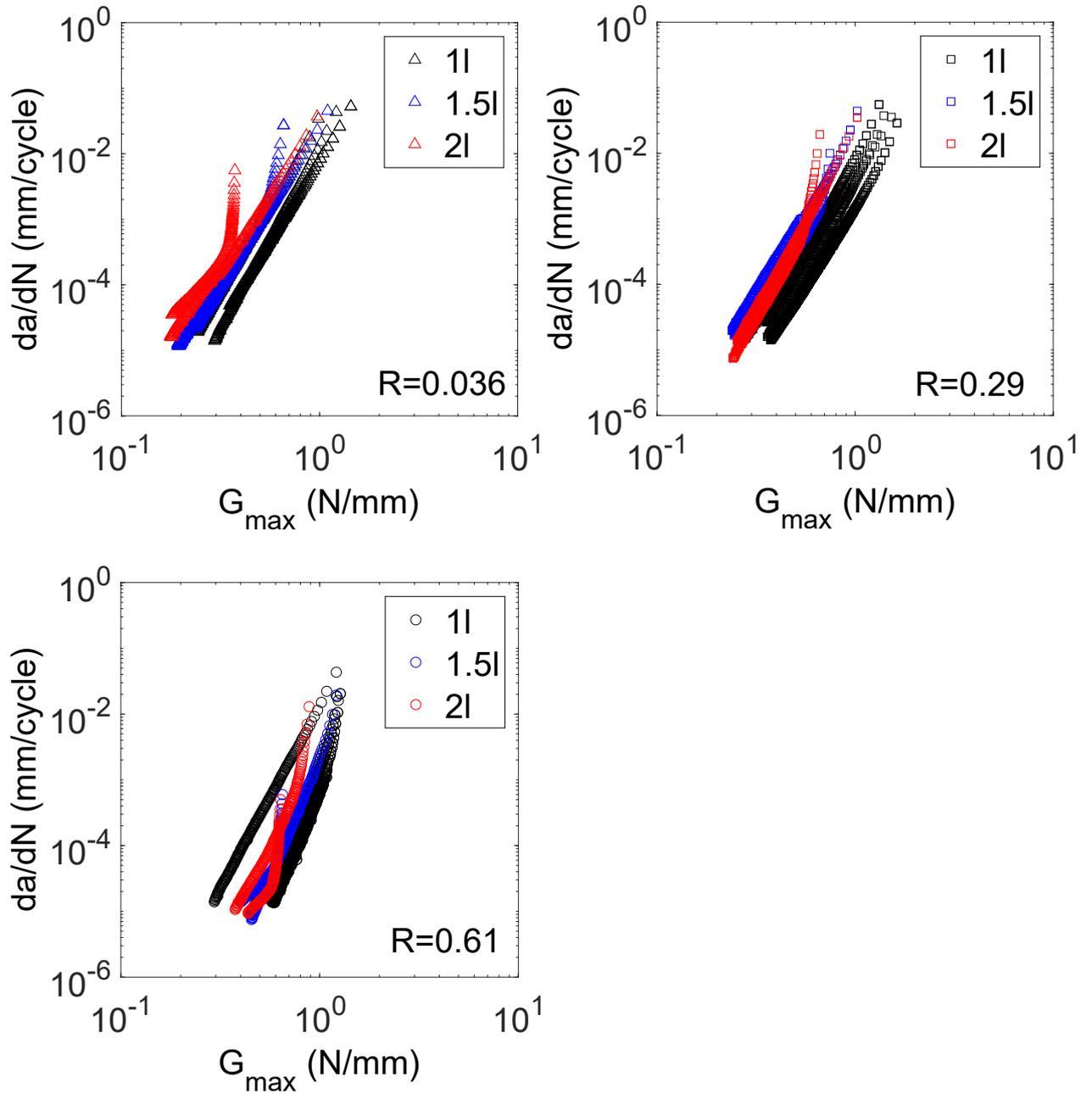
Figure 2.5: Crack growth rate as a function of the maximum strain energy release rate. The data are grouped according to the R-ratio to show the effect of the thickness.
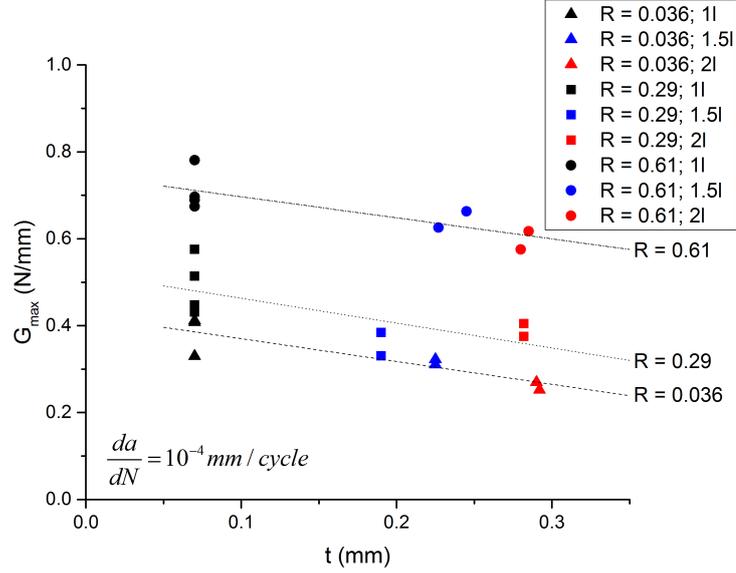
Figure 2.6: G_{max} corresponding to a given value of the crack growth rate, plotted as a function of the adhesive thickness. Linear fits through the data are shown, as a guide to the eye.

of increasing from 1 layer to 1.5 layers appears to be larger than that of increasing from 1.5 layers to 2 layers. However, it should be noted (as it can be seen in Table 2.1 and Figure 2.6) that going from 1 to 1.5 layers also causes a larger increase of the final bondline thickness than going from 1.5 to 2 layers.

In contrast to the traditional method, Figure 2.7 shows the crack growth rate plotted against the strain energy dissipation per cycle $\frac{\mathrm{d}U}{\mathrm{d}N}$. Here the data fall into a narrow band, except for three experiments: G-006-III (2 layers, $R = 0.036$), H-006-I (1.5 layers, $R = 0.61$) and G-008-I (2 layers, $R = 0.61$). The figure shows that the effect of adhesive thickness on the relationship between energy dissipation per cycle and crack growth rate is limited, especially in comparison to the effect of thickness on the relationship between crack growth rate and G_{max}.

The anomalous behaviour of specimens H-006-I and G-008-I can potentially be explained by the observed crack growth behaviour. In these experiments secondary cracks growing along the adhesive/adherent interface were observed. A definition of secondary crack is schematically shown in Figure 2.8. The secondary crack develops as a branch of the main crack, extending through the adhesive thickness and growing close to the adhesive/adherent interface. Figure 2.9 shows a photograph of the secondary cracks in a 1.5l specimen. These secondary cracks were not present during
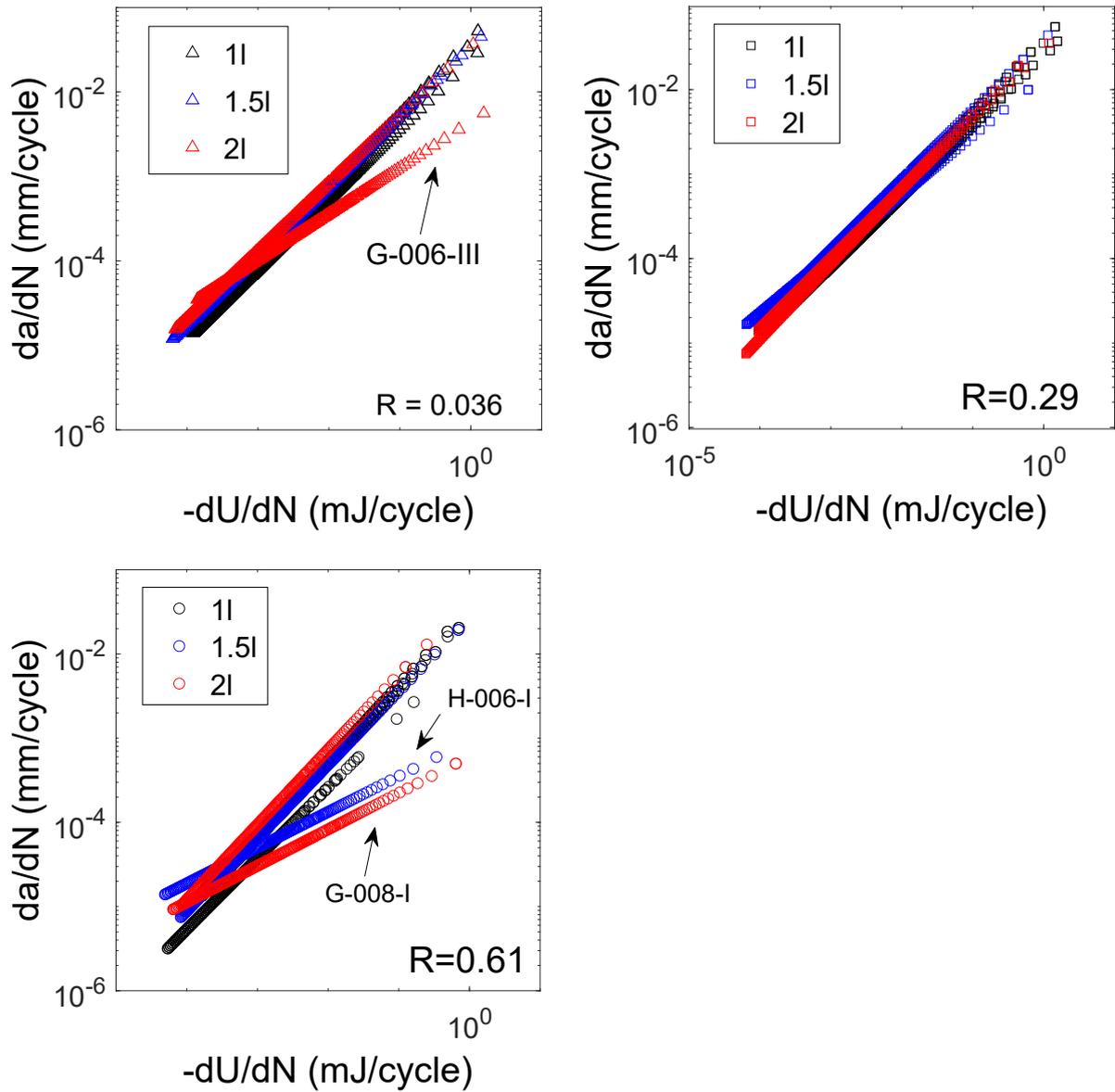
Figure 2.7: Crack growth rate vs energy dissipation per cycle. Data are grouped according to the R-ratio.
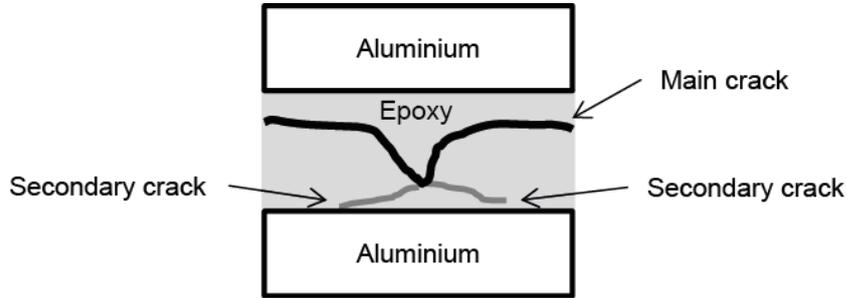
Figure 2.8: Schematic representation of a secondary crack developing inside the adhesive thickness.

the other experiments. The growth of these secondary cracks will also dissipate energy, while not producing an advance of the main crack tip. As a consequence, the total amount of energy dissipated per unit of growth of the main crack will be increased, which is what is seen in Figure 2.7. We note that the growth of secondary cracks is only observed in the first part of the test, after which they stop and the crack grows as a cohesive crack inside the adhesive layer. An hypothesis on why this secondary crack growth occurs is formulated later in section 2.9.

Note that for all the anomalous experiments a second experiment was conducted under the same load conditions. During these repeat experiments no secondary crack growth was observed, and the data for these repeat experiments fall into the same band as for the bulk of the experiments.

In Figure 2.10 G^* is compared to the maximum SERR value $G_{\max}$. For most of the data there is a linear relationship between G^* and $G_{\max}$. The exceptions are the three experiments that were identified as outliers in Figure 2.7, as well as experiments B-001-II (1 layer, $R = 0.61$) and H-003-I (1.5 layers, $R = 0.29$). For these experiments the G^* value rises asymptotically as $G_{\max}$ approaches a certain value. Apart from the outliers, the curves for the higher adhesive thickness specimens seem to follow the same linear trend as those for the single layer specimens. Even though there is some scatter in the data, this suggests that the adhesive thickness does not affect the crack growth resistance in a substantial way. For G-008-I (2 layers, $R = 0.61$) and H-006-I (2 layers, $R = 0.61$) the difference in behaviour compared to the other specimens seems to be linked to the secondary crack growth discussed above. As the secondary crack growth was only seen during the early part of the test, when the $G_{\max}$ value is high, this could explain why for low $G_{\max}$ values the G^* value matches that seen during the tests without secondary crack growth.

Another view on the amount of energy required for crack growth is given
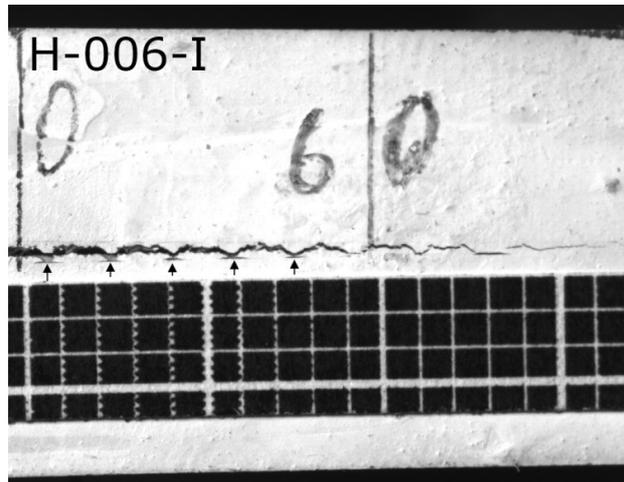
(a) w/ secondary cracks
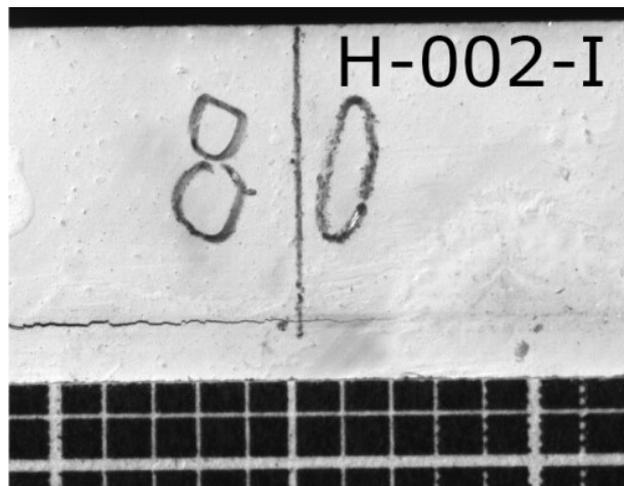
(b) w/o secondary cracks

Figure 2.9: Fatigue crack growth in 1.5l specimens. The two photographs show the difference between cracks with and without secondary branching.
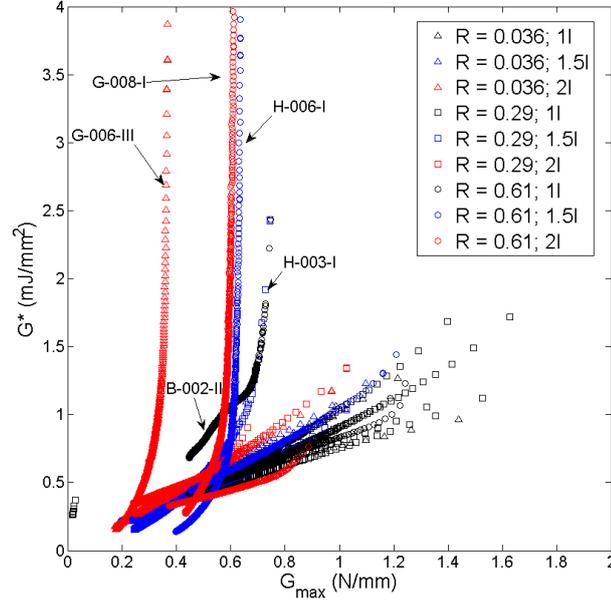
Figure 2.10: Fatigue crack growth resistance G^* vs maximum strain energy release rate.

by Figure 2.11, which shows how much energy was dissipated for a crack growth of 10^{-4} mm/cycle, as a function of G_{max}. The figure shows that for a given R-ratio, for higher adhesive thickness, the amount of energy dissipated to produce 10^{-4} mm/cycle crack growth rate was lower.

It was noted elsewhere [26, 33] that if G^* is fixed, i.e. the resistance to crack growth is the same, then the energy dissipation is strongly correlated to the applied cyclic work U_{cyc}. Figure 2.12 shows the energy dissipation as a function of U_{cyc} for a fixed G^*. It can be noted that for a given value of U_{cyc} the amount of energy dissipated in the increased thickness specimens is higher than that dissipated in the single adhesive layer specimens.

The raw and processed data presented in this work are available online [5, 28, 34].
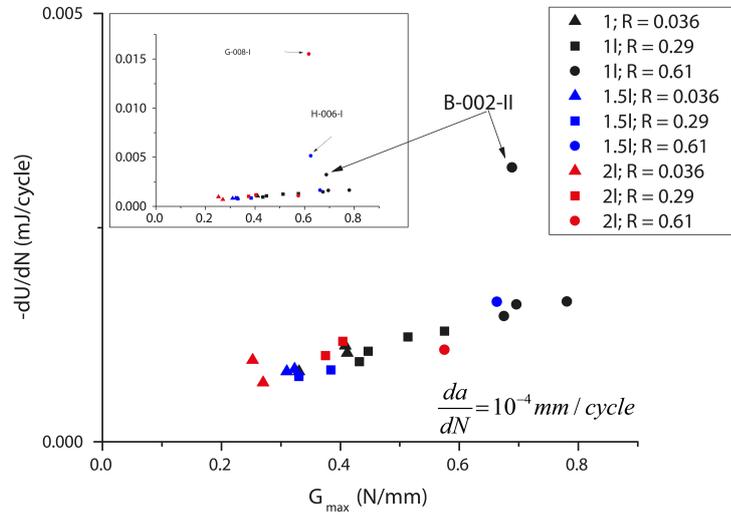
Figure 2.11: Energy dissipated per cycle for a fixed crack growth rate, plotted as a function of $G_{\max}$.
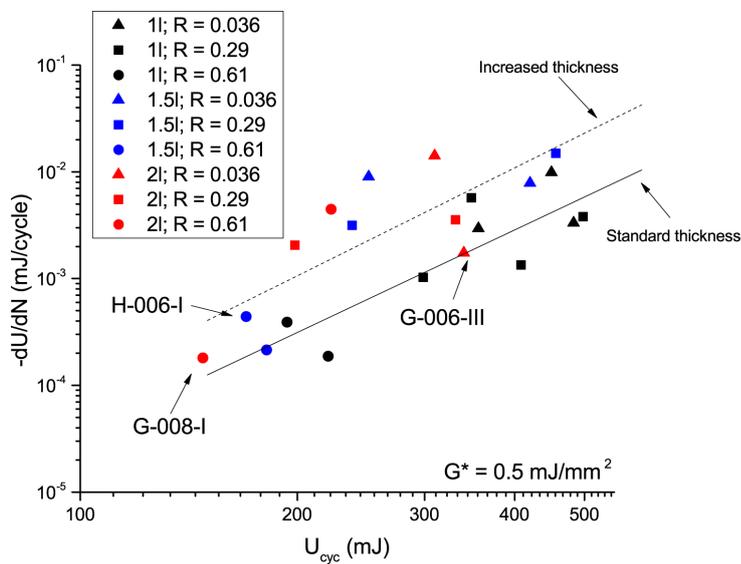
Figure 2.12: Energy dissipation per cycle as a function of the cyclic energy, for a fixed crack resistance G^*.
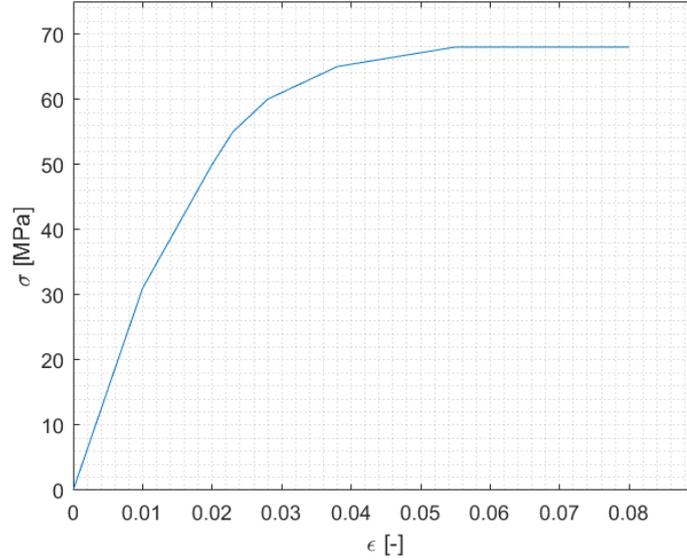
Figure 2.13: Elasto-plastic behaviour of FM94 epoxy as implemented to model the adhesive layer. Data taken from Papanicolaou et al. [36]

2.7   Numerical model

In order to compute the plasticity produced in the adhesive and its effect on the energy release and dissipation, a 2D finite element model was developed in the software package *Abaqus*. The geometry of the model was equal to that of the tested specimens, i.e. a double cantilever beam with same dimensions. The adherends were modelled as aluminium plates, while the adhesive was modelled as an epoxy layer cut by the disbond surface along its midline. Three different configurations of the epoxy layer were considered, corresponding to 1 layer, 1.5 layers and 2 layers of adhesive, which resulted in an adhesive thickness equal to 0.08, 0.20 and 0.28 mm respectively.

Both the aluminium and the epoxy were modelled as isotropic materials with elastic-plastic behaviour; the elasto-plastic properties of the FM94 epoxy are reported in the literature [35, 36]. Figure 2.13 shows the stress-strain curve which was used to define the elasto-plastic behaviour of the adhesive in the numerical model.

The Virtual Crack Closure Technique (VCCT) [37, 38] was used to compute the strain energy release rate in the adhesive. Although the use of the VCCT is usually restricted to the framework of linear elastic fracture mechanics, a similar application of this technique to yielding of FM300 adhesive is discussed in Jokinen et al [39].

The entire specimen was meshed with second-order plain strain elements

with quadrangular shape, i.e. types CPE8 and CPE8R in Abaqus. The mesh was refined in order to accommodate a sufficient number of elements around the crack tip; this resulted in a minimum of 4 elements through the adhesive thickness in the single layer specimen.

The model was loaded under displacement control similarly to the experimental tests. First the specimen was applied a linear displacement equal to $d_{\max}$, then it was unloaded down to a displacement of $d_{\min}$ and then loaded up again to $d_{\max}$. Globally, this reproduces the loading conditions occurring during a single cycle in the fatigue tests. The values $d_{\max} = 2.85$ mm and $d_{\min} = 1.89$ mm were used in the simulations, which are numerically equal to those applied to specimen C-002-D in the tests. One single cycle was applied in each simulation. We run a total of ten simulations for each adhesive configuration, varying the length of the cracked area from 55 mm to 100 mm, with steps of 5 mm.

2.8   Numerical results

Figure 2.14 shows a comparison between the strain energy release rates G_{I} computed with the VCCT in the three different configurations of adhesive thickness. The G_{I} calculated from experimental data on single layer specimens is also plotted for comparison. Only specimens with an applied displacement comparable to that used in the simulations are reported. The variation of strain energy release rate in the three configurations is as little as 7%. This suggests that, at least for the range of thicknesses considered here, varying the adhesive thickness has little effect on G_{I}. The strain energy release rate computed by the VCCT differs by no more than 15% from the experimental results for all the considered disbond lengths. The numerical and experimental curves tend to diverge for short disbonds, which can be related to the presence of the insert used for pre-cracking. It might be that, as the crack starts at the insert, only after some length the SERR reaches the value observed for crack growth in the bulk adhesive. Comparing the numerical results to the data from specimen C-002-D, which were obtained under basically the same cyclic displacement, shows an almost complete overlapping of the curves for both the maximum and minimum strain energy release rates, which suggests that both the upper and lower part of the loading cycle are well reproduced by the model.

The cyclic energy U_{cyc} computed by the numerical model for different adhesive thicknesses is plotted in Figure 2.15 versus the crack length. The cyclic energy of specimen C-002-D is also plotted for comparison, given that the same loading cycle is applied. For both cases, Equation (2.5) is used
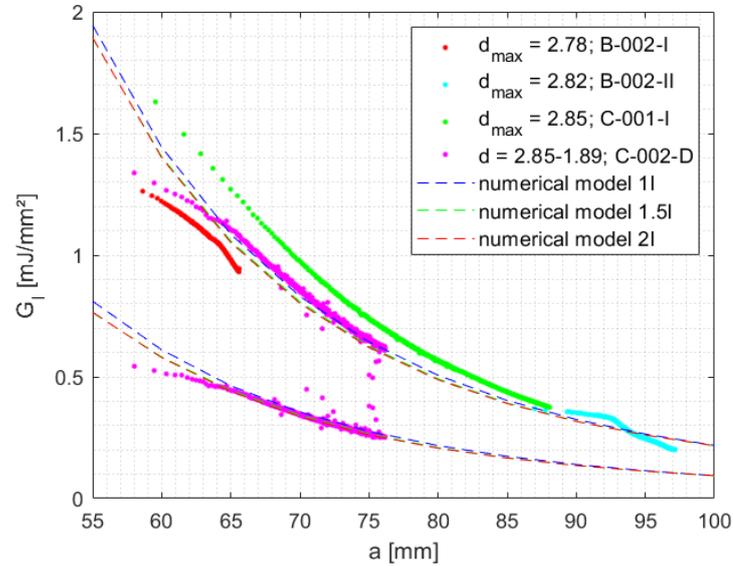
Figure 2.14: SERR computed with the VCCT for different adhesive thickness (dashed lines) and from experimental data (dots). The same load cycle is applied in specimen C-002-D and in the simulations.
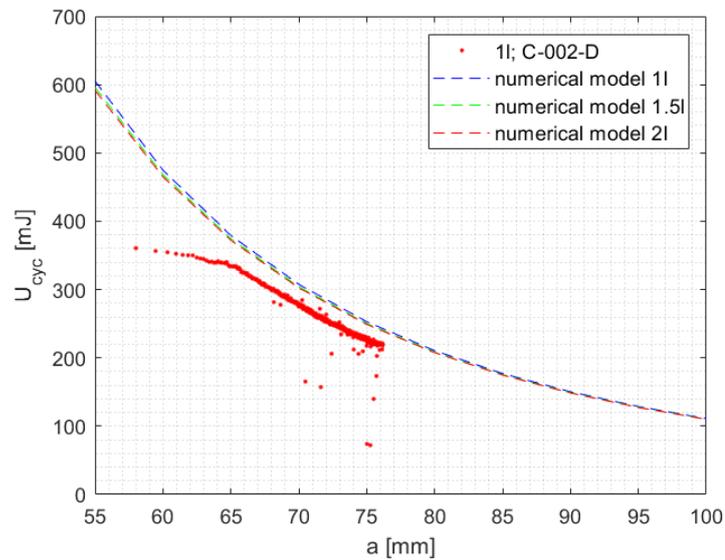
Figure 2.15: Cyclic energy computed by the model for different adhesive thicknesses. Data of specimen C-002-D are also shown for comparison.
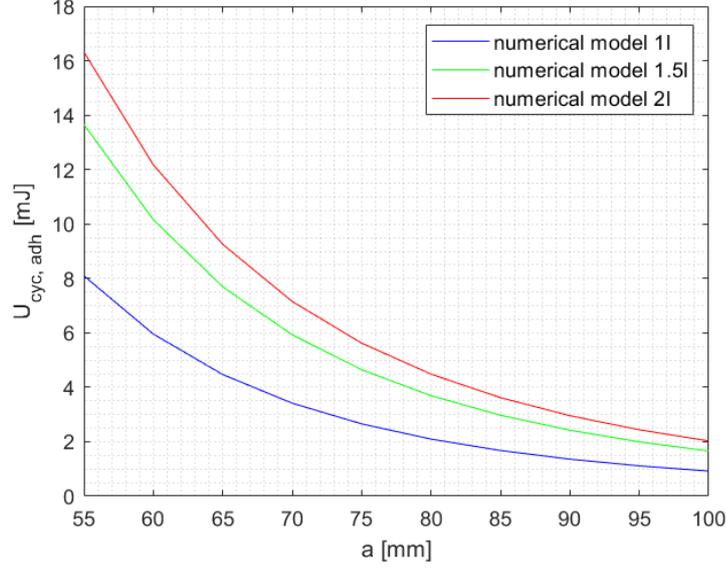
Figure 2.16: Cyclic energy of the adhesive computed for different thicknesses, plotted as a function of crack length.

to calculate U_{cyc}. Like in Figure 2.14, the effect of the thickness is small, in that the U_{cyc} computed in the three configurations differs by as little as 2.5%. The value of the cyclic energy computed by the model is slightly overestimated compared to that of the tested specimen (about 10% more). We note that, at the beginning of the test, the experimentally measured U_{cyc} is remarkably lower than the computed one, which has probably to do with the high compliance of the specimen.

By using Equation (2.6), we can compute the cyclic strain energy of the adhesive layer, $U_{\text{cyc, adh}}$, for different thicknesses. The results are shown in Figure 2.16. The figure clearly shows that more energy goes in the thicker adhesive. However, by comparison with Figure 2.15, it can be noted that the amount of strain energy in the adhesive is only a small fraction of the energy in the whole specimen, which explains why no appreciable variation of U_{cyc} could be seen for different thicknesses.

The crack growth resistance G^* can be estimated numerically by using Equation 2.9. This requires first the computation of the total energy U for each cycle, which can be done straightforwardly by Equation (2.4). In order to compute $\frac{\mathrm{d}U}{\mathrm{d}a}$, a power-law fitting of U vs a is generated using a least squares algorithm. This yield an expression in the form:

$$U = \alpha a^{\beta} + \gamma \tag{2.10}$$

The derivative $\frac{\mathrm{d}U}{\mathrm{d}a}$ is then computed by differentiating Equation (2.10), which

Type	α	β	γ
1 layer	$7.038 \cdot 10^7$	-2.764	-10.65
1.5 layers	$6.345 \cdot 10^7$	-2.742	-11.88
2 layers	$6.050 \cdot 10^7$	-2.732	-12.37

Table 2.3: Coefficients of the power-law fitting of U vs a, as expressed in Equations (2.10) and (2.11). The energy U is measured in [mJ], the crack length in [mm].

gives:

$$\frac{\mathrm{d}U}{\mathrm{d}a} = \alpha\beta a^{\beta-1} \tag{2.11}$$

The coefficients of the power-law for the three adhesive thicknesses are provided in Table 2.3.

Figure 2.17 shows the fatigue crack growth resistance G^* computed by the model for the single layer adhesive, plotted as a function of the maximum SERR. Also shown are the experimental data of four 1l specimens. It is worth noting that the numerical results are computed according to Equation (2.9), thus not considering the crack growth rate, while the experimental G^*, calculated by Equation 2.8, explicitly considers it. Despite this conceptual difference, and the scatter already noted in Figure 2.10, the results of the model fall within the same range of the experimental data.

No plasticity occurs in the aluminium adherends, in accordance to what was observed in the tested specimens. On the contrary, the yield strength of the epoxy is exceeded in a region around the crack tip, which extends through the adhesive thickness. This means that a plastic deformation is produced in the adhesive layer during the loading cycle, which is not recovered after unloading. As a result, a net amount of energy associated to the plastic strain is dissipated in the process. The plastic dissipation per unit crack growth is given by $\frac{\mathrm{d}U_{\mathrm{pl}}}{\mathrm{d}A} = \frac{1}{w}\frac{\mathrm{d}U_{\mathrm{pl}}}{\mathrm{d}a}$. This was computed using a power-law fitting of the form of Equations (2.10) and (2.11). The coefficients of the fitting are shown in Table 2.4. The amount of plastic dissipation depends on the applied energy, which for a single cycle is equal to U_{cyc}.

The plastic energy dissipation is affected by the adhesive thickness, as shown in Figure 2.18. The thicker the adhesive layer, the more energy is dissipated by plasticity for a given applied energy. The relationship between the amount of dissipated energy and the adhesive thickness is non-linear, as it is clearly visible in the figure: increasing the thickness from 0.08 mm
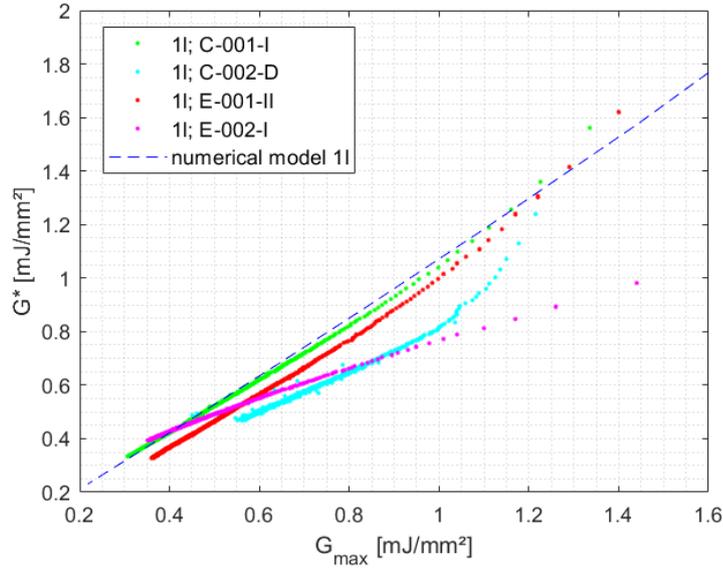
Figure 2.17: Fatigue crack growth resistance compute by the model and from experimental data, plotted as a function of the maximum SERR.

Type	α	β	γ
1 layer	$1.962 \cdot 10^{10}$	-5.644	0.0169
1.5 layers	$2.069 \cdot 10^{10}$	-5.534	-0.0758
2 layers	$1.571 \cdot 10^{10}$	-5.440	-0.1431

Table 2.4: Coefficients of the power-law fitting of U_{pl} vs a, as expressed in Equations (2.10) and (2.11). The plastic energy U_{pl} is in [mJ], the crack length in [mm].
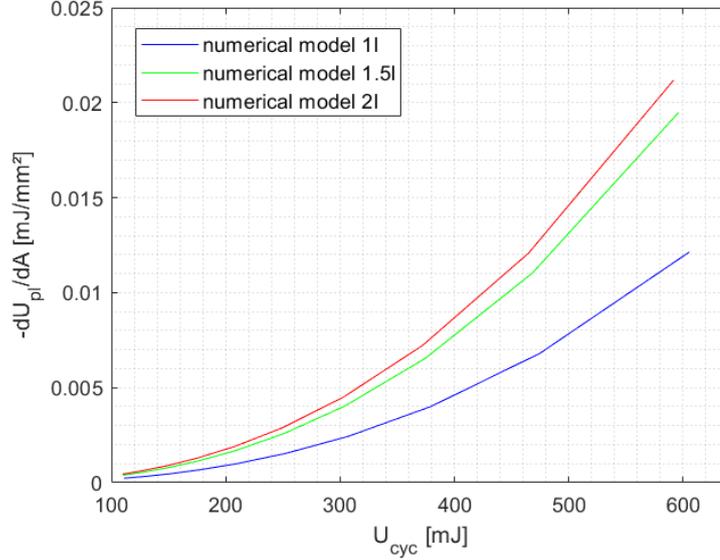
Figure 2.18: Plastic energy dissipation computed by the model for different adhesive thicknesses.

(1 layer) to 0.20 mm (1.5 layers) results in a plastic dissipation which is 1.6 times the original value; an additional increase to 0.28 mm only increases the dissipation of about 10%.

2.9   Discussion of experimental and numerical results

A comparison between Figures 2.4 and 2.10 shows that despite the higher G^* for higher $G_{\max}$, the crack growth rate is also higher. That is to say: although more energy is being dissipated per unit of crack growth, the crack growth rate is also higher. That faster crack growth requires more energy dissipation per unit of growth has been observed previously [40], though not to the extent seen here. This implies that increasing $G_{\max}$ not only increases the resistance (in terms of required energy per unit crack growth), but also the amount of energy available for crack growth.

In particular, it appears that the secondary crack growth seen during experiments G-008-I and H-006-I is driven by an extra amount of energy that is not available for normal crack growth. Otherwise it cannot be explained that the same crack growth rate is achieved for much higher G^* values.

Although no secondary crack growth was seen for experiments G-006-III (2 layers, $R = 0.036$), B-001-II (1 layer, $R = 0.61$), and H-003-I (1.5 layers,

$R = 0.29$), the similarity in the shape of the G^* vs G_{max} curves to those
for G-008-I and H-006-I suggests that also for these specimens there is some
form of dissipative mechanism that is activated at high G_{max} values. What
mechanism this is could not be determined during the present research. Pos-
sibilities include void formation that is not in line with the main crack (and
therefore does not contribute to crack advance), or secondary crack forma-
tion that was not visible from the side of the specimen. Further research is
required to investigate these possibilities.

The experimental results show that the adhesive thickness has little effect
on the energy dissipated per unit of crack surface created, as illustrated in
Figure 2.10. At the same time, Figure 2.12 shows that the adhesive thickness
does affect the total amount of energy dissipated for a given load cycle.

Together Figures 2.10 and 2.12 give an insight on the mechanism of crack
growth. The energy dissipation required per unit crack growth for a given
load cycle, i.e. combination of G_{max} and U_{cyc}, is not affected by the thickness.
On the other hand, an increase in adhesive thickness results in a larger total
amount of energy dissipation $\frac{\mathrm{d}U}{\mathrm{d}N}$, implying more energy is available for crack
growth. As a result, for G^* to be constant, the crack growth rate must be
higher for higher adhesive thickness. This explains why a thicker adhesive
results in a higher $\frac{\mathrm{d}a}{\mathrm{d}N}$ for a given G_{max}, as shown in Figure 2.4.

The numerical results confirm that increasing the adhesive thickness yields
no substantial difference in the strain energy release rate. Considering the
thickness-independent correlation between G_{max} and G^* shown in Figure 2.10,
this means that the resistance to crack growth is also independent on the
thickness.

Conversely, more plastic dissipation was found in specimens with thicker
adhesive. Comparing this with experimental results shows that the increased
plasticity has a favourable effect on crack growth.

It seems likely that plastic deformation is related to some form of damage
(e.g. voids and crazes) that contributes to crack growth. A recent investiga-
tion [41] using in-situ SEM observations of crack growth tests on carbon fibre
reinforced polymers suggests that even under mode I loading crack growth
occurs by link-up of micro-cracks nucleating ahead of the crack tip. If plastic
deformation prompted the formation of micro-cracks around the crack tip,
that would explain why more crack growth was observed with thicker adhe-
sive, as well as why secondary cracks developed in the thick specimens only
in the first part of the test. In fact, from Figure 2.18 we can see that most
plasticity is produced when the applied U_{cyc} is high, i.e. at the beginning of
the test, possibly resulting in micro-cracks formed at the sides of the crack
tip, which link up creating secondary cracks. The formation of secondary
cracks would then stop when the plastic deformation decreases under a cer-

tain level. Further investigations of the micro-mechanics of fatigue crack growth are required to test this hypothesis.

The effect of increasing the thickness is opposite to most of the fatigue results from literature discussed above, including e.g. the results of Azari et al. [11], Mall and Ramamurthy [16] and Chai [13]. In fact, the damaging mechanism associated to plasticity would be obviously material dependent, and furthermore the thicknesses investigated here were lower than those used in previous studies, which could explain why opposite results are reported in the literature, i.e. decreased crack growth rate with increasing adhesive thickness.

This suggests that also in fatigue there is an optimum thickness, such as found by Kinloch and Shaw [6] and Yan et al. [10] for the (quasi-static) fracture toughness. In the quasi-static case increasing the thickness above this optimum results in a lower fracture toughness; similarly, in fatigue it might result in a higher crack growth rate for a given load cycle. Kinloch and Shaw [6], and Bascom and Cottington [7] suggest that the highest G_{Ic} value is obtained when the plastic zone size at the critical load is equal to the adhesive thickness. Since the plastic zone size depends on the yield strength, this would make the optimum thickness material dependant.

This leads to the hypothesis that, for the FM94 epoxy tested here, the bond line thicknesses were greater than the optimum thickness, whereas for the other adhesives reported in literature the thicknesses were still below the optimum thickness.

2.10 Conclusions

A combination of experiments and numerical calculations was used to investigate the effect of adhesive thickness on fatigue crack growth in an FM94 epoxy adhesive bond.

For the range of thicknesses investigated in this research, increasing the adhesive thickness results in an increase of the crack growth rate. The resistance to crack growth (energy dissipation per unit crack growth) is not affected by changes in the adhesive thickness. However, the amount of energy available per unit crack growth, for a given load, increases when the adhesive thickness is increased. The net result is an increased crack growth rate.

The numerical results confirm that the resistance to crack growth is not affected by the adhesive thickness, although more plastic dissipation is found in thicker specimens. It is hypothesised that this plastic deformation promotes the formation of micro-cracks around the crack tip, which result in

increased crack growth and creation of secondary cracks in thicker adhesives.

A more detailed investigation of the micro-mechanics of crack growth and the crack opening is needed in order to determine how exactly the plastic deformation influences the crack growth rate. Such an investigation might also be able to show if and when increased plastic dissipation leads to a shielding effect, reducing the crack growth rate, as has been reported in literature for larger adhesive thicknesses.

Furthermore, the present results show that the effect of adhesive thickness most likely depends on whether the thickness is smaller or greater than a material-dependant optimum thickness. Care must therefore be taken when assuming that trends observed in one adhesive will also apply to a different adhesive.

References

1. Pascoe, J. A., Alderliesten, R. C. & Benedictus, R. Methods for the prediction of fatigue delamination growth in composites and adhesive bonds - A critical review. *Engineering Fracture Mechanics* **112-113,** 72–96. `http://dx.doi.org/10.1016/j.engfracmech.2013.10.003` (2013).

2. Alderliesten, R. C., Brunner, A. J. & Pascoe, J. A. Cyclic fatigue fracture of composites: What has testing revealed about the physics of the processes so far? *Engineering Fracture Mechanics* **203,** 186–196 (2018).

3. Pascoe, J., Alderliesten, R. & Benedictus, R. Towards Understanding Fatigue Disbond Growth via Cyclic Strain Energy. *Procedia Materials Science* **3,** 610–615. `http://dx.doi.org/10.1016/j.mspro.2014.06.101` (2014).

4. Pascoe, J. A., Alderliesten, R. C. & Benedictus, R. On the relationship between disbond growth and the release of strain energy. *Engineering Fracture Mechanics* **133,** 1–13. `http://dx.doi.org/10.1016/j.engfracmech.2014.10.027` (2015).

5. Pascoe, J. *Damage Tolerance of Adhesive Bonds - Datasets.* Dataset. 2014. `https://doi.org/10.4121/uuid:c43549b8-606e-4540-b75e-235b1e29f81d`.

6. Kinloch, A. J. & Shaw, S. J. The Fracture Resistance of a Toughened Epoxy Adhesive. *The Journal of Adhesion* **12,** 59–77 (1981).

7. Bascom, W. D., Cottington, R. L., Jones, R. L. & Peyser, P. The fracture of epoxy- and elastomer-modified epoxy polymers in bulk and as adhesives. *Journal of Applied Polymer Science* **19,** 2545–2562 (1975).

8. Wang, S. S., Mandell, J. F. & McGarry, F. J. An analysis of the crack tip stress field in DCB adhesive fracture specimens. *International Journal of Fracture* **14,** 39–58 (1978).

9. Daghyani, H. R., Ye, L. & Mai, Y. W. Mode-I Fracture Behaviour of Adhesive Joints. Part II. Stress Analysis and Constraint Parameters. *The Journal of Adhesion* **53,** 163–172 (1995).

10. Yan, C., Mai, Y. W. & Ye, L. Effect of bond thickness on fracture behaviour in adhesive joints. *Journal of Adhesion* **75,** 27–44 (2001).

11. Azari, S., Papini, M. & Spelt, J. K. Effect of adhesive thickness on fatigue and fracture of toughened epoxy joints - Part I: Experiments. *Engineering Fracture Mechanics* **78,** 153–162 (2011).

12. Azari, S., Papini, M. & Spelt, J. K. Effect of adhesive thickness on fatigue and fracture of toughened epoxy joints - Part II: Analysis and finite element modeling. *Engineering Fracture Mechanics* **78,** 138–152 (2011).

13. Chai, H. On the correlation between the mode I failure of adhesive joints and laminated composites. *Engineering Fracture Mechanics* **24,** 413–431 (1986).

14. Krenk, S., Jönsson, J. & Hansen, L. P. Fatigue analysis and testing of adhesive joints. *Engineering Fracture Mechanics* **53,** 859–872 (1996).

15. Abou-Hamda, M., Megahed, M. & Hammouda, M. Fatigue crack growth in double cantilever beam specimen with an adhesive layer. *Engineering Fracture Mechanics* **60,** 605–614. `https://linkinghub.elsevier.com/retrieve/pii/S0013794498000186` (1998).

16. Mall, S. & Ramamurthy, G. Effect of bond thickness on fracture and fatigue strength of adhesively bonded composite joints. *International Journal of Adhesion and Adhesives* **9,** 33–37 (1989).

17. Xu, X. X., Crocombe, A. D. & Smith, P. A. Fatigue crack growth rates in adhesive joints tested at different frequencies. *Journal of Adhesion* **58,** 191–204 (1996).

18. Schmueser, D. W. A fracture mechanics approach to characterizing cyclic debonding of varied thickness adhesive joints to electroprimed steel surfaces. *The Journal of Adhesion* **36,** 1–23 (1991).

19. Joseph, R., Bell, J. P., Mcevily, A. J. & Liang, J. L. Fatigue crack growth in epoxy/aluminum and epoxy/steel joints. *The Journal of Adhesion* **41,** 169–187 (1993).

20. Azari, S., Ameli, A., Papini, M. & Spelt, J. K. Analysis and design of adhesively bonded joints for fatigue and fracture loading: A fracture-mechanics approach. *Journal of Adhesion Science and Technology* **27,** 1681–1711 (2013).

21. Pardoen, T., Ferracin, T., Landis, C. M. & Delannay, F. Constraint effects in adhesive joint fracture. *Journal of the Mechanics and Physics of Solids* **53,** 1951–1983 (2005).

22. Chiu, W. K. & Jones, R. A numerical study of adhesively bonded lap joints. *International Journal of Adhesion and Adhesives* **12,** 219–225 (1992).

23. Gleich, D. M., Van Tooren, M. J. & Beukers, A. Analysis and evaluation of bondline thickness effects on failure load in adhesively bonded structures. *Journal of Adhesion Science and Technology* **15,** 1091–1101 (2001).

24. Gleich, D. M., Van Tooren, M. J. & Beukers, A. A stress singularity approach to failure initiation in a bonded joint with varying bondline thickness. *Journal of Adhesion Science and Technology* **15,** 1247–1259 (2001).

25. Lenwari, A., Thepchatri, T. & Santisukpotha, P. A fracture-based criterion for debonding strength of adhesive-bonded double-strap steel joints. *Engineering Journal* **16,** 17–25 (2012).

26. Pascoe, J. A. *Characterisation of Fatigue Crack Growth in Adhesive Bonds.* PhD thesis (Delft University of Technology, 2016), 147. `http://doi.org/10.4233/uuid:ebbf552a-ce98-4ab6-b9cc-0b939e12ba8b`.

27. Bürger, D. *Mixed-mode fatigue disbond on metallic bonded joints.* PhD thesis (Delft University of Technology, 2015). `http://dx.doi.org/10.4233/uuid:ec4dbcd6-052d-4009-bf9e-cdcbf4614174`.

28. Pascoe, J. A., Al Amery, A. M. K. H. & Zavatta, N. *Effect of Bondline Thickness on Fatigue Crack Growth in FM94.* Dataset. 2016. `http://dx.doi.org/10.4121/uuid:1495c951-33e2-43ab-9f41-5ed3b57ba02f`.

29. Zavatta, N. *Influence of adhesive thickness on adhesively bonded joints under fatigue loading* Master thesis (Università di Bologna, 2015). `http://amslaurea.unibo.it/9713/1/zavatta%7B%5C_%7Dnicola%7B%5C_%7Dtesi.pdf.pdf`.

30. ASTM Standard. D5528 - 01 (2007) Standard Test Method for Mode I Interlaminar Fracture Toughness of Unidirectional Fiber-Reinforced Polymer Matrix Composites. `www.astm.org` (2007).

31. Irwin, G. & Kies, J. Critical energy rate analysis of fracture strength. *Welding Journal Research Supplement* **33,** 193s–198s (1954).

32. Irwin, G. Analysis of stresses and strains near the end of a crack traversing a plate. *ASME Journal of Applied Mechanics* **24,** 361–364 (1957).

33. Pascoe, J. A., Alderliesten, R. C. & Benedictus, R. *Characterising resistance to fatigue crack growth in adhesive bonds by measuring release of strain energy.* in *Procedia Structural Integrity* **2** (Elsevier B.V., 2016), 80–87.

34. Pascoe, J., Zavatta, N., Alderliesten, R. & Benedictus, R. *Effect of Bondline Thickness on Fatigue Crack Growth in FM94 Epoxy Adhesive Bonds - Dataset 2.* Dataset. 2017.

35. Cytec Engineered Materials. *FM 94 Adhesive Film Technical Data Sheet.* Data sheet. 2010.

36. Papanicolaou, G. C. *et al.* Experimental and numerical investigation of balanced Boron/Epoxy single lap joints subjected to salt spray aging. *International Journal of Adhesion and Adhesives* **68,** 9–18 (2016).

37. Rybicki, E. F. & Kanninen, M. F. A finite element calculation of stress intensity factors by a modified crack closure integral. *Engineering Fracture Mechanics* **9,** 931–938 (1977).

38. Krueger, R. Virtual crack closure technique: History, approach, and applications. *Applied Mechanics Reviews* **57,** 109–143 (2004).

39. Jokinen, J., Wallin, M. & Saarela, O. Applicability of VCCT in mode I loading of yielding adhesively bonded joints - a case study. *International Journal of Adhesion and Adhesives* **62,** 85–91 (2015).

40. Amaral, L., Yao, L., Alderliesten, R. & Benedictus, R. The relation between the strain energy release in fatigue and quasi-static crack growth. *Engineering Fracture Mechanics* **145,** 86–97 (2015).

41. Khan, R. *et al.* Experimental investigation of the microscopic damage development at mode I fatigue delamination tips in carbon/epoxy laminates. *Jurnal Teknologi* **78,** 33–40 (2016).

Chapter 3

Application of cohesive zone models to cracking of bonded joints

This chapter deals with the application of cohesive zone models to fracture of adhesively bonded joints. Specifically, cohesive models are applied to the study of mode I and mode II crack growth under quasi-static loading. The author gratefully acknowledges Mr. Santiago Scalone [1], who contributed substantially to the work presented in this chapter. In the following, the theoretical framework of cohesive zone models is first introduced and a concise literature review on the topic is presented. Then, we describe the model used in this work and apply it to the case studies in exam. The results of the simulations are compared to experimental results from previous research. The chapter is closed by a discussion of the results, with a particular emphasis on the influence of the input parameters on the solution.

3.1   Introduction

Cohesive Zone Models (CZM) are a class of models developed within the framework of fracture mechanics. The basic idea behind cohesive zone models is that the crack can be modelled as a region where cohesive stresses progressive fade according to a given damage parameter.

Dugdale [2] proposed that the plastic zone ahead of the crack tip in a metal sheet be considered as an extension of the crack, whose surfaces are acted upon by distributed stresses. Barenblatt [3] introduced cohesive forces near the edges of the crack to model brittle fracture. More recently, cohesive models have been widely used to study crack growth in adhesive joints [4–8]

and delaminations in composites [9, 10]. Cohesive models are well suited for the implementation in finite element methods and various formulations have been presented in the literature [9, 11–14]. Among the advantages of using cohesive models for the study of fracture phenomena, there stand:

- the capability to model crack initiation in structures without pre-existing damage, which contrasts with other techniques such as the virtual crack closure technique [15, 16]. Examples of such problems are the prediction of the mechanical properties of adhesive joints [4] or modelling impact damage in composites [17];

- the possibility to reproduce progressive damage of the material through the deterioration of its properties. The laws that enforce the damage behaviour can be quite general, which allows for several sources of damage to be accounted for [18];

- the ability to model crack growth not only under quasi-static loading, but even in fatigue [9, 10, 19–21] and under mixed-mode conditions [22].

Two main classes of cohesive zone models are described in the literature: *intrinsic* models and *extrinsic* ones [23]. In intrinsic models, the cohesive response has an hardening behaviour up to the point of damage onset, which is followed by softening; on the other hand, in extrinsic models the cohesive behaviour is characterized by softening only. In this work an intrinsic cohesive model is adopted, thus we will refer exclusively to this formulation in the following.

Before delving in more detail into the description of the model, we will provide a short review of the literature on the topic of cohesive models applied to delamination and disbonding problems.

3.2   Literature review

Cohesive zone models have been largely applied to the study of crack growth in adhesively bonded joints. Liao et al. [4] used a mixed-mode CZM to model the adhesive bond line in a parametric study of the mechanical properties of a scarf joint. The influence of the adhesive thickness was explicitly taken into account in the properties of the cohesive zone. Azevedo et al. [6] and Figueiredo et al. [8] employed a cohesive law to estimate the shear strength of an end-notch flexure joint, i.e. under predominant mode II conditions. Ribeiro et al. [7] investigated the effects of a defect on the strength of a single lap-joint by using a cohesive model.

Generally, the models presented in the works above are effective in predicting the crack growth in adhesive joints under quasi-static conditions. By modifying the constitutive relationship of the cohesive model it is possible to consider the effects of fatigue, as discussed by Liu et al [20]. Turon et al. [9, 10] developed a cohesive formulation for fatigue loading by including the contribution of the number of cycles to the increase of the damage parameter. This model was then applied to mode I, mode II and mixed-mode delamination in composites. A similar model was presented by de Moura and Gonçalves [21], with an application to fatigue crack growth in adhesively bonded specimens under mode I. The authors reported a good agreement with experimental results for different R-ratios.

In general, cohesive zone models are rather sensitive to the choice of the input parameters. However, it is not always obvious how the different parameters affect the solution as demonstrated by a number of works on this topic. Turon et al. [24] investigated the influence of mesh size and cohesive stiffness on delamination of a double cantilever beam specimen, and compared the model with experimental tests. A clear effect of the mesh size is observed: for too coarse a mesh, the numerical results overshoot the experimental ones; the mesh size effect vanishes if the elements are sufficiently fine. Analogously, an appropriate value of the stiffness is needed. A formula was proposed, which allows to calculate the cohesive stiffness based on adhesive's and adherent's properties. A work by Song et al. [25] extended the findings of Turon et al. to end-notch flexure and mixed mode specimens. Azevedo et al. [6] found a significant effect of both the cohesive strength and fracture energy on cracking of bonded joints in mode II conditions. Recently, Pirondi and Moroni [14] have proposed a cohesive formulation which corrects for the effects of stiffness and cohesive strength. The resulting model proves almost independent ofbasically unaffected by these parameters and is able to predict fatigue crack growth in a double cantilever beam specimen.

To improve the stability of cohesive models, viscous regularization is sometimes used. This technique is also implemented in commercial softwares such as Abaqus [26]. However, the effect of viscosity on the numerical solution is usually not investigated in as much detail as other parameters, see e.g. the works of Liao et al. [4] and of Gustafson and Waas [27]. To the best of the author's knowledge, no extensive study on the influence of viscous regularization on the solution of a cohesive model has been published to date. In this work we will address this topic and discuss the consistency of the regularized solution.
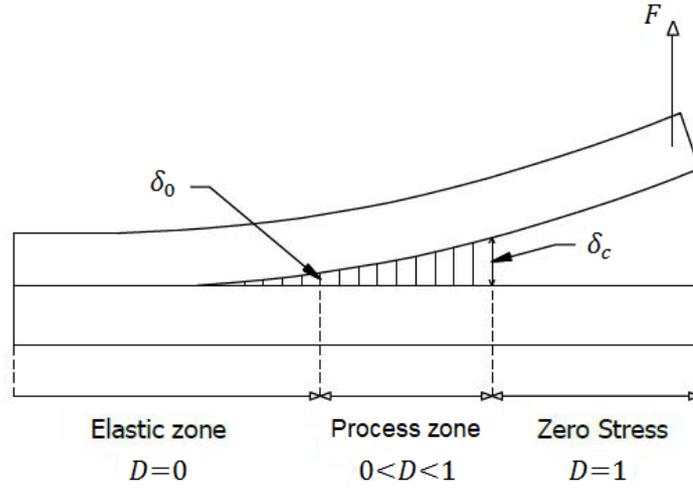
Figure 3.1: Schematics of the cohesive zone around the cracked region. The cracked region, the process zone and the undamaged zone are shown.

3.3   Formulation of the cohesive zone model

Cohesive models assume that the crack develops in an interface region, called cohesive zone. The top and bottom surfaces of this region are held together by cohesive stresses, which vary as a function of the distance between the two surfaces, also referred to as separation. A schematics of the cracking process is shown in Figure 3.1. The cohesive zone can be divided in three main regions: an undamaged region ahead of the crack tip, a zone interested by damage phenomena and a fully cracked zone. Far from the crack tip the material behaves in an elastic way and loading is fully reversible, as no damage occurs. At some point the maximum stress, called cohesive strength, is reached and the material gets damaged, which leads to a decrease of cohesive stresses. The region where damage occurs is called *process zone*. As damaging is irreversible, the material in the process zone does not return to the initial state if external forces are released. The length of the process zone is called *cohesive length*. When the maximum damage is reached, the cohesive zone is no longer able to transfer loads between the upper and lower surface and the cohesive stresses vanish.

The constitutive relationship which links the cohesive stresses to the relative displacement of the two surfaces is called *traction-separation law*. There exists no unique form of the traction-separation law, and several formulations have been proposed. Among them, bilinear, trapezoidal and exponential laws are widely adopted. In general, the performances of the computational model
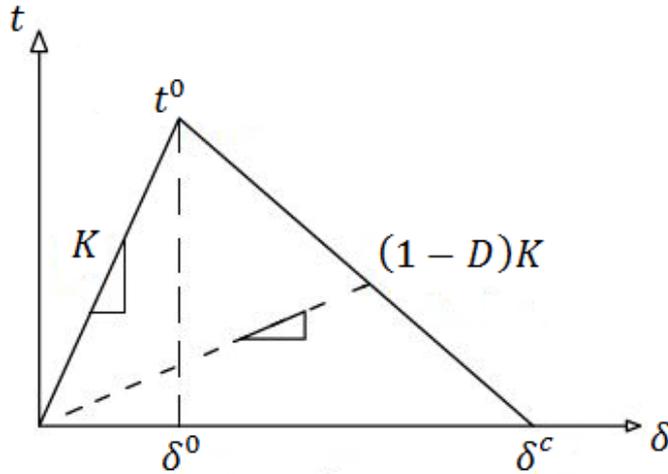
Figure 3.2: Bilinear traction-separation law.

are affected by the particular form chosen for the constitutive law [28]. Independently of their specific form, traction-separation laws generally have some common features. Two distinct regions can be identified: an hardening segment up to the point of maximum traction and a softening one from this point to maximum separation. The hardening region behaves elastically and is defined by an increasing function, which can either be linear or non-linear. The softening behaviour is expressed as a function of a damage parameter, which defines the amount of decreasing of cohesive stress for increasing separation. When unit damage, or equivalently maximum separation, is attained, the cohesive stress goes to zero, i.e. no more forces resist the displacement between the crack surfaces. The area under the traction-separation law must be finite and its value is equal to the fracture energy.

In finite element formulations of the cohesive model, both the upper and lower surface are discretized by a set of interconnected nodes. Separation is therefore related to the distance between the nodes belonging to the upper surface and those on the lower one. The cohesive forces arise in response to the displacements which separate the nodes and resist to the movement of the two surfaces.

Two different finite element formulations of the cohesive model will be discussed in the following: element-based and surface-based [26]. In the element-based formulation, a specific type of elements, called cohesive elements, is introduced in the cohesive zone. The topology of the cohesive elements is the same of traditional elements, from which they differ mostly for their constitutive relationship, which takes the form of a traction-separation law. As cohesive elements have finite, non-zero size, a strain measure is well-

defined. This can be computed by considering the ratio between the relative displacement of element nodes and their initial underformed distance. Thus, the traction-separation law is expressed in terms of stresses and strains in the cohesive element. In the surface-based formulation, the cohesive zone is modelled as a zero-thickness interface region. The traction-separation law is enforced as an interaction between the nodes belonging to the upper surface and those on the lower one. As the initial distance between the two surfaces is zero and no element is defined, no such thing as a cohesive strain is defined. Instead, separation is defined directly as the distance between corresponding nodes on the two surfaces. Analogously, cohesive forces are modelled as nodal traction forces; a surface area is associated to each node and the stress is computed by normalizing the force on this area. Both formulations will be used in the present work.

A bilinear traction-separation law similar to the one used in this work is shown in Figure 3.2. The following input parameters must be specified to fully define the traction-separation law:

- the cohesive strength t^0;

- the displacement δ_0, called characteristic length, which corresponds to maximum traction;

- the value of the area under the curve, i.e. the fracture energy, or, alternatively, the maximum displacement δ^c.

The cohesive strength defines the maximum stress beyond which the material is damaged. For traction-separation laws characterized by linear hardening, such as the one shown in the figure, the elastic region is fully defined by the slope of the curve, named *penalty stiffness*.

Let n, s and t be three coordinates of an orthogonal frame of reference, aligned respectively with the normal to the crack plane and with two directions of the in-plane shear. The displacement vector, i.e. the vector of the relative displacements between upper and lower nodes along the three directions, is denoted by $\boldsymbol{\delta}$. As noted previously, a distinction must be made between element-based and surface-based formulations. In surface-based formulations, separation is taken equal to the relative displacement of the surface nodes, so that $\boldsymbol{\delta}$ also represents the separation vector. For cohesive elements, a strain vector $\boldsymbol{\varepsilon}$ is introduced, with components:

$$\varepsilon_n = \frac{\delta_n}{L_n} \qquad \varepsilon_s = \frac{\delta_s}{L_s} \qquad \varepsilon_t = \frac{\delta_t}{L_t} \tag{3.1}$$

where δ_n, δ_s, δ_t are the components of the displacement vector and L_n, L_s, L_t are the initial distances between the nodes in the undeformed state. The

cohesive stress vector is denoted by $\boldsymbol{t}$ and is made up of the stress components along the three directions. Because of the specific choice of coordinates orientation, the first component of the stress vector, t_n, is the opening stress perpendicular to the crack surface, while the second and third components, t_s and t_t, are respectively the longitudinal and transverse shear. We note here that only positive values of t_n are considered, as compressive stresses do not contribute to damage. In element-based models, the traction-separation law is formulated in terms of element stress and strain vectors; in surface-based models, the surface stress and displacement vectors are used instead. For the sake of simplicity, since the expressions involved in both formulations are formally equal, in the following we will deliberately use $\boldsymbol{t}$ and $\boldsymbol{\delta}$ to denote traction and separation respectively; the corresponding equations for the element-based formulation would be readily obtained by replacing $\boldsymbol{\delta}$ with $\boldsymbol{\varepsilon}$ (computed by Equation (3.1)).

In the linear elastic segment of the traction-separation law, the following relation holds:

$$\boldsymbol{t} = \begin{bmatrix} t_n \\ t_s \\ t_t \end{bmatrix} = \begin{bmatrix} K_{nn} & K_{ns} & K_{nt} \\ K_{sn} & K_{ss} & K_{st} \\ K_{tn} & K_{ts} & K_{tt} \end{bmatrix} \begin{bmatrix} \delta_n \\ \delta_s \\ \delta_t \end{bmatrix} = \mathbf{K}\boldsymbol{\delta} \tag{3.2}$$

where $\mathbf{K}$ is called penalty stiffness matrix and contains the various components of the stiffness. In the general case, it is a symmetric matrix. Under the hypothesis that the normal and shear components of cohesive stress are uncoupled, the cross terms vanish, i.e. $K_{ns} = K_{nt} = K_{st} = 0$, and $\mathbf{K}$ becomes a diagonal matrix.

Equation (3.2) is valid up to the point of damage onset. Different criteria can be used to identify damage initiation. Among them:

- maximum stress criterion: $\max\left\{ \frac{t_n}{t_n^0}, \frac{t_s}{t_s^0}, \frac{t_t}{t_t^0} \right\} = 1$

- maximum separation criterion: $\max\left\{ \frac{\delta_n}{\delta_n^0}, \frac{\delta_s}{\delta_s^0}, \frac{\delta_t}{\delta_t^0} \right\} = 1$

- quadratic stress criterion: $\left(\frac{t_n}{t_n^0}\right)^2 + \left(\frac{t_s}{t_s^0}\right)^2 + \left(\frac{t_t}{t_t^0}\right)^2 = 1$

- quadratic separation criterion: $\left(\frac{\delta_n}{\delta_n^0}\right)^2 + \left(\frac{\delta_s}{\delta_s^0}\right)^2 + \left(\frac{\delta_t}{\delta_t^0}\right)^2 = 1.$

Here t_i^0, δ_i^0 are respectively the cohesive strength and characteristic length along direction i. In this work the quadratic stress criterion is used.

The softening region is described by the scalar damage parameter D. Damage is defined as an increasing function of the equivalent displacement

$\delta_e = \sqrt{\delta_n^2 + \delta_s^2 + \delta_t^2}$. The initial value of damage is equal to zero, while the maximum damage is unit, i.e. $D(\delta_e^0) = 0$ and $D(\delta_e^c) = 1$. For linear softening the following expression can be derived:

$$D(\delta_e) = \frac{\delta_e^c(\delta_e^{\max} - \delta_e^0)}{\delta_e^{\max}(\delta_e^c - \delta_e^0)} \tag{3.3}$$

where $\delta_e^{\max}$ is the maximum equivalent displacement attained during loading. The stiffness in the softening segment is computed as:

$$\boldsymbol{t} = (1 - D)\,\mathbf{K}\boldsymbol{\delta} \tag{3.4}$$

Equation (3.4) can be used to define the loading-unloading path in the softening regime.

Let denote G_I, G_II and G_III the work done by cohesive stresses in directions n, s and t respectively. The fracture energy in the three modes is calculated as the area under the traction-separation curve:

$$
\begin{aligned}
G_\text{Ic} &= \int_0^{\delta_n^c} t_n \, d\delta_n = \frac{1}{2} t_n^0 \delta_n^c \\
G_\text{IIc} &= \int_0^{\delta_s^c} t_s \, d\delta_s = \frac{1}{2} t_s^0 \delta_s^c \\
G_\text{IIIc} &= \int_0^{\delta_t^c} t_t \, d\delta_t = \frac{1}{2} t_t^0 \delta_t^c
\end{aligned}
\tag{3.5}
$$

where the last equality in the equations holds only for the specific case of a bilinear law. The total fracture energy in mixed mode loading, G_Tc, can be computed according to Benzeggagh-Kenane's criterion [29]:

$$G_\text{Tc} = G_\text{Ic} + (G_\text{Sc} - G_\text{Ic})\left(\frac{G_\text{S}}{G_\text{T}}\right)^n \tag{3.6}$$

where $G_\text{S} = G_\text{II} + G_\text{III}$ and $G_\text{T} = G_\text{I} + G_\text{II} + G_\text{III}$ are respectively the work done by shear stresses and the total work, and $G_\text{Sc} = G_\text{IIc} + G_\text{IIIc}$ is the fracture energy in pure shear; the exponent n is determined by experimental data. According to this criterion, unit damage is attained when $G_\text{T}/G_\text{Tc} = 1$. The crack surface is determined by computing the set of nodes where $D = 1$.

From what we have described so far, it is apparent that several parameters are required for the implementation of a cohesive zone model. As the behaviour enforced by the traction-separation law is in fact an artefact of modelling, choosing the correct values of the input parameters is not obvious. Some criteria have been proposed in the literature to guide the choice.

Estimating the penalty stiffness from material properties results in excessively high compliance in adhesive joints, where the stiffness of the adhesive is usually much lower than that of the adherents. Turon et al. [24] argued that in order for the model to give consistent results, the contribution of the cohesive zone to the total compliance must be small. That is to say that the cohesive stiffness must be high compared to that of the surrounding material. They proposed the following expression to determine the value of the penalty stiffness in cohesive elements:

$$K_{nn} = \alpha \frac{E_n}{t} \tag{3.7}$$

where E_n is the elastic modulus of the surrounding material, t is the thickness of the cohesive zone and α must be much greater than one. Turon et al. showed that for $\alpha > 50$, the contribution of the cohesive zone to the total compliance is about 2%. For a bonded joint in which the crack grows inside the adhesive layer, typical values of $\frac{E_n}{t}$ could be around 10^4 N/mm^3 and Equation (3.7) gives a value in the order of $5 \cdot 10^5$ N/mm^3 for the penalty stiffness.

The cohesive strength and the fracture energy are estimated from the material properties of the adhesive. Not only the parameters of the traction-separation law, but also the mesh size must be chosen with care. In particular, a sufficient number of elements must be present in the process zone. We call cohesive length l_{cz} the length of the process zone, which is defined as the distance between the node where the cohesive strength is attained and the crack tip. Turon et al. [24] reviewed several works in the literature and concluded that 3 elements in the process zone were enough to obtain reasonable results for delamination growth in mode I. Moreover, they discussed a number of models to compute the cohesive length. In the present work, Hillerborg's model [30] is used to estimate the cohesive length, which results in the following equation:

$$l_{cz} = E \frac{G_c}{t_{max}^2} \tag{3.8}$$

where E is the elastic modulus, G_c is the fracture energy and t_{max} is the cohesive strength. In mixed-mode loading, t_{max} is computed according to the quadratic stress criterion.

In section 3.6 we will slightly modify the model by introducing a viscous regularization scheme and discuss how this affects the numerical solution.
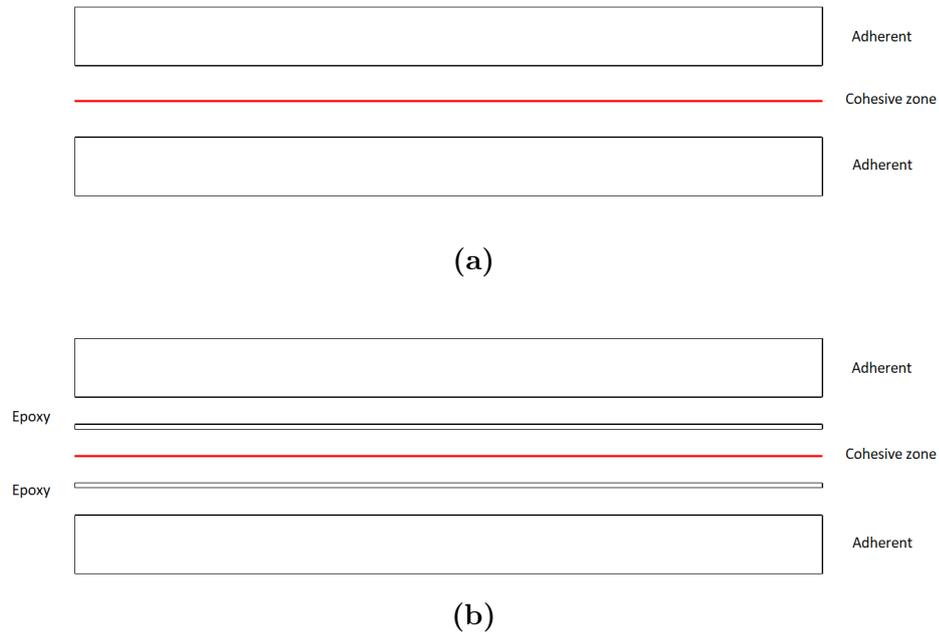
Figure 3.3: Configurations considered for cohesive modelling of quasi-static crack growth.

3.4   Implementation of the cohesive model

In this section, we will present the finite element model implemented in Abaqus for the computation of disbond growth under quasi-static loading.

Two configurations were considered, as shown in Figure 3.3:

- Configuration (a): the aluminium adherents are modelled as isotropic solid elements, while a cohesive layer, e.g. the red line in figure, is used to model the adhesive bond line. The adhesive thickness is not explicitly taken into account.

- Configuration (b): the aluminium beams are modelled as solid elements like in the previous configuration. The adhesive thickness is included by modelling the epoxy layer as isotropic solid elements with elastic-plastic properties. A cohesive zone is placed along the midline of the epoxy layer. The crack is assumed to grow entirely inside the adhesive, thus disbonding at the aluminium-epoxy interface is not taken into account.

Configuration (a) was used to model both mode I and mode II crack growth, employing double cantilever beam (DCB) and end-notched flexure (ENF)

Material	E [MPa]	ν	σ_Y [MPa]
Al 2024-T3	73100	0.33	320
FM94K	3000	0.35	30

Table 3.1: Material properties employed in the double cantilever beam model.

specimens respectively. Configuration (b) was used for mode I modelling of a double cantilever beam specimen. For clarity, the models for the DCB and ENF configurations will be presented separately in the following.

3.4.1   Double cantilever beam model

The geometry of the double cantilever beam model used for mode I crack growth is shown in Figure 3.4. Various models of the DCB specimen were built. Specifically, three models were built following configuration (a), i.e. without considering the epoxy layer: a 2D model with element-based cohesive zone, a 2D model with surface-based cohesive and a 3D one with surface-based formulation. The results for the different cases were compared to one another. Then, a surface-based 2D model following configuration (b) was created, considering an adhesive thickness of 0.2 mm. The results of this model were compared to experimental data.

The mechanical properties of the adherent and adhesive materials are reported in Table 3.1. To evaluate the non-linear plastic behaviour of FM94 the stress-strain curve in Figure 2.13 was used.

The properties of the cohesive zone model are shown in Table 3.2. The input data are tabulated in such an order that the values in column i are the components of stiffness and cohesive strength along direction i. For instance, the value of K_i in column s is the component K_s of the penalty stiffness matrix. The fracture energy G_{Ic} was considered equal to 1700 J/m^2.

The results of quasi-static tests from previous research [31, 32] actually suggest that the value of G_{Ic} might be influenced by the adhesive thickness, and a more thorough investigation would be needed to obtain better measurements of the fracture energy. For configuration (b), G_{Ic} was set equal to 1400 J/m^2, while the cohesive strength was obtained from Figure 2.13, which gives $t_n = 68$ MPa.

For configuration (a), quadrangular plane strain elements of type CPE4R were used to model the aluminium arms in the 2D model, while tetrahedral solid elements C3D8R were employed in the 3D model. The cohesive zone
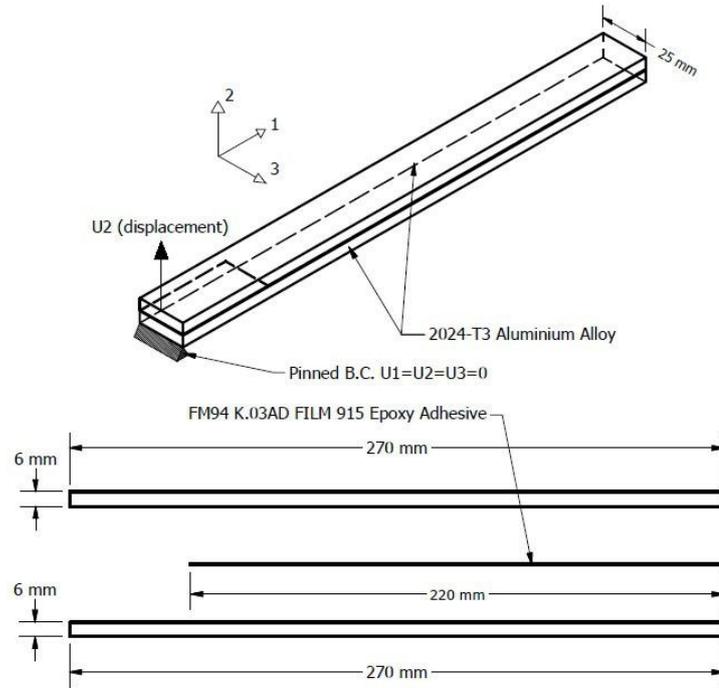
Figure 3.4: Geometry of the double cantilever beam model. The material and the boundary conditions are also shown.

Parameter	n	s	t
K_i [N/mm^3]	$5 \cdot 10^5$	$1 \cdot 10^5$	$1 \cdot 10^5$
t_i [MPa]	50	30	30

Table 3.2: Cohesive properties of the double cantilever beam model. Values in column i are the components of the stiffness and cohesive strength in the corresponding direction.
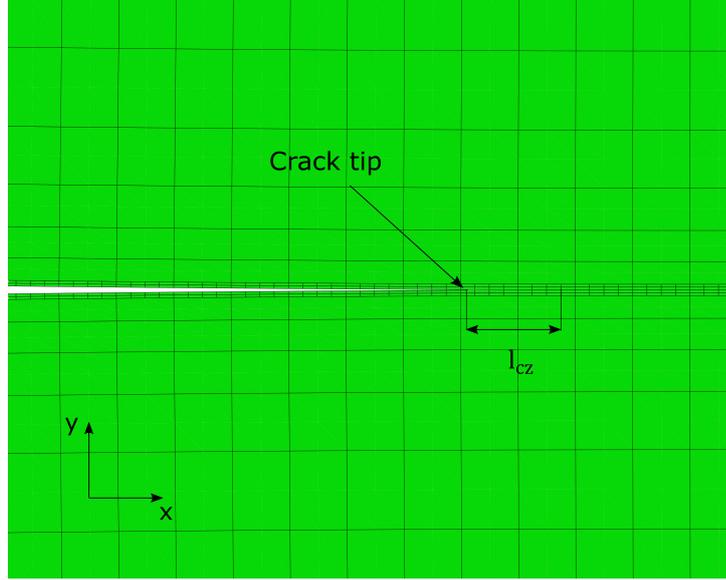
Figure 3.5: Mesh used for the 2D model with configuration (b). Also shown are the right-most node where $D = 0.99$, denoted as the crack tip, and the cohesive length computed accordingly.

was modelled by either COH2D4 elements and a surface-based cohesive interaction. The mesh size was refined around the adhesive bondline, so to have a sufficient number of elements in the cohesive zone. Equation (3.8) can be used to estimate the size of the cohesive elements: considering the mechanical properties of Al 2024 and FM94, a cohesive zone length of about 50 mm is computed; Turon et al. [24] suggested that a minimum of 3 elements be present in the cohesive zone, which would result in an element size of approximately 16 mm. In our model, a finer mesh was used, with elements as small as 0.25 mm in the 2D model and 0.6 mm in the 3D one.

We note here that the configuration with the epoxy layer explicitly modelled, i.e. configuration (b), is more critical in terms of mesh refinement. As in this case the cohesive zone is fully embedded in the epoxy, a much lower stiffness enters in Equation (3.8), resulting in a cohesive zone length $l_{cz} \approx 1.7$ mm. A longitudinal element size of 0.25 mm was used, which corresponds to having 8 elements in the cohesive length, while 4 elements were stacked through the adhesive thickness. Both the adherents and the epoxy layer were meshed with second-order plain strain elements of type CPE8R.

A detailed view of the mesh around the crack tip is given in Figure 3.5. The cohesive length l_{cz} is also shown, computed as the distance between the node where cohesive strength is attained and the crack tip. Here, the cohesive

length is equal to 1.625 mm, which is in very good agreement with the value computed by Equation (3.8). However, the point identified as the crack tip in the figure corresponds to the right-most node where damage exceeds 0.99; considering the node where $D = 1$ instead causes the crack tip to shift to the left, and the cohesive length becomes about 5.5 mm. This is not related to the mesh size: a test run with the mesh refined to a longitudinal element size of 0.125 mm, i.e. half of the size considered here, resulted in the same values of the cohesive length found here. In fact, this effect is caused by the linear traction-separation law used. Equation (3.3) shows that damage increases slowly with separation for $0.99 < D < 1$; moreover, in a DCB specimen the separation of the crack surfaces is small close to the crack tip, due to the limited rotation of the adherents. Thus, a relatively long region is observed before the crack tip, in which the cohesive elements are almost but not entirely cracked. Anyway, since the cohesive length computed by Equation (3.8) results in smaller element size, we sticked to that value in the present work.

The simulations were run under displacement control, similarly to previous experimental tests [32–34]. The loading blocks were not explicitly modelled; a pinned constraint, i.e. zero displacements in all directions and free rotations, was used instead, as shown in Figure 3.4. Maximum displacements of 30 mm and 40 mm were applied in configuration (a), while 15 mm was used for configuration (b).

An initially disbonded region with a length of 50 mm is considered, which is expected to be consistent with the pre-cracked length provided by the insert in the real specimens.

The results of the double cantilever beam models are presented in section 3.5.1.

3.4.2   End-notched flexure model

The geometry of the end-notched flexure model used for mode II crack growth is illustrated in Figure 3.6. The geometry and materials shown in the figure follow those of the specimens used in a work by Budzik et al. [35], which was taken as a reference to validate the cohesive model. For the ENF model, only configuration (a) was used, neglecting the thickness of the epoxy layer. Two models were built: a 2D and a 3D one.

The properties of the cohesive zone model are shown in Table 3.3. The data follow the same order introduced in Table 3.2. The following values were used for the fracture energy of EA9395 epoxy: $G_{\text{Ic}} = 20$ J/m^2 and $G_{\text{IIc}} = G_{\text{IIIc}} = 200$ J/m^2. Equation (3.6) was used to compute the total fracture energy.
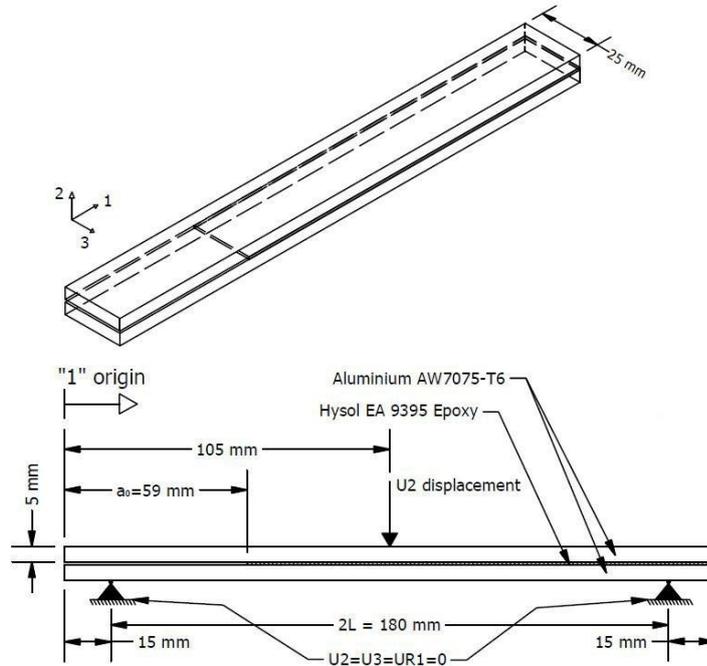
Figure 3.6: Geometry of the end-notched flexure model.

Parameter	n	s	t
K_i [N/mm^3]	$5 \cdot 10^5$	$1 \cdot 10^5$	$1 \cdot 10^5$
t_i [MPa]	55.6	29.7	29.7

Table 3.3: Cohesive properties of the end-notched flexure model. Values in column i are the components of the stiffness and cohesive strength in the corresponding direction.

Quadrangular plane strain elements of type CPE4R were used to model the aluminium arms in the 2D model, while tetrahedral solid elements C3D8R were employed in the 3D model. The surface-based cohesive formulation was used in both the 2D and 3D model.

Similarly to the double cantilever beam specimen, the mesh size was refined around the adhesive bondline, so to appropriately model the cohesive zone. A minimum mesh size of about 0.25 and 0.5 mm was used in the 2D and 3D case respectively.

In order to reproduce the supports of the test machine, roller constraints were enforced at the two sides of the specimen, as shown in Figure 3.6. A vertical displacement was applied in the middle; maximum values of 2.5 mm and 2 mm were used respectively in the 2D and 3D model. An initial crack length of 59 mm is considered.

The results of the end-notched flexure models are presented in section 3.5.2.

3.5   Results and discussion

In the following we will show the results of the numerical simulations. For the double cantilever beam model, first the results obtained with configuration (a) in the 2D and 3D cases are compared; after that, the results of configuration (b) are presented and compared to experimental findings [34]. For the end-notched flexure specimen, the 2D and 3D simulations are compared to experimental results from the literature [35].

3.5.1   Double cantilever beam results

Figure 3.7 shows the load-displacement curve of the DCB specimen as computed using configuration (a), comparing the three cases under consideration. The lines of the 2D and 3D cases basically overlap on the entire domain, with a small difference (about 5%) in the value of the maximum load, the 2D surface-based model giving the highest figure.

The crack growth computed in the three cases is shown in Figure 3.8. Since the 3D model actually gives the cracked area, the equivalent length shown in the graph for comparison with the 2D cases is obtained by averaging on the specimen width. The values of the crack length calculated by the three models differ by no more than 3% from one another.

Together, Figures 3.7 and 3.8 show that for a double cantilever beam specimen the three models give almost identical results, computing the same force and crack length for a given applied displacement. Incidentally, this also means that the same strain energy release rate is calculated according
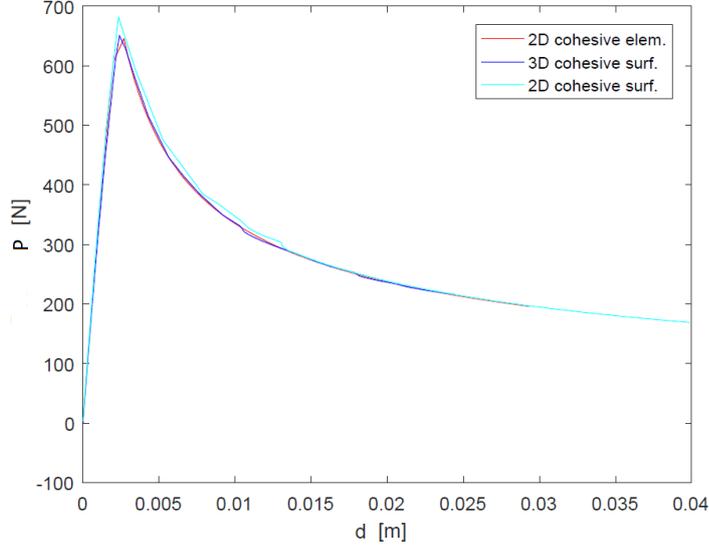
Figure 3.7: Load-displacement curve of the double cantilever beam specimen computed by the three models using configuration (a): 2D with cohesive elements, 2D with surface-based cohesive formulation and 3D. All quantities are in S.I. units.

to the modified beam theory, i.e. Equation 2.1 in the previous chapter. This is also shown explicitly in Figure 3.9, where the crack resistance curve, G_I vs a, is plotted for the three cases. We observe that the computed fracture energy tends to the input value of 1700 J/m^2.

The shape of the crack front as computed by the 3D model can be seen in Figure 3.10. Several positions along the specimen length are shown, in order to evaluate if the crack shape varies during propagation. No significant change of the crack shape is observed in the present results, thus the crack remains basically self-similar. The crack front is slightly curved, with the middle of the crack which is a bit more advanced than the edges. This effect has already been reported in the literature, and has been explained by Budzik et al. [36] in terms of the distribution of strain energy density at the crack front. In our case, the crack front exhibits only little curvature, which makes it reasonable to approximate it to a straight line. This could explain why the simpler 2D models give almost the same crack length of the 3D one, as noted earlier.

In the following, we will present a comparison between the results obtained by configuration (b) and data from previous experimental tests. The specimens used for comparison belong to the same batches discussed in chapter 2. The specimens were tested in quasi-static conditions under displace-
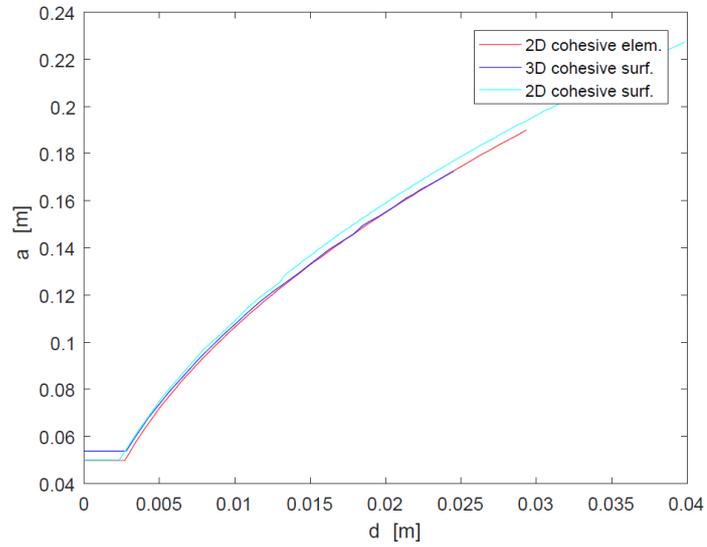
Figure 3.8: Crack length in the double cantilever beam model as a function of the applied displacement. The three cases of configuration (a) are shown. All quantities are in S.I. units.
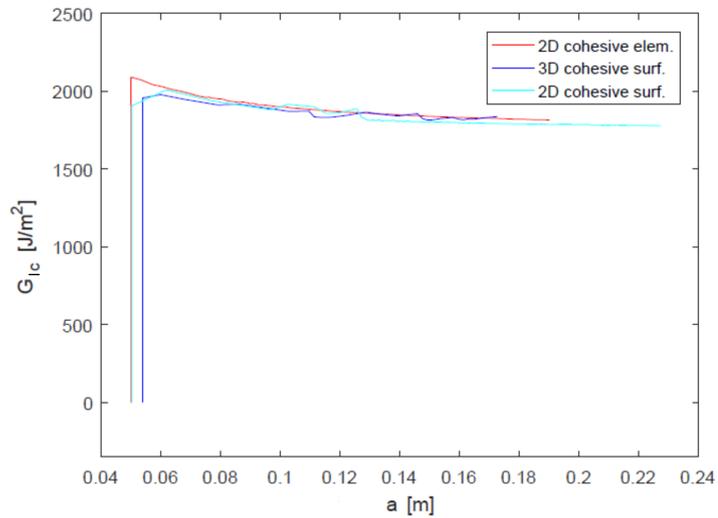
Figure 3.9: Strain energy release rate G_{I} computed by the modified beam theory, plotted as a function of the crack length.
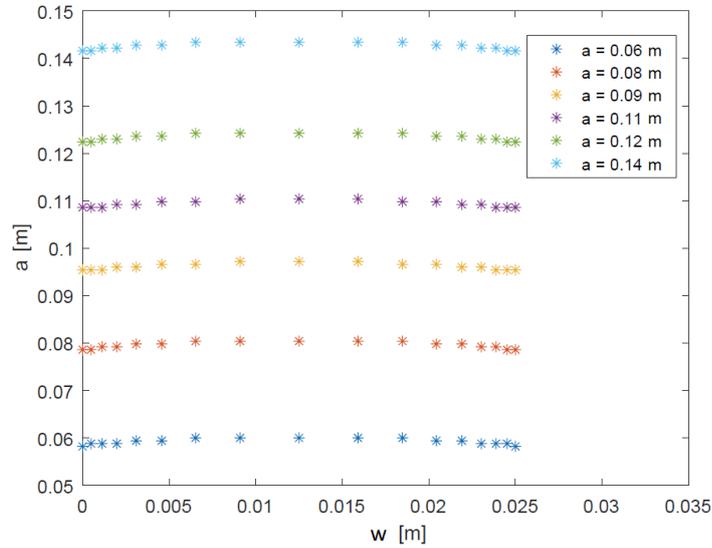
Figure 3.10: Crack shape computed by the 3D model. The crack front at different positions along the specimen length is shown.
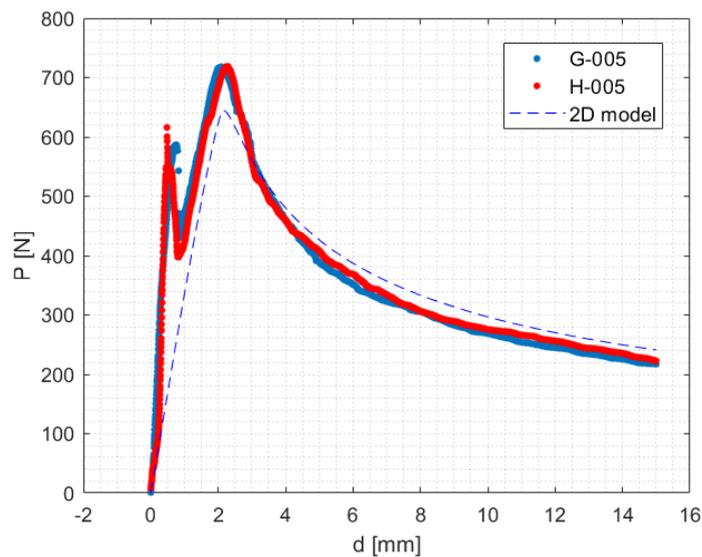
Figure 3.11: Load-displacement curve as computed by the 2D model with configuration (b). Data measured in double cantilever beam specimens, i.e. G-005 and H-005, in previous quasi-static tests are also shown for comparison.

ment control and the load was measured by the test machine. A displacement rate equal to 1 mm/min was applied throughout the test. The crack propagation was measured by a camera aiming at the side of the specimen. The experimental results are shown here for the sole purpose of validating the cohesive model; we refer the reader to earlier works [32, 34] for more information on the tests.

The load-displacement curve computed by the model and the ones measured in the tests are plotted in Figure 3.11. We can identify two distinct behaviours in the curves: a linear increase of the load at the beginning of the test and a non-linear softening in the second part. In the experimental tests, the linear increase is interrupted by an abrupt drop of the force, which is followed by a decrease of the stiffness. The reason for this behaviour is to be found in the pre-cracking of the insert used to initiate the crack. Since the insert is weakly bonded to the adherent, fracture is likely to start at the insert-adherent interface; then, the crack jumps into the bulk adhesive, which offers more resistance to crack growth. This would explain the two peaks observed in the load-displacement curve: detaching of the insert from the adherent is responsible for the decrease of force after the first peak, while the second peak, i.e. the absolute maximum of the force, corresponds to the crack starting to grow in the bulk adhesive.

Clearly, the cohesive model is not able to say anything about insert precracking, so that it predicts a roughly linear increase of the force until the point where adhesive cracking starts. The displacement for which the crack starts propagating in the model is basically equal to that in the real specimens. On the other hand, the maximum force computed by the cohesive model is about 12% lower than the measured one, which means that the specimens resist more to the applied displacement. A possible explanation for this could be that the insert does not completely debond from the adherents and an additional force is required to fully detach it.

During crack propagation, the force calculated by the model is approximately 5% more than the experimental one, which seems quite an accurate result.

Figure 3.12 shows a comparison between the crack length calculated by the model and the one measured with the camera. The computed line basically overlaps the experimental data, with an error within a 3% range.

Together, the data in Figures 3.11 and 3.12 allow us to compute the strain energy release rate using the modified beam theory method presented in section 2.5. This results in the crack resistance curve plotted in Figure 3.13.

Clearly, the strain energy release rate is not constant through the length of the specimen. The SERR computed from the experimental data is maximum when the crack starts propagating and reaches a steady value during crack
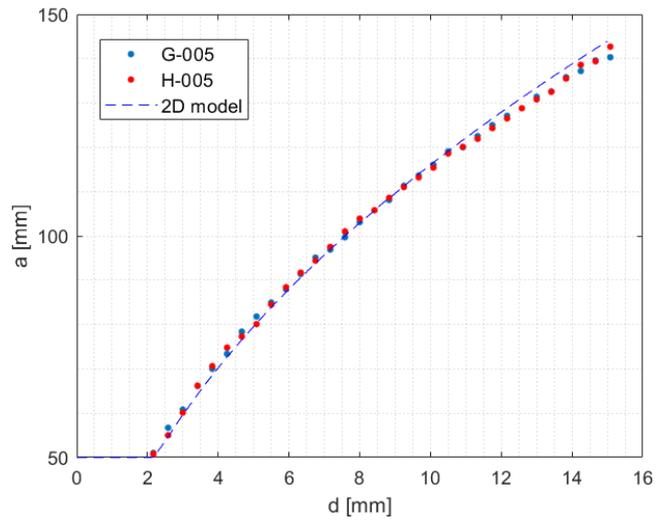
Figure 3.12: Crack length computed by the model with configuration (b), plotted as a function of the applied displacement. The crack measured with the camera in specimens G-005 and H-005 is shown for comparison.
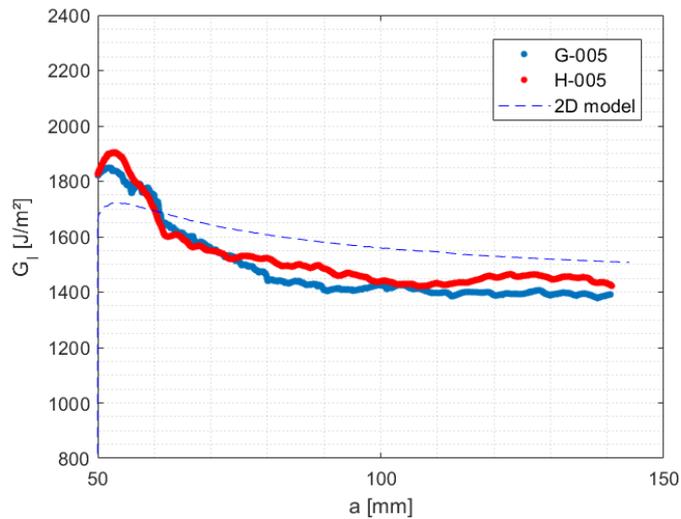
Figure 3.13: Comparison of the crack resistance curves, G_{I} vs a, computed by the model and obtained from experimental data.

growth. The same trend can also be seen in the curve calculated by the model, even though the value of the SERR remains much more constant during crack propagation compared to the experimental data. Given that the crack length is practically the same in both cases (see Figure 3.12), this is due to the discrepancy between the measured and predicted values of the force, as discussed previously.

Looking from an energetic standpoint, it means that, at crack onset, more energy is released by crack growth in the real specimens than in the model. Since in the cohesive formulation a constant value of the fracture energy was used, we expect that only processes in which the fracture energy is constant are reproduced. Hypothesizing that the energy required to advance the crack when the crack is small is higher than the nominal value of the fracture energy chosen in the traction-separation law, this would explain why a higher G_{I} is obtained from experimental data compared to the results of the model. In the second part of the curve, the SERR computed by the model follows the experimental one within a limited error range. The numerical value is slightly overestimated, something which has to do with the predicted force being higher than the measured one, as shown earlier in Figure 3.11.

3.5.2   End-notched flexure results

Figure 3.14 shows the load-displacement curve computed by the ENF model. The results of the 2D and 3D models are shown for comparison.

The curve can be divided in three distinct regions: linear elastic loading, softening and inelastic loading. The first segment corresponds to the response of the undamaged specimen. If the applied displacement is removed, the specimen returns to its initial state with an elastic behaviour. When the maximum force is attained, the specimen starts to crack and the stiffness drops abruptly, which is seen as softening in the load-displacement graph. At some point, the force starts to increase again with the displacement and the stiffness decrease becomes smoother. We called this behaviour inelastic loading because it involves damage occurring in the specimen: a new state of equilibrium is reached if the displacement is released, which is different from the initial one.

Differently from what was observed in mode I, where all models gave similar results, here the force calculated by the 2D model is slightly different from the one computed in the 3D case. The maximum force is reached earlier in the 2D case, and its value is moderately higher. The difference between the two is about 5% during linear elastic loading and increases to approximately 10% in the inelastic regime.

The crack growth computed in the two cases is plotted in Figure 3.15 as
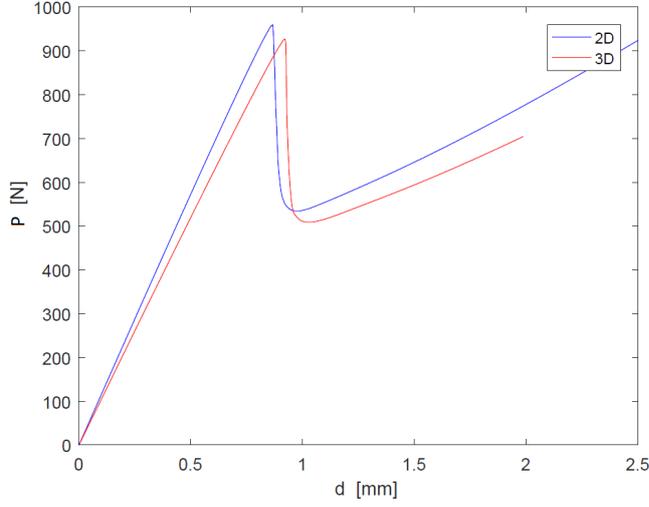
Figure 3.14: Load-displacement curve of the end-notched flexure specimen computed by the 2D and 3D models.

a function of the applied displacement. The crack length for the 3D model is obtained by averaging the cracked area on the specimen width. The curves of the two models basically overlap, except for a little shift in the crack onset, which occurs slightly earlier in the 2D model.

Clearly, the crack is initially unstable and grows almost instantaneously until it reaches the centre of the specimen, i.e. the point where the displacement is applied. Once the crack gets past this point, it grows in a stable way as the specimen is bent.

Figures 3.14 and 3.15 show that the maximum force is attained just before crack propagation starts. The softening behaviour observed in the load-displacement curve corresponds to the unstable crack growth, while the stable cracking is responsible for the inelastic loading. The transition between the softening regime and inelastic loading occurs in correspondence of the point of application of the load. By a comparison of the two graphs, it is apparent that the different positions of the force peak observed in the 2D model and in the 3D one are a consequence of the shifted crack onset.

The strain energy release rate G_{II} was computed according to the following equation:

$$G_{\text{II}} = \frac{9a^2 P^2}{16w^2 t^3 E_f} \tag{3.9}$$

where a is the crack length, P is the applied load, w and t are respectively the specimen width and thickness, and E_f is the flexural modulus. This was calculated from the slope of the load-displacement curve as $E_f = \frac{l^3}{4wt^3}\frac{\partial P}{\partial d}$,
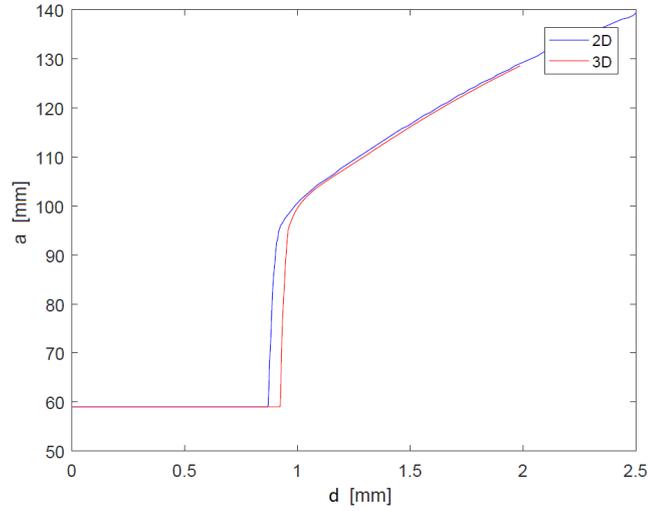
Figure 3.15: Crack length in the end-notched flexure model as a function of the applied displacement. The results of the 2D and 3D models are shown.

being l the specimen length.

The crack resistance curve G_{II} vs a resulting from the 2D model is plotted in Figure 3.16. Experimental results from a work by Budzik et al. [35] are also shown for comparison. Several methods for computing G_{II} were compared by Budzik et al., all giving similar results. Here, the data from Shear Compliance method (SC) and from Simple Beam Theory (SBT) are reported. In the SC method, the variation of compliance of the specimen was measured directly with a digital image correlation technique and used to compute the strain energy release rate. In the SBT method, the value of G_{II} is derived analytically by assuming that the adhesive layer is infinitely rigid. The numerical results computed according to Equation (3.9) basically overlap the experimental data for $a < 90$ mm, i.e. before the crack reaches the point of application of the load. Once the crack grows past this point the SERR found experimentally increases faster than the one computed by the model.

The shape of the crack front computed by the 3D model can be seen in Figure 3.17. Several positions along the specimen length are shown. The crack front is almost straight along the width of the specimen. No significant change of the crack shape is observed.
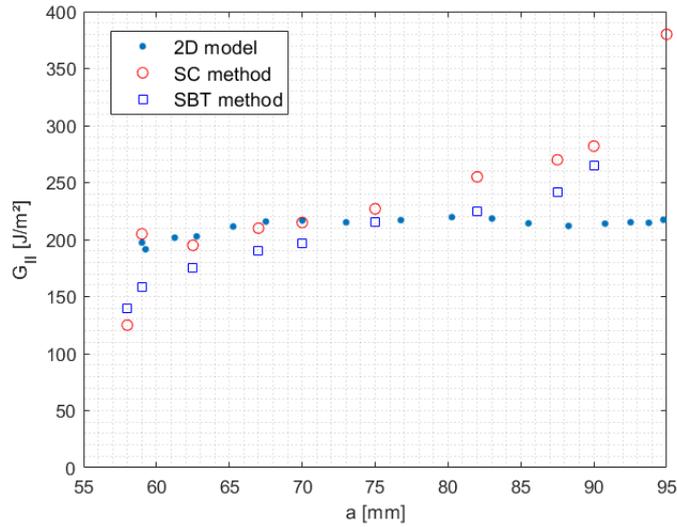
Figure 3.16: Crack resistance curve, G_{II} vs a, computed by the 2D model. Also shown are the experimental results calculated by Budzik et al. [35] using the shear compliance (SC) and simple beam theory (SBT) methods.
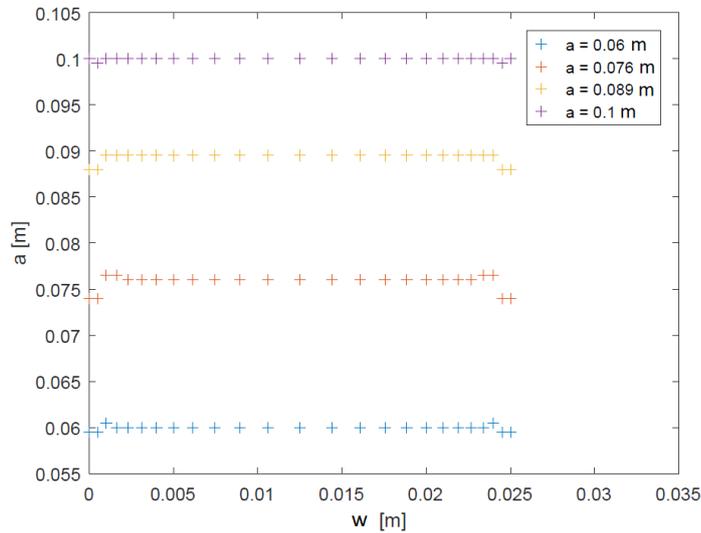
Figure 3.17: Crack shape computed by the 3D model. The crack front remains almost straight during crack propagation.

3.6   Effect of viscous regularization on the solution of cohesive zone models

Cohesive zone models often involve numerical difficulties in the convergence of the solution, which are caused by the softening behaviour of the traction-separation law. In order to overcome these difficulties, numerical techniques can be used to stabilize the solution [4, 27].

While input parameters such as penalty stiffness and mesh size have been discussed by a number of authors and they have been proven to significantly affect the results, other parameters involved in the numerical solution seems to receive less attention. It is the author's opinion that understanding the effect of these parameters on cohesive models would greatly benefit the trustworthiness of their results. In this section we will discuss the viscous regularization technique and its influence on the numerical results of double cantilever beam model.

Several viscous regularization schemes have been applied to cohesive zone models [37, 38]. Here, we will refer to the regularization scheme which is adopted in the Abaqus/Standard solver [26]. The damage parameter D is modified by introducing a rate dependence, which is expressed by the following equation:

$$\frac{\mathrm{d}D_\mu}{\mathrm{d}t} = \frac{1}{\mu}\left(D - D_\mu\right) \tag{3.10}$$

where μ is called artificial viscosity. The expression of cohesive stress in the softening regime, i.e. Equation (3.4), thus becomes:

$$\boldsymbol{t} = \left(1 - D_\mu\right)\mathbf{K}\boldsymbol{\delta} \tag{3.11}$$

The idea behind the regularization scheme is that D_μ tends to D as $\frac{t}{\mu} \to \infty$, which implies that the value of the artificial viscosity must be small compared to the characteristic time scale of the model.

In Appendix A we prove that $D_\mu = D$ if $\mu \to 0$ for a general damage formulation. The following inequality is derived, which establishes an upper and a lower bound on the viscous damage D_μ:

$$D\left[1 - e^{\frac{t_0-t}{\mu}}\right] - \mu^{\frac{1}{2}}\left[1 - e^{2\frac{t_0-t}{\mu}}\right]^{\frac{1}{2}}\varepsilon_D \leq D_\mu \leq D\left[1 - e^{\frac{t_0-t}{\mu}}\right] \tag{3.12}$$

The value of ε_D can be computed as follows:

$$\varepsilon_D = \frac{\sqrt{2}}{2}\left[\int_{t_0}^t \left(\frac{\mathrm{d}D}{\mathrm{d}t}\right)^2 d\tau\right]^{\frac{1}{2}} = \frac{\sqrt{2}}{2}\left[\int_{\delta_e^0}^{\delta_e} \left(\frac{\mathrm{d}D}{\mathrm{d}\delta}\right)^2 \frac{\mathrm{d}\delta}{\mathrm{d}t}\, d\delta\right]^{\frac{1}{2}} \tag{3.13}$$
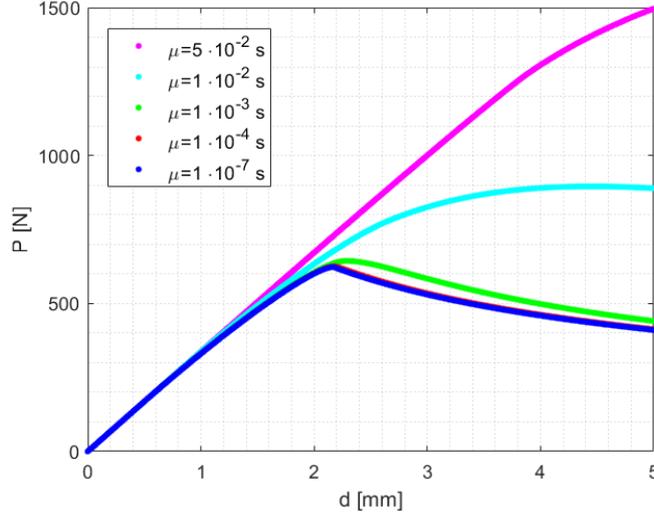
Figure 3.18: Effect of viscosity on the load-displacement curve of a double cantilever beam specimen. The curves overlap for values of $\mu < 10^{-3}$ s.

The derivative $\frac{\mathrm{d}D}{\mathrm{d}\delta}$ can be calculated knowing the expression of the traction-separation law. For linear softening it is equal to:

$$\frac{\mathrm{d}D}{\mathrm{d}\delta} = \frac{\delta^{\mathrm{c}}\delta^{0}}{\delta^{2}(\delta^{\mathrm{c}} - \delta^{0})} \tag{3.14}$$

where $\delta = \delta_e$ in mixed-mode conditions. The derivative $\frac{\mathrm{d}\delta}{\mathrm{d}t}$ should be computed by relating crack separation to time for the specific load case in exam.

To test the influence of viscosity on the solution, we run numerical simulations with five different values of μ, ranging from 10^{-7} s to $5 \cdot 10^{-2}$ s. The model used in the simulations was the DCB in configuration (b) already described in section 3.4.1. The penalty stiffness and the cohesive strength were set according to Table 3.2, while the fracture energy was 1400 J/m^2.

Figure 3.18 shows the effect of viscosity on the load-displacement curve of the specimen. Clearly, the force predicted by the cohesive model is wrong if too high a viscosity is used. In particular, the model overestimates the specimen stiffness and fails to reproduce the crack growth. There seems to be an asymptotic behaviour with decreasing viscosity, in that values of μ lower than 10^{-3} produce similar results.

Figure 3.19 illustrates how the traction-separation law is affected by μ. For low values of the viscosity, the curves overlap almost perfectly the theoretical traction-separation law for the inviscid case, i.e. that with $\mu = 0$. More viscous stabilization, i.e. higher μ, results in an increased value of the
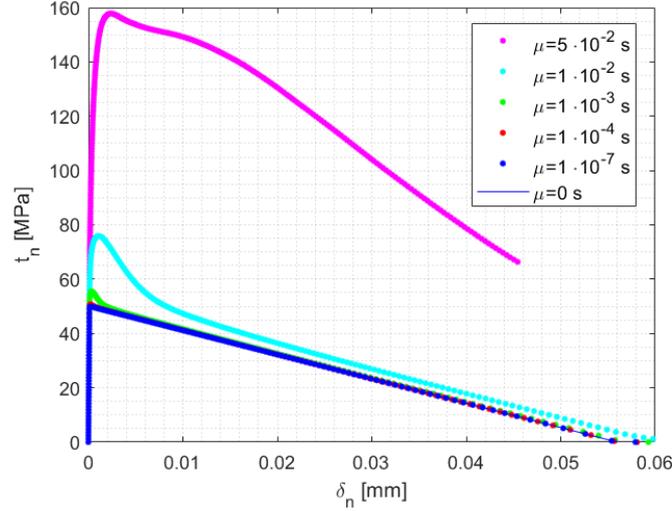
Figure 3.19: Comparison of the traction-separation curves obtained for different values of the viscosity μ. The inviscid law is plotted for comparison.

cohesive strength. Moreover, the area under the curve gets larger, which means that more energy is required to reach fracture. Thus, if viscosity is too high, it produces a spurious increase of the fracture energy, which makes it harder to propagate a crack in the cohesive zone and results in an overly stiff model. This explains the behaviour observed in Figure 3.18 for high values of μ.

The artificial increase of fracture energy can be seen explicitly in Figure 3.20. Here, the area under the traction-separation law, i.e. the fracture energy G_{c}, is plotted against the value of the viscosity. For $\mu < 10^{-3}$ s, the value of the fracture energy is equal to the nominal value $G_{\mathrm{c}} = 1400$ J/m^2, up to an error of 1%. For $\mu = 0.05$ s, the fracture energy increases up to 5400 J/m^2, with an error of almost 300%.

From the results above, it is apparent that using a viscous regularization scheme to stabilize the solution of the cohesive model can potentially affect the results, even in an undesired way. If large values of the viscosity are used, it is therefore advisable to perform a sensitivity analysis to ensure that the numerical results are consistent.

3.7   Conclusions

Cohesive zone models were applied to the study of quasi-static crack growth in adhesively bonded joints under mode I and mode II conditions. To this
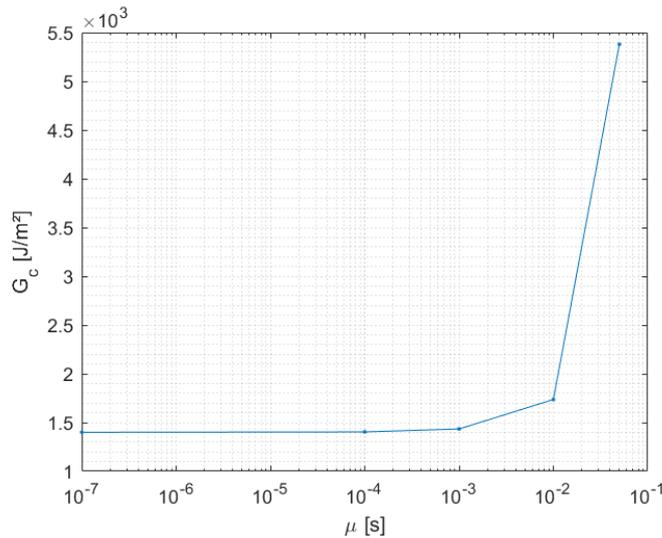
Figure 3.20: Fracture energy G_c plotted as a function of the artificial viscosity. The nominal value of G_c is equal to 1400 J/m^2.

end, double cantilever beam and end-notched flexure specimens were modelled. Different models were compared, either in 2D and 3D configurations. In one double cantilever beam model, the adhesive thickness was explicitly modelled. The results of mode I simulations were compared to experimental data from previous research, while results from the literature were used as a reference for mode II simulations.

The double cantilever beam model proved able to compute the crack growth and strain energy release rate with a good accuracy. No substantial difference was observed for the 2D and 3D models in mode I. The fracture energy chosen in the constitutive relationship of the cohesive model was seen to have an influence on the computed strain energy release rate, which makes it important to accurately estimate its value.

Consistent strain energy release rates were computed by the end-notched flexure model before the crack reaches the point of application of the load. When the crack grows beyond this point, the model tends to underestimate the value of the SERR.

In the end of the chapter, a viscous regularization scheme to stabilize the solution of cohesive models was discussed. The effect of artificial viscosity on the numerical results of a double cantilever beam model was investigated. The constitutive relationship of the cohesive model was found to be affected by viscosity. In particular, unexpectedly high values of the fracture energy were observed for high viscosity. This produced an artificial stiffening of

the cohesive model and resulted in underestimating the crack growth. A sufficiently low value of the viscosity is necessary to obtain consistent results. An expression to estimate the error of the regularized solution was derived, and its application to a cohesive model with linear softening was discussed.

References

1. Scalone, S. *A numerical evaluation of mode I & II damage propagation in composites materials.* Master thesis (Università di Bologna, 2018).

2. Dugdale, D. Yielding of steel sheets containing slits. *Journal of the Mechanics and Physics of Solids* **8,** 100–104. `https://linkinghub.elsevier.com/retrieve/pii/0022509660900132` (1960).

3. Barenblatt, G. I. The Mathematical Theory of Equilibrium Cracks in Brittle Fracture. *Advances in Applied Mechanics* **7,** 55–129 (1962).

4. Liao, L., Huang, C. & Sawa, T. Effect of adhesive thickness, adhesive type and scarf angle on the mechanical properties of scarf adhesive joints. *International Journal of Solids and Structures* **50,** 4333–4340. `http://dx.doi.org/10.1016/j.ijsolstr.2013.09.005` (2013).

5. Ji, G., Ouyang, Z., Li, G., Ibekwe, S. & Pang, S. S. Effects of adhesive thickness on global and local mode-I interfacial fracture of bonded joints. *International Journal of Solids and Structures* **47,** 2445–2458. `http://dx.doi.org/10.1016/j.ijsolstr.2010.05.006` (2010).

6. Azevedo, J. C., Campilho, R. D., da Silva, F. J., Faneco, T. M. & Lopes, R. M. Cohesive law estimation of adhesive joints in mode II condition. *Theoretical and Applied Fracture Mechanics* **80,** 143–154. `http://dx.doi.org/10.1016/j.tafmec.2015.09.007` (2015).

7. Ribeiro, F. M., Campilho, R. D., Carbas, R. J. & da Silva, L. F. Strength and damage growth in composite bonded joints with defects. *Composites Part B: Engineering* **100,** 91–100. `http://dx.doi.org/10.1016/j.compositesb.2016.06.060` (2016).

8. Figueiredo, J. C., Campilho, R. D., Marques, E. A., Machado, J. J. & da Silva, L. F. Adhesive thickness influence on the shear fracture toughness measurements of adhesive joints. *International Journal of Adhesion and Adhesives* **83,** 15–23. `http://dx.doi.org/10.1016/j.ijadhadh.2018.02.015` (2018).

9. Turon, A. T. *Simulation of delamination in composites under quasi-static and fatigue loading using cohesive zone models.* PhD thesis (University of Girona, 2006).

10. Turon, A., Costa, J., Camanho, P. P. & Dávila, C. G. Simulation of delamination in composites under high-cycle fatigue. *Composites Part A: Applied Science and Manufacturing* **38,** 2270–2282 (2007).

11. Park, K. & Paulino, G. H. Computational implementation of the PPR potential-based cohesive model in ABAQUS: Educational perspective. *Engineering Fracture Mechanics* **93,** 239–262. `http://dx.doi.org/10.1016/j.engfracmech.2012.02.007` (2012).

12. Giuliese, G., Pirondi, A. & Moroni, F. A Cohesive Zone Model for Three-dimensional Fatigue Debonding/Delamination. *Procedia Materials Science* **3,** 1473–1478. `http://dx.doi.org/10.1016/j.mspro.2014.06.238` (2014).

13. Musto, M. & Alfano, G. A fractional rate-dependent cohesive-zone model. *International Journal for Numerical Methods in Engineering* **103,** 313–341. `http://doi.wiley.com/10.1002/nme.4885` (2015).

14. Pirondi, A. & Moroni, F. Improvement of a cohesive zone model for fatigue delamination rate simulation. *Materials* **12** (2019).

15. Rybicki, E. F. & Kanninen, M. F. A finite element calculation of stress intensity factors by a modified crack closure integral. *Engineering Fracture Mechanics* **9,** 931–938 (1977).

16. Krueger, R. Virtual crack closure technique: History, approach, and applications. *Applied Mechanics Reviews* **57,** 109–143 (2004).

17. Falaschetti, M. P. *Experimental and Numerical Evaluation of Impact Damage Tolerance in composite materials* PhD thesis (Università di Bologna, 2017). `http://amsdottorato.unibo.it/8078/`.

18. Costa, M., Viana, G., Créac'hcadec, R., da Silva, L. F. & Campilho, R. D. A cohesive zone element for mode I modelling of adhesives degraded by humidity and fatigue. *International Journal of Fatigue* **112,** 173–182. `https://doi.org/10.1016/j.ijfatigue.2018.03.014` (2018).

19. Lucas, L. J., Black, T. M. & Jones, D. P. Use of cohesive elements in fatigue analysis. *American Society of Mechanical Engineers, Pressure Vessels and Piping Division (Publication) PVP* **2,** 13–25 (2008).

20. Liu, J., Li, J. & Wu, B. The cohesive zone model for fatigue crack growth. *Advances in Mechanical Engineering* **2013** (2013).

21.   De Moura, M. F. & Gonçalves, J. P. Cohesive zone model for high-cycle fatigue of adhesively bonded joints under mode i loading. *International Journal of Solids and Structures* **51,** 1123–1131. `http://dx.doi.org/10.1016/j.ijsolstr.2013.12.009` (2014).

22.   Moroni, F. & Pirondi, A. *Cohesive zone model simulation of fatigue debonding along interfaces* in *Procedia Engineering* **10** (Elsevier Ltd, 2011), 1829–1834.

23.   Kubair, D. V. & Geubelle, P. H. Comparative analysis of extrinsic and intrinsic cohesive models of dynamic fracture. *International Journal of Solids and Structures* **40,** 3853–3868 (2003).

24.   Turon, A., Dávila, C. G., Camanho, P. P. & Costa, J. An engineering solution for mesh size effects in the simulation of delamination using cohesive zone models. *Engineering Fracture Mechanics* **74,** 1665–1682 (2007).

25.   Song, K., Davila, C. & Rose, C. *Guidelines and parameter selection for the simulation of progressive delamination* in *2008 ABAQUS User's Conference* (2008), 1–15. `http://www.simulia.com/forms/world/pdf2008/SONG-AUC2008.pdf`.

26.   Dassault Systèmes. *Abaqus Analysis User's Manual, Version 6.7* (2007). `http://130.149.89.49:2080/v6.7/books/usb/default.htm`.

27.   Gustafson, P. A. & Waas, A. M. The influence of adhesive constitutive parameters in cohesive zone finite element models of adhesively bonded joints. *International Journal of Solids and Structures* **46,** 2201–2215 (May 2009).

28.   Alfano, G. On the influence of the shape of the interface law on the application of cohesive-zone models. *Composites Science and Technology* **66,** 723–730 (2006).

29.   Benzeggagh, M. L. & Kenane, M. Measurement of mixed-mode delamination fracture toughness of unidirectional glass/epoxy composites with mixed-mode bending apparatus. *Composites Science and Technology* **56,** 439–449 (1996).

30.   Hillerborg, A., Modéer, M. & Petersson, P. E. Analysis of crack formation and crack growth in concrete by means of fracture mechanics and finite elements. *Cement and Concrete Research* **6,** 773–781 (1976).

31.   Pascoe, J. A. *Characterisation of Fatigue Crack Growth in Adhesive Bonds.* PhD thesis (Delft University of Technology, 2016), 147. `http://doi.org/10.4233/uuid:ebbf552a-ce98-4ab6-b9cc-0b939e12ba8b`.

32. Zavatta, N. *Influence of adhesive thickness on adhesively bonded joints under fatigue loading* Master thesis (Università di Bologna, 2015). `http://amslaurea.unibo.it/9713/1/zavatta%7B%5C_%7Dnicola%7B%5C_%7Dtesi.pdf.pdf`.

33. Pascoe, J. A., Al Amery, A. M. K. H. & Zavatta, N. *Effect of Bondline Thickness on Fatigue Crack Growth in FM94.* Dataset. 2016. `http://dx.doi.org/10.4121/uuid:1495c951-33e2-43ab-9f41-5ed3b57ba02f`.

34. Zavatta, N. & Troiani, E. in *ICAF 2019 - Structural Integrity in the Age of Additive Manufacturing* 360–371 (2020).

35. Budzik, M. K., Jumel, J., Ben Salem, N. & Shanahan, M. E. Instrumented end notched flexure - Crack propagation and process zone monitoring Part II: Data reduction and experimental. *International Journal of Solids and Structures* **50,** 310–319 (2013).

36. Budzik, M. K., Jumel, J. & Shanahan, M. E. On the crack front curvature in bonded joints. *Theoretical and Applied Fracture Mechanics* **59,** 8–20 (2012).

37. Chaboche, J. L., Feyel, F. & Monerie, Y. Interface debonding models: A viscous regularization with a limited rate dependency. *International Journal of Solids and Structures* **38,** 3127–3160 (2001).

38. Yu, H. *et al.* Viscous regularization for cohesive zone modeling under constant displacement: An application to hydrogen embrittlement simulation. *Engineering Fracture Mechanics* **166,** 23–42 (2016).

Chapter 4

Influence of a bolted disbond arrest feature on fatigue crack growth in GLARE bonded joints

This chapter investigates the effect of a bolted disbond arrest feature on fatigue crack growth in a GLARE bonded joint. In particular, a modified version of the Cracked Lap Shear (CLS) specimen is used, with an Hi-lok installed in the middle which acts as a disbond arrest feature.

First the relevance of disbond arrest features to certification of adhesively bonded joints is introduced, followed by a concise literature review on the subject of disbond arrest in GLARE. The experimental tests and the numerical model used in this research are then presented. Finally, their results are illustrated and discussed with reference to each other and to existing works in the literature.

This piece of research was conducted in the laboratories of TU Delft. The author would like to thank Prof. Calvin D. Rans of TU Delft, who made this activity possible and provided invaluable suggestions in supervising the work. No blame should be placed on him for any of the opinions expressed in the following by the author.

4.1 Introduction

Certification is one of the major concerns for the application of adhesively bonded joints in aerospace structures. For an adhesive joint, cracking along the bond line, also referred to as disbonding, is probably the most critical fracture mode, as it dramatically impairs the joint's capability to sustain the design loads. In general, disbonding can either result from bad manufac-

turing or from operative loads, and must be taken in due consideration in the design of a damage tolerant structure. For instance, Federal Aviation Administration's Advisory Circular 20-107B [1], §23.573(a)(5), states:

"For any bonded joint, the failure of which would result in catastrophic loss of the airplane, the limit load capacity must be substantiated by one of the following methods:

(i) *The maximum disbonds of each bonded joint consistent with the capability to withstand the loads in paragraph (a)(3) of this section must be determined by analysis, tests, or both.*[1] *Disbonds of each bonded joint greater than this must be prevented by design features; or*

(ii) *Proof testing must be conducted on each production article that will apply the critical limit design load to each critical bonded joint; or*

(iii) *Repeatable and reliable non-destructive inspection techniques must be established that ensure the strength of each joint."*

At present, available non-destructive inspection techniques are not able to fulfil requirement (iii). On the other hand, the application of requirement (ii) is unpractical for aerospace companies for obvious economical reasons, which leaves requirement (i) to be the only viable option for the certification of bonded joints in aerospace structures.

In this context, Disbond Arrest Features (DAF) are an attracting option to improve the fracture behaviour of adhesively bonded joints. The term disbond arrest feature denotes any design feature which can be used to retard or stop the crack growth. For adhesively bonded joints this usually means stopping the crack growth in the adhesive layer, i.e. disbonding. The European project Boltless Assembling of Primary Aerospace Composite Structures (BOPACS) started in 2012 and has demonstrated the capability of bolts to arrest fatigue disbond growth in bonded Carbon Fibre Reinforced Polymers (CFRP) joints [2, 3]. That bolts are able to stop disbond growth in bonded CFRP was also concluded in a joint research project sponsored by the Federal Aviation Administration [4], even though this work dealt mostly with quasi-static loading.

Some studies have been conducted to extend the results found for bonded CFRP joints to fibre metal laminates such as Glass Reinforced Aluminium (GLARE), [3, 5, 6] but they evidenced more difficulties than in CFRP. In particular, fatigue crack arrest was not fully attained in GLARE, which has been suggested by Hangx [5] to be possibly related to fatigue cracking in the adherents.

---

[1]These are basically critical limit flight loads and pressurization loads.

In the following we will investigate fatigue crack growth in bonded GLARE specimens with a bolted disbond arrest feature. To this end, cracked lap shear specimens were modified by installing an Hi-lok in the centre, and tested under fatigue loading. The CLS configuration was chosen because it allows to obtain a realistic mode-mixity ratio, which is comparable to that observed in many aeronautical components. Beside flat-headed Hi-loks similar to those used in earlier works [5, 6], flush-headed ones were also employed, with the aim of investigating their disbond arresting behaviour. A 3D finite element model of the bolted CLS specimen was developed to compute the strain energy release rate around the Hi-lok.

4.2 Literature review

Several studies on the effect of disbond arrest features on fatigue crack growth in bonded joints are available in the literature.

Most of these works deal with bonded composite joints, such as bonded CFRP. Within the European project BOPACS, Kruse et al. [2] investigated the disbond arresting behaviour of a lockbolt in cracked lap shear specimens made of quasi-isotropic CFRP laminates. They found a significant decrease of the crack growth rate behind the bolt's position. The authors also proposed to use a knitted fabric on the adherent's surface so that the fibres could contribute to crack arrest, similarly to what has been reported for Z-pins [7].

Lin et al. [4] and Richard [8] studied the effect of single and double fasteners in bonded CFRP. Crack arrest was observed in both quasi-static and fatigue loading. However, under high fatigue loads Richard found a significant amount of adherent damage close to the hole, which resulted in diminished crack arrest. By using a 3D finite element model, the authors found that the fastener affects the strain energy release rate distribution in a substantial way. [4, 8, 9] Specifically, the clamping force provided by the fastener was reported to produce suppression of the mode I strain energy release rate underneath the fastener head.

Hangx [5] investigated the applicability of a bolted disbond arrest feature in GLARE bonded joints by fatigue testing of wide single lap shear specimens. Flat-headed Hi-loks were used as disbond arrest features. The author reported a fatigue life for the bolted specimens of more than 8 times that of the unbolted one. Unfortunately, only one specimen was tested in the bolted configuration, greatly limiting the statistical significance of the results. Cracking was found in the aluminium plies, which was thought to be coupled with the crack growth in the adhesive.

The effect of a DAF on fatigue crack growth in bonded GLARE was
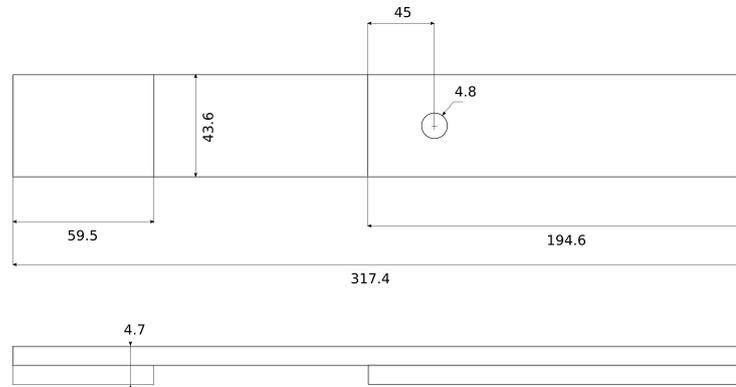
Figure 4.1: Geometry of the cracked-lap shear specimens.

further investigated by van Teeseling [6]. Cracked lap shear specimens were tested in this work, with flat-headed Hi-loks similar to those employed by Hangx. Two different adhesives were tested: a high-toughness and a low-toughness one. A favourable crack arresting effect of the bolt was observed for both specimens, even though it was much more relevant in the low-toughness specimen. In fact, a considerable amount of adherent cracking occurred in the specimens with the tougher adhesive, which forced the author to stop the tests. Strain energy release rate computations using a 2D finite element model evidenced a decrease of the mode I SERR and an increase of the mode II SERR near the disbond arrest feature.

4.3   Materials

In this research cracked lap shear specimens consisting of two fibre metal laminate arms bonded with epoxy adhesive were used. The CLS specimens were modified with the addition of a titanium Hi-lok along the midline, which was used as a disbond arrest feature. The specimens used in this work belong to the same batch of a previous work by van Teeseling [6].

The specimen geometry is shown in Figure 4.1. The length of the specimens is slightly higher than that used for the cracked lap shear specimens used in BOPACS.

The adherents were made of GLARE 2A-4/3-0.4 with Al 2024-T3 metal plies and unidirectional S2-Glass/FM94 prepreg plies. The nominal thickness of the aluminium plies was equal to 0.4 mm. Each fibreglass laminate consisted of two plies of thickness 0.13 mm stacked on top of each other, which gives a nominal thickness of 0.26 mm for the laminate. The plies were

Material	E_{11} [MPa]	E_{12} [MPa]	G_{12} [MPa]	ν_{12}	ν_{21}	σ_Y [MPa]	$\sigma_{4.7\%}$ [MPa]
Al 2024-T3	72400	–	27600	0.33	–	347	420
S2-glass/FM73	48900	5500	5550	0.33	0.0371	–	–

Table 4.1: Material properties of Al 2024-T3 and of the fibreglass prepreg, as taken from Alderliesten [10]. Here $\sigma_{4.7\%}$ denotes the strength at 4.7% strain.

all oriented in the 0° direction, i.e. along the length of the specimen, which results in the highest strength and stiffness in the loading direction. The mechanical properties of Al 2024-T3 and those of the prepreg are shown in Table 4.1. For the adhesive material, an FM94 adhesive film without carrier was used.

A tab was bonded to the longer adherent to obtain the same thickness at both sides of the specimen, as shown in Figure 4.2. This was needed to avoid bending preload when the specimen was mounted on the test machine. The inner edge of the tab was tapered to decrease stress concentrations.

The initial crack was provided by a sawtooth-shaped Teflon foil of length 25 mm inserted between the upper and lower adherents during the bonding process. The sawtooth shape should result in more uniform disbonding compared to a straight insert, thus giving an initial crack front as uniform as possible.

After curing, an hole with a 4.8 mm diameter was drilled in each specimen to accommodate the Hi-lok. The mounting resulted in a tight fit between the Hi-lok and the hole, so to prevent fretting during subsequent testing. The Hi-loks were produced by Lisi Aerospace and made of Ti-6Al-4V titanium alloy. Two different types of Hi-loks were used: flat-headed and flush-headed. A view of the installed Hi-loks is given in Figure 4.3. In all samples, the hole was placed at a distance of 45 mm from the inner edge of the short adherent. According to previous tests [6], this should provide enough room for the crack to grow before reaching the Hi-lok. In the following, we will refer to the samples with the flat-headed Hi-lok as 'HL'; the samples with the flush-headed Hi-lok will be denoted as 'FHL'. A progressive number is used to denote different specimens of the same type; so, for instance, specimen FHL-02 will be the second sample among those with a flush head Hi-lok.

One of the functions of the Hi-lok as a disbond arrest feature is to clamp together the upper and bottom adherents, which is related to the pre-tensioning force in the body of the Hi-lok. This was computed according
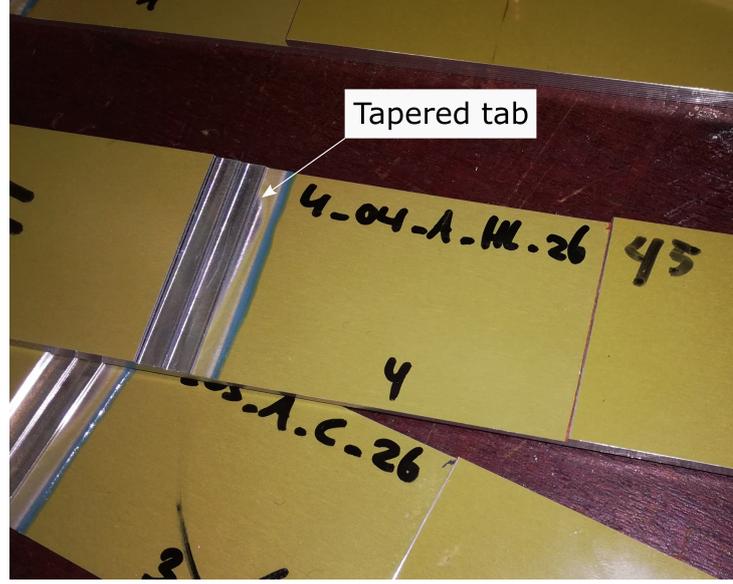
Figure 4.2: Tab bonded on the longer adherent to avoid bending preload during the tests. Note the tapered edge to decrease stress concentrations.

to the following formula [11]:

$$F_{\text{bolt}} = \Delta L_{\text{bolt}} \left(\frac{L_{\text{s}}}{EA_{\text{S}}} + \frac{L_{\text{t}}}{EA_{\text{T}}} \right)^{-1} \tag{4.1}$$

Here E is the elastic modulus of the Hi-lok's shaft, ΔL_{bolt} is the total variation of length due to pre-tensioning, A_{S} and A_{T} are the cross-sectional areas of the unthreaded and threaded parts of the shaft and L_{s}, L_{t} are defined as:

$$L_{\text{s}} = L_{\text{S}} + \frac{T_{\text{H}}}{2} \tag{4.2}$$

$$L_{\text{t}} = L_{\text{T}} + \frac{T_{\text{N}}}{2} \tag{4.3}$$

where L_{S} and L_{T} are the lengths of the unthreaded and threaded sections of the the shaft and T_{H}, T_{N} are the thicknesses of the Hi-lok's head and nut respectively. Knowing the diameter of the shaft, D_{S}, and the thread pitch, p, the cross-sectional areas can be calculated as:

$$A_{\text{S}} = \frac{\pi}{4} D_{\text{S}}{}^{2} \tag{4.4}$$

$$A_{\text{T}} = \frac{\pi}{4} \left(D_{\text{S}} - 0.938p \right)^{2} \tag{4.5}$$

The deformation $\Delta L_{\text{bolt}} = L_1 - L_0$ was computed by measuring the length of the undeformed Hi-lok prior to mounting, L_0, and that after installation, L_1.

(a)

(b)

Figure 4.3: Picture of the Hi-lok's installation: (a) bottom view; (b) top view. The difference between the flush head and the flat head is visible.

Specimen	L_0 [mm]	L_1 [mm]	ΔL_{bolt} [mm]	F_{bolt} [N]
HL-01	14.994	15.021	0.027	2414.7
HL-02	15.023	15.057	0.034	3036.8
FHL-01	14.653	14.702	0.049	4396.7
FHL-02	14.654	14.696	0.042	3768.4
FHL-03	–	–	–	–

Table 4.2: Summary of the pre-tensioning force in the different samples, as computed according to Equation (4.1). For sample FHL-03, the pre-tensioning force could not be computed due to problems in measuring the length.

A micrometer was used for length measurements. The results of the pre-tensioning force measurements are collected in Table 4.2.

4.4   Test set-up

Fatigue tests were performed on a 60 kN fatigue testing machine at a frequency of 5 Hz. All tests were conducted under force control, and force and displacement were measured by the fatigue bench.

The top surface of the samples was painted white and a speckle pattern for DIC measurements was applied on it with a spray paint. Additionally, one side was painted with typewriter corrector fluid and a strip of scale paper was attached on it to allow visual measurement of the crack length. The pattern painted on the top surface is shown in Figure 4.4.

The specimens were mounted on the fatigue machine using clamps, as shown in Figure 4.5.

The crack length was measured using a 9 MP camera aimed at the side of the specimen. Two 5 MP cameras aimed at specimen's top were used to track the surface displacements. The acquisition frequency was such that one picture was taken every 500 cycles. A digital image correlation technique was applied to compute the strain field at the surface. The dedicated software *Vic3D* was employed to calculate the strain from the raw images. The strain data obtained from the software were then used to compute the crack area, as explained in section 4.5. Accurate calibration is required for the DIC measurements. This was performed in the Vic3D software prior to fatigue tests. Basically, some images are taken using a calibration target, i.e. a rigid plate with equispaced marks on it, and they are processed by the software

Figure 4.4: Speckle pattern for DIC measurements on the top surface of two specimens. An HL and an FHL samples are shown. The HL sample is clearly recognizable from the protruding head.

Figure 4.5: Clamps used to connect the specimens to the fatigue machine.
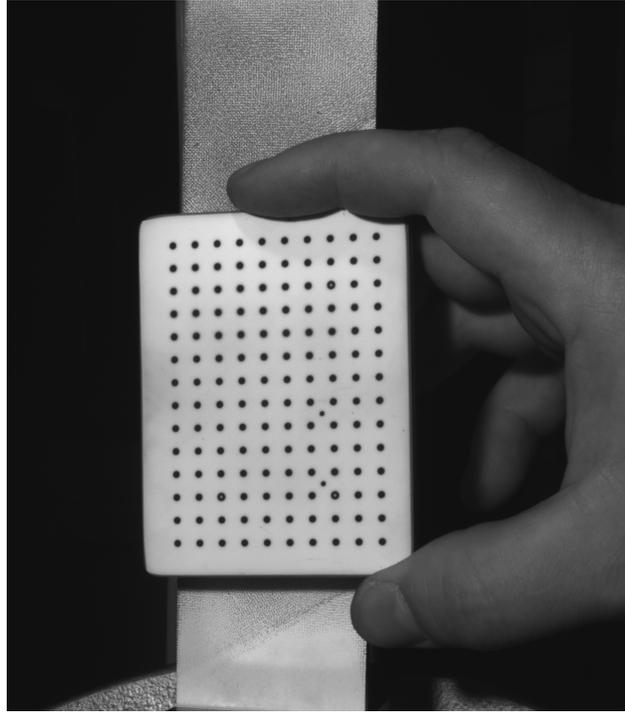
Figure 4.6: Image used for calibration of the DIC measurement system.

to compute the calibration parameters. An example of the images used for the calibration procedure is given in Figure 4.6.

The following load sequence was applied in the fatigue tests. First, an high cyclic load was applied for 10 kcycles to facilitate crack initiation. After that, the load was lowered and this second cyclic load was maintained until the end of the test. The test was stopped when evidence of adherent failure was observed, as discussed later.

In all tests, an R-ratio $R = \frac{P_{min}}{P_{max}} = 0.1$ was used for both the first and the second part of the experiment. The maximum load P_{max} applied in the initiation phase was equal to 28 kN ($P_{min} = 2.8$ kN). The value of the load in the propagation phase was chosen based on previous tests by van Teeseling [6]. In those experiments, a value $P_{max} = 26$ kN had been used, which had resulted in cracking of the top adherent before an acceptable crack growth along the bondline could be observed. The amount of unexpected adherent cracking seen in the first tests had been so severe that the author had resorted to using a second type of specimens with a weaker adhesive for the rest of the experiments. For this reason, we lowered the load applied in the second part of the test to $P_{max} = 24$ kN ($P_{min} = 2.4$ kN), in an attempt to retard adherent cracking. It should be noted that decreasing the applied
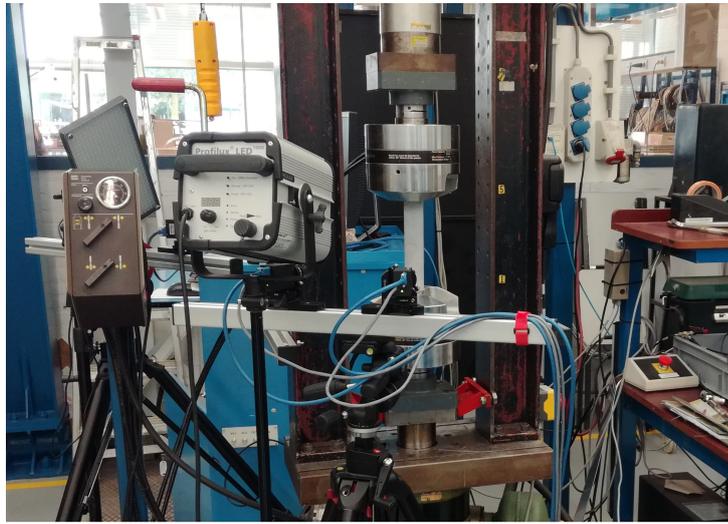
Figure 4.7: Experimental set-up used in the fatigue tests. The two 5 MP cameras used for DIC images acquisition are recognizable in the front. Barely visible behind the lamp is the 9 MP side camera.

load also slows the crack growth in the adhesive layer, which could result in the same problem encountered by van Teeseling. Given the complex relation between crack growth in the bondline and adherent cracking, no estimate of the optimal load value could be made before testing. Information on the load cycles applied for each experiment is given in the test matrix in Table 4.3.

A view of the complete experimental set-up is given in Figure 4.7.

4.5 Methods

In this section the methods used to measure the fatigue crack growth in the experimental tests are presented. An existing theoretical model for computing the strain energy release rate in a crack lap shear specimen is then illustrated, together with a method for fatigue crack growth prediction under mixed-mode conditions.

4.5.1 Fatigue crack growth measurement

The crack length at the side of the specimen was measured visually from the pictures taken by the side camera. The camera was triggered automatically while the maximum load was applied, in order to have a clear view of the open crack tip. Even though the system acquired one image every 500 cycles, the

Type	Sample	$P_{\max, i}$ [N]	N_i [cycles]	$P_{\max, g}$ [N]	N_g [cycles]
Flat head	HL-01	28000	10000	24000	165499
	HL-02	28000	10000	24000	131999
Flush head	FHL-01	28000	10000	24000	149999
	FHL-02	28000	10000	24000	176499
	FHL-03	28000	10000	24000	175999

Table 4.3: Test matrix of all samples, grouped according to the type of Hi-lok. Here, $P_{\max, i}$ and N_i denote the maximum load applied in the initiation phase and the corresponding number of cycles respectively; $P_{\max, g}$ and N_g denote the maximum load applied during crack growth and the corresponding number of cycles.

crack length was measured only once every 3500 cycles, as the crack growth could not be detected from the intermediate pictures.

The images taken by the two front cameras were used to compute the surface displacements and thus the strain field by means of digital image correlation. As DIC is a well-established measurement technique in the literature and all the computation involved were performed by the commercial software Vic3D, we will not deal with the details of it.

The strain data from the DIC were used to track the position of the disbond front, using a method similar to that presented by van Teeseling [6]. This allows to monitor the evolution of the crack area and its shape, more than just relying on unidimensional measurements of the crack length. However, the crack length measurements taken by the side camera were used for comparison with the DIC-based method.

An ad-hoc algorithm was developed to compute the crack front position. The following steps are executed:

- Data from the DIC measurements are initialized. This results in a map such as that in Figure 4.8a. Inaccurate measurements are usually taken in regions with poor speckle pattern and close to the edges.

- Raw DIC data are cleaned to remove incorrect data points. Moreover, data in and around the Hi-lok head are removed from the map (see Figure 4.8b), as the discontinuity of the strain field at the interface between the Hi-lok and the surrounding material produces an artificial strain gradient that affects the adjacent data in the subsequent step. We note that the data belonging to the Hi-lok are not needed to track the crack front, thus this process involves no loss of information.

Sample	α	β	γ	RMSE
HL-01	$4.56 \cdot 10^{-4}$	1.20	1214	17.9
HL-02	$1.96 \cdot 10^{-2}$	0.89	1217	16.1
FHL-01	1.09	0.54	1053	28.6
FHL-02	$7.06 \cdot 10^{-2}$	0.76	1191	18.6
FHL-03	$5.36 \cdot 10^{-2}$	0.77	1280	19.1

Table 4.4: Coefficients of Equations (4.6) and (4.7). The crack area A_b is in [mm^2]. The root mean square error $RMSE$ is also reported.

- The strain field, which is computed by the DIC in a pixel-based frame of reference, is projected onto a uniform grid. This provides a uniform distribution of data points, such as that shown in Figure 4.8c. The removal of points in the Hi-lok region performed during previous step ensures that the projection is not affected by those data points.

- The position of the crack front is computed as follows. Let suppose the rectangular grid has size $m \times n$; the strain field ε_y is sliced in m subsets $\varepsilon_i = \{\varepsilon(x_i, y_j) \quad \forall j \in \{1, \ldots, n\}\}$ and the minimum value $\varepsilon(x_i, y_{m_i})$ of each subset is calculated. The crack front is found as the set of points $\{(x_i, y_{m_i}) \quad \forall i \in \{1, \ldots, m\}\}$. Basically, we assume that the crack front corresponds to the points of minimum strain in the loading direction.

The crack area A_b is uniquely defined once the crack front is computed, if we assume that the region before the crack front is fully disbonded. An example of the algorithm's output is given in Figure 4.9. The method described above proved able to track the crack front position with reasonable accuracy, as seen from the comparison with the crack length measured at the side, provided that no cracking occurs in the adherent. If a crack propagates through the GLARE adherent, it substantially affects the surface strain field, to the point that the results computed by the algorithm above are inconsistent.

The crack area growth rate, $\frac{\mathrm{d}A_b}{\mathrm{d}N}$, was computed as follows. First we fitted a curve through the A_b vs N data, according to the following expression:

$$A_b = \alpha N^\beta + \gamma \tag{4.6}$$

Then, the crack area growth rate was calculated by differentiating Equation (4.6), which gives:

$$A_b = \alpha \beta N^{\beta - 1} \tag{4.7}$$

The values of coefficients α, β and γ are reported in Table 4.4.
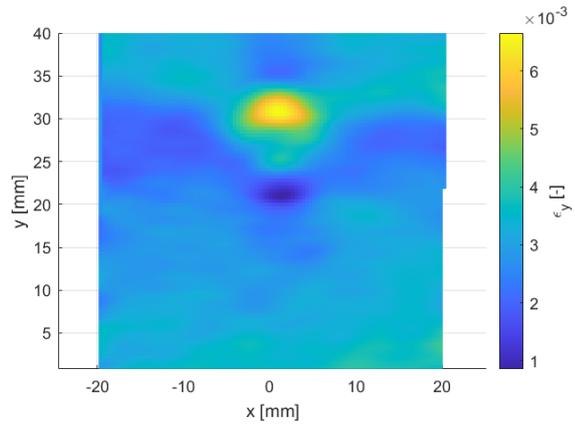
(a)
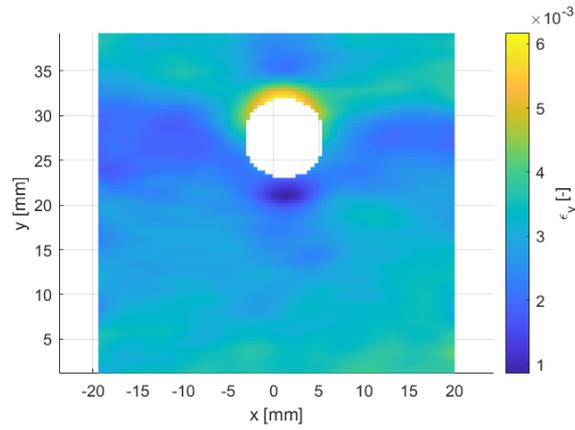
(b)
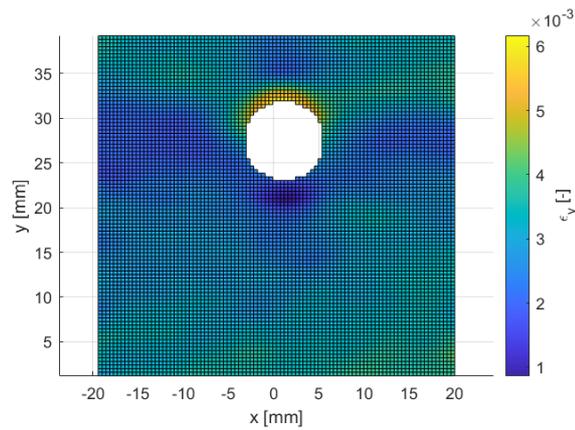
(c)

Figure 4.8: Steps of the algorithm for crack area measurement: (a) DIC data initialization, (b) removal of Hi-lok data, (c) data projection on grid.
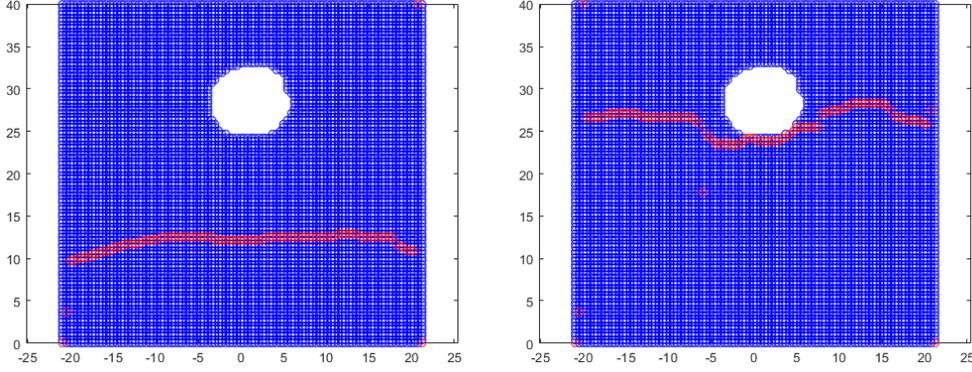
Figure 4.9: Crack front as computed by the tracking algorithm. The front positions for 10 kcycles (left) and 100 kcycles (right) are shown.

4.5.2 Strain energy release rate in a CLS specimen

To the author's knowledge, no analytical expression exists for computing the strain energy release rate in bolted cracked lap shear specimens. However, given the complex 3D stress state around the Hi-lok, it seems unlikely that such an expression for the SERR could be derived in simple terms. In this work, the bolted specimens were modelled with a 3D finite element method and the Virtual Crack Closure Technique (VCCT) was used to compute the strain energy release rate at the crack front, as discussed in section 4.6.

An expression to compute the total strain energy release rate in a conventional cracked lap shear specimen, i.e. without the Hi-lok, was derived by Brussat et al. [12, 13], which can be used as a comparison for the results of the numerical model. This formulation was obtained under the assumption of infinitely long specimen, and results in a constant value of the total SERR, which is given by:

$$G_{\mathrm{T}} = \frac{P^2}{2w(EA)_{\mathrm{s}}} \left[1 - \frac{(EA)_{\mathrm{s}}}{(EA)_0} \right] \tag{4.8}$$

where P is the applied load, w is the width of the specimen and $(EA)_{\mathrm{s}}$, $(EA)_0$ are the tensile rigidity of the strap section and that of the whole specimen, i.e. strap+lap sections, respectively. Moreover, Brussat et al. also derived the following expression for the mode I component of the strain energy release rate:

$$G_{\mathrm{I}} = \frac{2M_0^2}{7w(EI)_{\mathrm{s}}} \left[1 - \frac{(EI)_{\mathrm{s}}}{(EI)_0} \right] \tag{4.9}$$

Here, M_0 is the internal bending moment at the crack tip, which can be

computed as:

$$M_0 = \frac{(y_{\mathrm{s}} - y_0)\, P}{1 + \sqrt{(EI)_0/(EI)_{\mathrm{s}}}} \tag{4.10}$$

being y_{s}, $(EI)_{\mathrm{s}}$ and y_0, $(EI)_0$ the centroid locations and bending rigidities of the strap section and of the whole specimen respectively.

In the case of equal adherents of thickness t, Equations (4.8) and (4.9) become:

$$G_{\mathrm{T}} = \frac{P^2}{4w(EA)_{\mathrm{s}}} \tag{4.11}$$

$$G_{\mathrm{I}} = \frac{M_0^2}{4w(EI)_{\mathrm{s}}} \tag{4.12}$$

with $M_0 = \frac{tP}{2(1+\sqrt{8})}$. By knowing G_{T} and G_{I}, the mode II component of the strain energy release rate can be computed simply as:

$$G_{\mathrm{II}} = G_{\mathrm{T}} - G_{\mathrm{I}} \tag{4.13}$$

4.5.3 Fatigue crack growth prediction in mixed-mode

A method to compute the fatigue crack growth in adhesively bonded joints under mixed-mode conditions was proposed by Bürger [14]. He suggested that fatigue crack growth be related to the principal stresses at the crack tip and derived an expression for an equivalent mode I strain energy release rate $G_{1,\,\mathrm{eq}}$ based on the principal stresses. A modification of Paris' relationship was then proposed using this energy as the scaling parameter.

According to Bürger's model, the equivalent mode I strain energy release rate can be computed as:

$$\sqrt{G_{1,\,\mathrm{eq}}} = \frac{\sqrt{G_{\mathrm{I}}}}{2} + \sqrt{\frac{G_{\mathrm{I}}}{4} + G_{\mathrm{II}}} \tag{4.14}$$

where G_{I} and G_{II} are respectively the mode I and mode II components of the SERR as usually defined. Considering the maximum an minimum values in a fatigue cycle, $G_{\mathrm{I,\,max}}$, $G_{\mathrm{II,\,max}}$ and $G_{\mathrm{I,\,min}}$, $G_{\mathrm{II,\,min}}$ respectively, the corresponding values $\sqrt{G_{1,\,\mathrm{eq,\,max}}}$ and $\sqrt{G_{1,\,\mathrm{eq,\,min}}}$ can be computed. The scaling parameter of Paris' law is now defined as:

$$\Delta\sqrt{G_{1,\,\mathrm{eq}}} = \left(\sqrt{G_{1,\,\mathrm{eq,\,max}}} - \sqrt{G_{1,\,\mathrm{eq,\,min}}}\right)^2 \tag{4.15}$$

The modified Paris' relationship thus reads:

$$\frac{\mathrm{d}a}{\mathrm{d}N} = C \left(\Delta\sqrt{G_{1,\,\mathrm{eq}}}\right)^n \tag{4.16}$$

Material	$C_{0\%}$	$C_{100\%}$	$n_{0\%}$
FM94	$5.27 \cdot 10^{-17}$	$2.07 \cdot 10^{-18}$	3.78

Table 4.5: Coefficients of modified Paris' law, as expressed in Equations (4.16) and (4.17). Strain energy release rate in [J/m^2] and crack growth rate in [m/cycle].

where coefficients C and n must be determined by fitting through experimental data. In general, these coefficients depend on the mode-mixity ratio. In Bürger's work it is proposed to consider n constant as the mode-mixity ratio varies and to compute C accordingly. Thus, defining the mode-mixity ratio $m = \frac{G_{\text{II}}}{G_{\text{I}}+G_{\text{II}}}$ and denoting by $n_{0\%}$ the coefficient n computed for pure mode I, the coefficient C can be calculated according to:

$$C\left(m\right) = C_{100\%}^{m} \cdot C_{0\%}^{1-m} \tag{4.17}$$

being $C_{0\%}$ and $C_{100\%}$ the coefficients computed for pure mode I and pure mode II respectively. The coefficients for FM94 adhesive film were provided by Bürger [14] and van Teeseling [6], and are collected in Table 4.5.

4.6   Numerical model

In order to compute the strain energy release rate in the CLS specimen with the Hi-lok, a 3D finite element model was developed in Abaqus. The geometry of the model followed that of the tested samples, i.e. a cracked lap shear specimen with same dimensions. The bolt was modelled as a deformable body with the same geometry of the flat-headed Hi-lok. Pre-tensioning was applied to the bolt, according to the values in Table 4.2.

The GLARE adherents were modelled as an orthotropic laminate with elastic behaviour, using the properties reported in Table 4.1. The adhesive layer and the Hi-lok were considered as isotropic materials with elastic properties.

The adherents and the Hi-lok were meshed with first-order hexahedral elements with reduced integration, i.e. type C3D8R. For the adhesive layer, incompatible-mode hexahedral elements of type C3D8I were used, which are well suited to model bending. Where the hexahedral elements could not be used, wedge elements of type C3D6 were employed. The mesh was refined around the crack front and at the sides of the hole; this resulted in a minimum element size of about 0.05 mm.
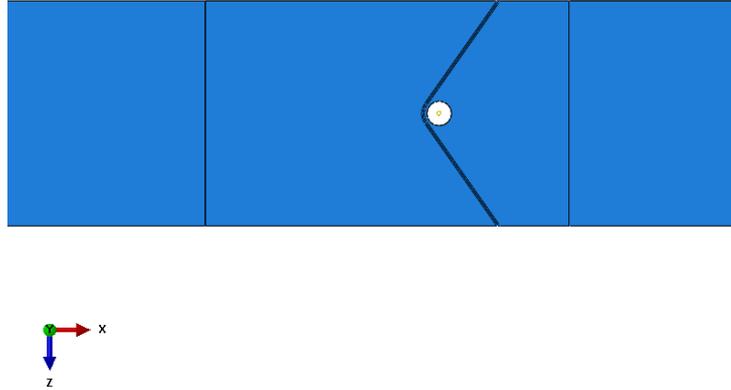
Figure 4.10: Curved crack front at a distance of 0.75 mm from the edge of the hole. The Hi-lok is not shown in order not to obstruct the view.

The strain energy release rate was computed using the virtual crack closure technique [15, 16]. This allowed for direct calculation of the three SERR components, i.e. modes I, II and III, along the crack front. Previous experiments evidenced that the shape of the crack front changes in proximity of the Hi-lok [6], as the crack wraps around the hole, which can also be seen in Figure 4.9. Accordingly, a curved crack front was used for the VCCT. The shape of the crack front was taken from van Teeseling's measurements, and approximated by two oblique segments connected by an arc in front of the hole, as shown in Figure 4.10. Three different locations of the crack front were considered, respectively at a distance of 2.3 mm, 1.3 mm and 0.75 mm from the edge of the hole. The angle of the oblique segments was maximum in the 0.75 mm position and decreased far from the hole, so that the crack front was straight at the 2.3 mm position.

A load of 26 kN was applied in the simulations, in order to compare the results to an earlier 2D model by van Teeseling [6]. A conventional cracked lap shear specimen without the Hi-lok was also modelled, for comparison with the theoretical model of Brussat et al. [12]. For all the characteristics of this second model, one could refer to those of the bolted one, the only difference being the absence of the hole.
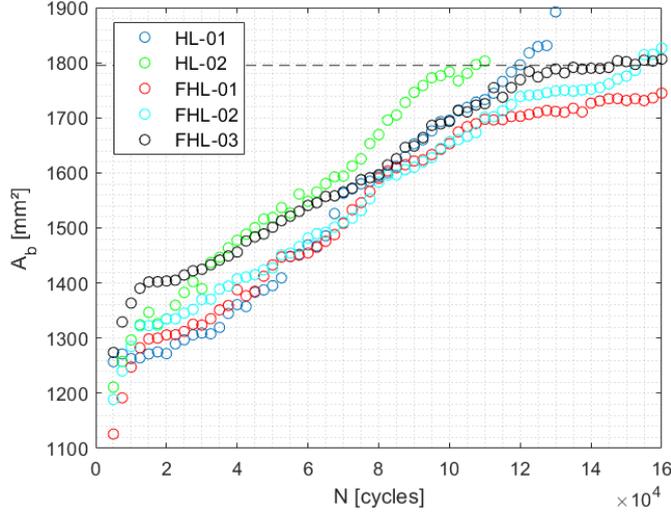
Figure 4.11: Crack area computed from the DIC data, plotted as a function of the number of cycles. The results for both types of specimens are shown. The dashed line represents the area corresponding to the edge of the flush-headed Hi-lok.

4.7 Results

In this section, the results of the fatigue tests and those obtained with the numerical model are presented. The experimental and numerical results will then be discussed in section 4.8 in relation to each other and compared to existing works in the literature.

4.7.1 Experimental results

Figure 4.11 shows the crack area A_b measured in the fatigue tests with the DIC-based algorithm, plotted as a function of the number of cycles N. Both HL and FHL specimens are shown. The crack area grows rapidly in the first 10 kcycles, which can be related to insert pre-cracking. Past this point, all specimens show an approximately linear increase of the crack area for about 100 kcycles. This linear growth should be expected if one assumes that the crack growth rate depends on $\Delta\sqrt{G_{1,\,\mathrm{eq}}}$, because the strain energy release rate is constant through the length of a cracked lap shear specimen. A clear decrease of the crack area growth is visible in all FHL specimens close to the head of the Hi-lok, which seems most likely related to the effect of the disbond arrest feature. Specimen HL-01 is an exception, as the crack continues to grow beyond the Hi-lok. The crack area growth beyond the
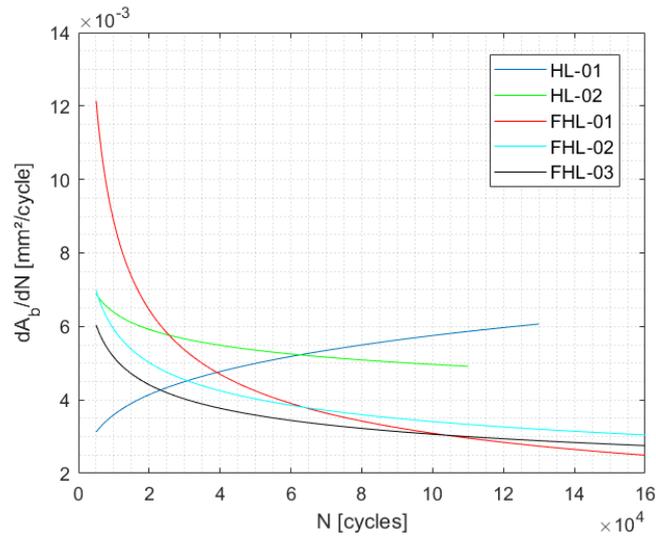
Figure 4.12: Crack area growth rate plotted against the number of cycles.

head of the Hi-lok could not be measured in the HL samples, because the DIC data were too noisy.

That the crack growth decreases past a given point can also be seen in Figure 4.12, which shows the crack area growth rate $\frac{\mathrm{d}A_b}{\mathrm{d}N}$ computed according to Equation (4.7) as a function of the number of cycles. Clearly, the crack growth rate decreases as the crack approaches the Hi-lok. The only exception is specimen HL-01, as already observed in Figure 4.11. It should be noted that, since the curve chosen to fit the data in Equation (4.6) is not upperly bounded, complete crack arrest can not be predicted.

The crack growth data discussed earlier are shown again in Figure 4.13, this time together with data obtained by the side camera. The crack area measured by the DIC-based algorithm is divided by the specimen width, so that an equivalent crack length is computed, equal to that which would give the same cracked area if the crack front were straight. It can be seen clearly that the DIC-based measurements and those by the side camera are almost equal up to approximately 100 kcycles, while a higher crack length is measured by the side camera beyond this point.

This provides a validation of the algorithm based on the DIC data. In fact, since the crack front is almost straight far from the Hi-lok, as shown in Figure 4.9, the crack length measured at the sides should be equal to the crack area divided by specimen thickness, i.e. the equivalent crack length shown on the graph for the DIC-based algorithm.

By comparing Figure 4.13 to Figure 4.11 it can be observed that the
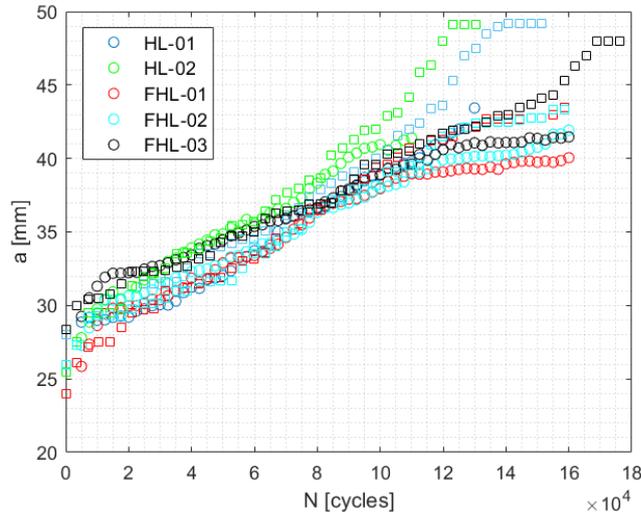
Figure 4.13: Crack length measured by the side camera (squares), plotted together with the equivalent crack length obtained dividing the crack area by specimen thickness (dots).

crack length measured by the camera gets higher that the one based on the DIC when crack growth approaches the Hi-lok position. This means that in this region the crack grows faster near the specimen edges than it does in the centre. Therefore, care must be taken when drawing conclusions on the inner crack shape, if only side measurements are available.

In all specimens, adherent cracking was observed after the crack reached the Hi-lok position. From our observations, the crack growth along the edges of the specimen stopped, while damage in the adherent started. For instance, let us consider specimen HL-01, for which crack growth at the edges stops at approximately 140 kcycles, as visible in Figure 4.13. Figure 4.14, taken at 145 kcycles, shows evidence of surface cracking in the aluminium panel started at the edge of the hole. We might argue that surface adherent cracking could have been preceded by some other form of damage, such as disbonding of the pre-preg plies, which would explain why, starting from approximately 13 kcycles, the noise observed in the DIC measurements on this specimen became so high that the crack area could not be computed.

4.7.2 Numerical results

Figure 4.15 shows the mode I and mode II components of the strain energy release rate computed by the model for the conventional cracked lap shear
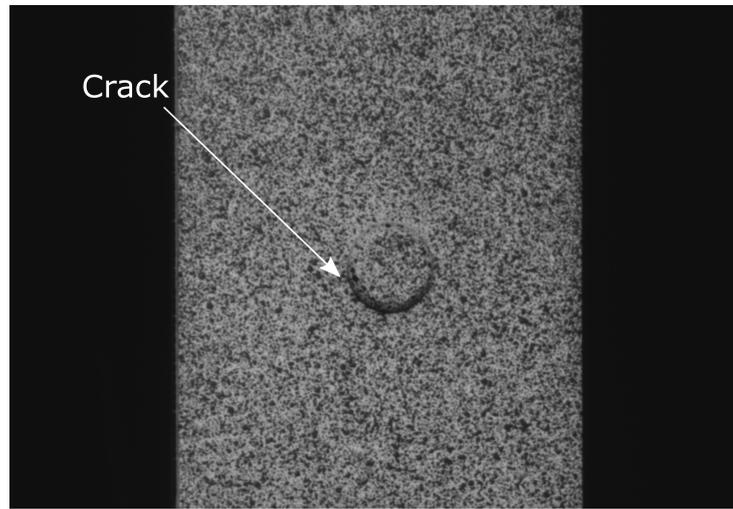
Figure 4.14: Surface crack started at the edge of the hole in the aluminium panel. The picture was taken at 145 kcycles.

specimen without the Hi-lok. The mean value of the SERR is obtained by averaging along the crack front. Also shown is the SERR computed according to Brussat et al.'s model, i.e. Equations (4.11), (4.12) and (4.13). The G_{II} computed by the VCCT is close to that predicted by the theory, with a difference of less than 4%. On the other hand, the G_{I} computed using Brussat's model is about 17% less than the numerical results.

The strain energy release rate distribution along the width of the modified cracked lap shear specimen is shown in Figure 4.16, for different positions with respect to the Hi-lok. Distances of 2.3 mm, 1.3 mm and 0.75 mm from the edge of the hole are shown. The edge of the Hi-lok's head is 2.2 mm away from the edge of the hole, which means that the 1.3 mm and 0.75 mm locations are right under the head, while the 2.3 mm one is slightly in front of it. A substantial effect of the bolt on the strain energy release rate is visible for all fracture modes. The mode I SERR decreases significantly close to the bolt, as crack opening is constrained by the clamping force exerted by the Hi-lok. In fact, the mode I suppression by the disbond arrest feature is maximum in the region under the head of the Hi-lok, i.e. the one delimited by the dashed lines in the figure. On the other hand, the mode II and mode III components increase close to the Hi-lok, which might be a result of the higher shear stress resulting from the bolt-hole combination.

It is worth noting that, outside the region of influence of the Hi-lok, the disbond arrest feature seems to be detrimental in terms of crack growth. In fact, comparing Figure 4.16 to Figure 4.15 clearly shows that G_{I} and G_{II}
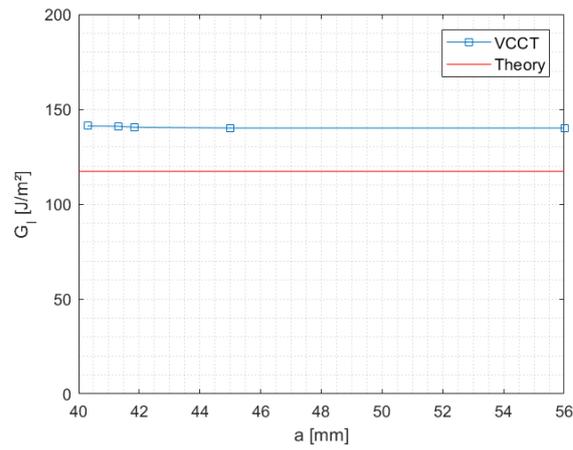
(a) Mode I
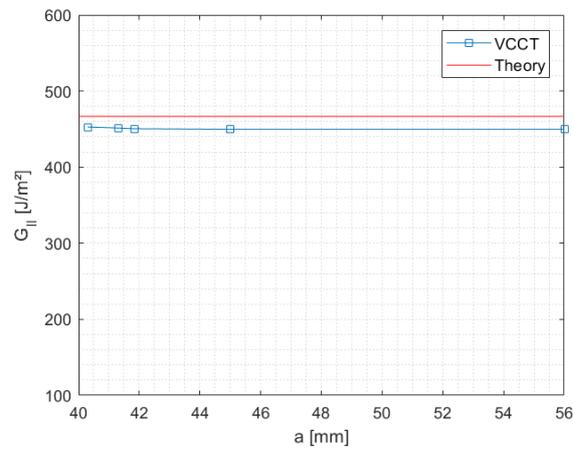
(b) Mode II

Figure 4.15: Comparison of the average strain energy release rate computed by the VCCT and according to Brussat et al.'s theory, in the case of a cracked lap shear specimen without the Hi-lok. The mode I and mode II components of the SERR are shown.
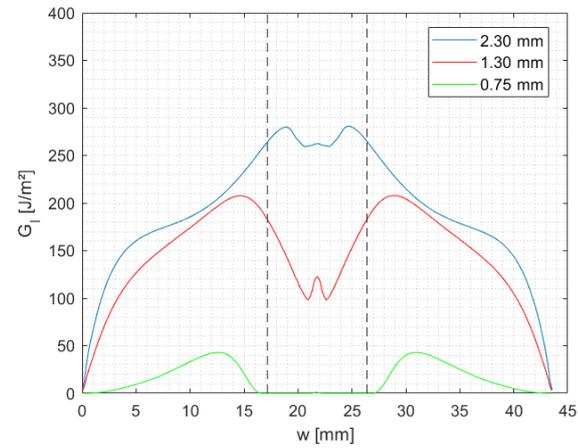
(a) Mode I
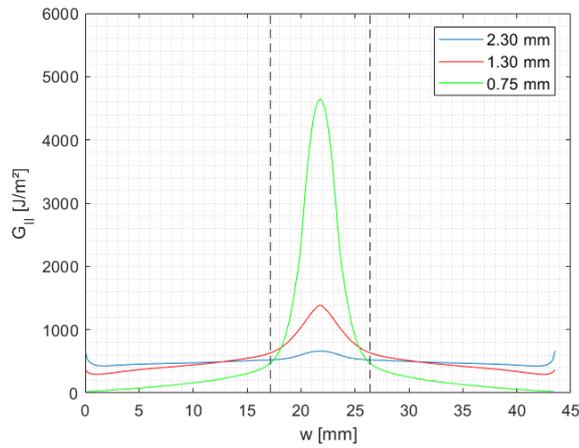
(b) Mode II
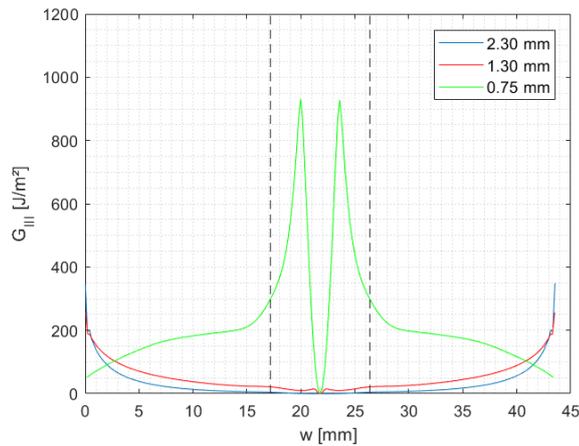
(c) Mode III

Figure 4.16: Distribution of the strain energy release rate along the specimen width. Three distances with respect to the edge of the hole are considered: 2.3 mm, 1.3 mm and 0.75 mm. The vertical dashed lines denote the coordinates corresponding to the edge of the Hi-lok's head.

are higher in front of the bolt compared to a conventional cracked lap shear specimen, which would result in more energy available to drive crack growth.

This can also be seen by considering the average value of the strain energy release rate, as shown in Figure 4.17. As noted previously, the mode I SERR decreases in the region around the Hi-lok, while the mode II component increases. In general, both mode I and mode II components are higher as compared to an unbolted specimen.

Clearly, numerical values as high as $G_{II} = 4500$ J/m^2 computed by the model close to the hole are unrealistic, because the crack will propagate in a quasi-static way when the toughness of the adhesive is exceeded. Nevertheless, these results suggest that there is a steep SERR gradient before and about the bolt, which should be taken into account for both an optimal design of the disbond arrest feature and of the surrounding structure.

4.8 Discussion

A comparison between the results of the numerical model and those computed with Brussat et al.'s formulation, e.g. Figure 4.15, shows that, for a conventional cracked lap shear specimen, both approaches predict similar values of the strain energy release rate. This is especially true for the mode II energy release rate, where the two models differ by about 3%, while the difference is more pronounced for mode I, approximately 17%. According to these results, the $\frac{G_I}{G_{II}}$ computed by the VCCT is equal to 0.31, while Brussat's model gives a value $\frac{G_I}{G_{II}} = 0.25$, with a mutual difference of about 20%. These figures compare fairly well with the results presented in a previous round-robin [13], where several methods applied to compute the SERR of a cracked lap shear specimen produced values of $\frac{G_I}{G_{II}}$ between 0.2 and 0.4, and differences within a range of 30% from one another.

Combining Brussat's model to compute the strain energy release rates G_I and G_{II} with the Paris' law modified by Bürger, we can estimate the fatigue crack growth rate in the cracked lap shear specimens, at least far from the region of influence of the bolt.

Figure 4.18 shows a comparison between the fatigue crack growth measured in the tests and that predicted combining Brussat's and Bürger's models. The values of $G_{I,\,max}$, $G_{II,\,max}$ and $G_{I,\,min}$, $G_{II,\,min}$ are computed according to Equations (4.12) and (4.13). As Brussat's formulation gives a constant value of the SERR along the specimen length, the equivalent SERR range $\Delta\sqrt{G_{1,\,eq}}$ is also constant. This results in a linear growth of the crack which,
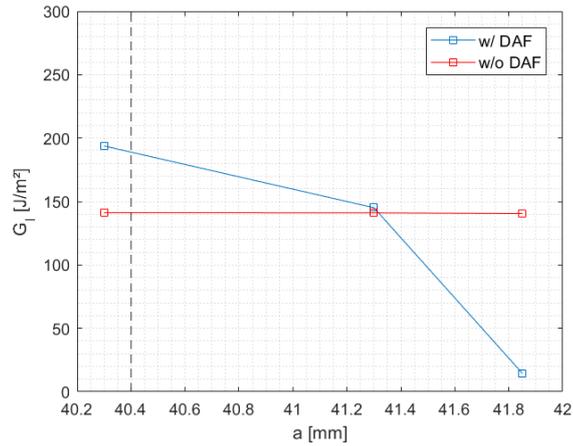
(a) Mode I
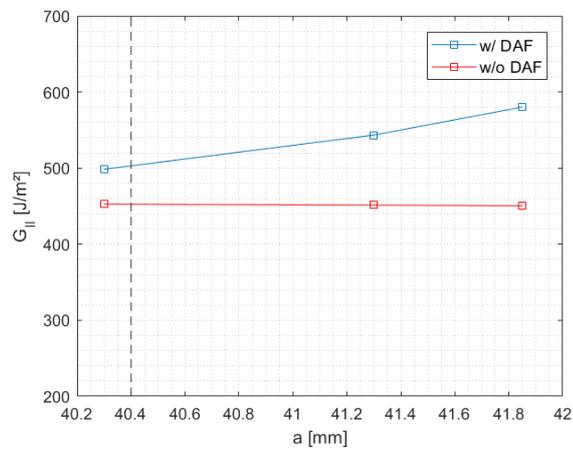
(b) Mode II

Figure 4.17: Comparison of the average strain energy release rate computed for the conventional cracked lap shear specimen and for the bolted one. The vertical dashed line denotes the edge of the Hi-lok's head.
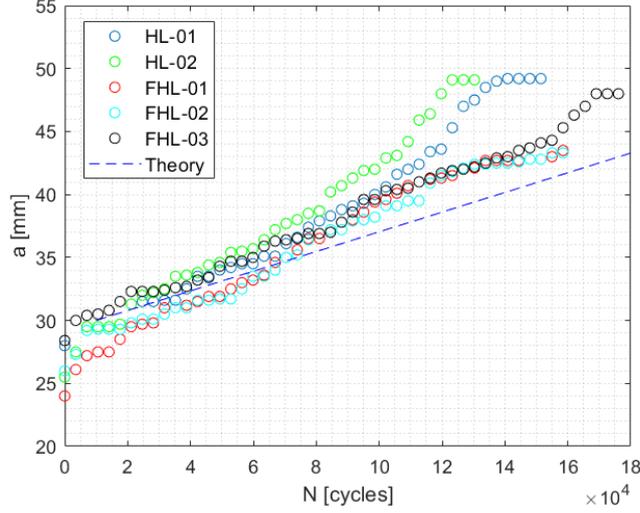
Figure 4.18: Crack length plotted as a function of the number of cycles. The theoretical curve obtained by the combination of Brussat's and Bürger's models is shown for comparison.

by using Equation (4.16), can be expressed as:

$$a = C \left(\Delta \sqrt{G_{1,\,eq}} \right)^n (N - N_0) + a_0 \qquad (4.18)$$

where N_0 and a_0 are the initial number of cycles and the corresponding crack length, respectively. Here, the initial number of cycles was chosen equal to that used for insert pre-cracking, i.e. $N_0 = 10$ kcycles, while a_0 was taken equal to the insert length, i.e. $a_0 = 30$ mm. Coefficients C and n were taken from Table 4.5. The graph shows that the curve predicted by the theoretical model overlaps with the experimental results for the first part of the tests, i.e. far from the Hi-lok, while the crack length increases when it gets close to the region of influence of the bolt. This can be explained by the fact that crack propagation is not arrested near the sides of the specimen, as already noticed in Figure 4.13.

The numerical model allows to compute the distribution of the strain energy release rate in the region of influence of the bolt. As visible in Figures 4.16 and 4.17, there is a steep SERR gradient right under the bolt's head and slightly in front of it. In particular, the mode I component is suppressed around the bolt, while the shearing components, i.e. mode II and III, increase. This is consistent with earlier findings by van Teeseling [6] and Richard et al. [9], obtained using a 2D and a 3D finite element model respectively. As the present 3D model confirms these findings, a deep under-

standing of the crack growth mechanism under prevalent mode II conditions seems crucial to accurately quantify the effect of the bolted disbond arrest feature on fatigue crack growth.

The present experimental results are not directly comparable to those reported by van Teeseling, because they were obtained for different loads, respectively $P_{\max} = 24$ kN and $P_{\max} = 26$ kN. However, the same trend is visible in the data. In van Teeseling's work, the crack area growth rate $\frac{\mathrm{d}A_b}{\mathrm{d}N}$ was found to decrease near the bolt's location, similarly to the behaviour seen in Figure 4.11 for flush-headed Hi-loks. This suggests that flush-headed bolts could be an alternative to flat-headed ones for crack arrest in GLARE.

Moreover, a comparison between HL and FHL specimens in Figures 4.11 and 4.13 shows that adherent cracking, which is related to the arrest of crack growth in the adhesive, occurs earlier for flat-headed Hi-loks than for flush headed-ones. This seems to suggest that not only do flush head bolts produce a retardation of fatigue crack growth in the adhesive, but they also postpone cracking of the adherents. Further research should be envisioned to support this hypothesis. In particular, numerical simulations considering a flush-headed bolt could give an insight on the SERR distribution around the Hi-lok. This could also be used to design an optimal shape for retarding fatigue crack growth.

Although lower loads were used in this research as compared to those applied in a similar work by van Teeseling [6], in which the same type of specimens was used, fatigue cracking of the GLARE adherents could not be prevented, which hindered the observation of crack arrest in the adhesive. This is critical, as the crack growing in the adherent affects the disbond, thus making it difficult to assess the effect of the Hi-lok on the disbonding mechanism. Even though the exact relationship between adhesive cracking and adherent cracking in a bolted cracked lap shear specimen is unknown, solutions must be found to postpone adherent cracking, so that the crack arrest in the adhesive provided by the bolt could be better quantified. For further tests on high-toughness adhesives such as FM94 we suggest to use specimens with either increased width or increased thickness. Among these two options, increasing the width seems the best one, as changing the thickness would affect the mode-mixity ratio in the specimen.

4.9   Conclusions

The effect of a disbond arrest feature on fatigue crack growth in bonded GLARE specimens was investigated by a combination of experiments and numerical calculations.

For the specimens tested in this research, the fatigue crack growth was moderately decreased by the bolt; unfortunately, because the decrease of crack growth in the adhesive is accompanied by cracking of the aluminium plies, it could not be assessed whether full disbond arrest can be achieved or not. As this very behaviour has been reported by other works in the literature, we suggest that it should be treated as a distinctive feature of disbond arrest in bonded GLARE.

From what was observed in the experiments, the flush-headed bolts resulted in a longer fatigue life compared to the flat-headed ones, which was ascribed to less crack growth in the adherents.

The numerical results showed that a region of influence exists around the bolt, inside which a steep gradient of the strain energy release rate is present. In this zone, the mode I SERR decreases due to the clamping effect of the bolt, while the mode II and mode III SERR increase. This produces a change in the mode-mixity ratio around the hole, which becomes almost pure mode II. On the other hand, the strain energy release rate at some distance from the bolt gets equal to that of a conventional cracked lap shear specimens, as it was confirmed by a comparison with theoretical results.

In the far-field region, a good prediction of the fatigue crack growth could be obtained by combining the strain energy release rate computed according to Brussat's model with Bürger's modification of Paris' law.

The present results evidence that fatigue crack arrest in bonded GLARE involves a balance between adhesive crack retardation and adherent crack onset. This suggests that designing a bolted disbond arrest feature requires an holistic view of the fracture mechanism.

Further research could envisage the use of wide CLS specimens, in order to provide more room for the disbond to grow around the Hi-lok. This would give more information on the extension of the influence region of the bolt, which is needed for the design of joints with multiple DAFs. Moreover, reducing the stress around the Hi-lok would facilitate the measurement of the disbond by postponing adherent cracking.

References

1. U.S. Department of Transportation - Federal Aviation Administration. *Composite Aircraft Structure.* AC20-107B (2009).

2. Kruse, T., Körwien, T., Heckner, S. & Geistbeck, M. *Bonding of CFRP primary aerospace structures - Crackstopping in composite bonded joints under fatigue* in *20th International Conference on Composite Materials* (Copenhagen, 2015).

3. Kruse, T., Körwien, T., Ruzek, R., Hangx, R. & Rans, C. *Fatigue behavior and damage tolerant design of bonded joints for aerospace application on Fiber Metal Laminates and composites* in *29th ICAF Symposium - Nagoya* (2017), 7–9.

4. Lin, K. Y., Richard, L. & Cheung, C. H. E. *Delamination/Disbond Arrest Features in Aircraft Composite Structures* tech. rep. DOT/FAA/TC-18/5 (University of Washington, Seattle, WA, 2018).

5. Hangx, R. *Disbond arrest in fibre metal laminates* Master thesis (Delft University of Technology, 2017).

6. Van Teeseling, I. *Towards the Certification of Bonded Primary Fiber Metal Laminate Joints by Bolted Disbond Arrest Features* Master thesis (Delft University of Technology, 2019). `https : / / repository . tudelft.nl/islandora/object/uuid%7B%5C%%7D3A85b6685a-52c8-4f0f-b05d-9752384a9c1c`.

7. Mouritz, A. P. Review of z-pinned composite laminates. *Composites Part A: Applied Science and Manufacturing* **38,** 2383–2397 (2007).

8. Richard, L. *Delamination Arrest by Fasteners in Aircraft Structures Under Static and Fatigue Loading* PhD thesis (University of Washington, 2017).

9. Richard, L. I., Rodriguez, P. A. & Lin, K. Y. *Analytical study of delamination arrest features in Abaqus FEA* in *SAMPE Conference Proceedings* (Long Beach, CA, 2016).

10. Alderliesten, R. *Fatigue Crack Propagation and Delamination Growth in Glare* PhD thesis (Technische Universiteit Delft, 2005). `https : / / repository.tudelft.nl/islandora/object/uuid%7B%5C%%7D3A15006e44-1232-4ef2-87bd-776b249d61f5`.

11. Bickford, J. H. *Introduction to the Design and Behavior of Bolted Joints* `https : / / www . taylorfrancis . com / books / 9780849381874` (CRC Press, 2007).

12. Brussat, T., Chiu, S. & Mostovoy, S. *Fracture Mechanics for Structural Adhesive Bonds - Final Report* tech. rep. AFML-TR-77-163 (Air Force Materials Laboratory, Wright-Patterson AFB, Ohio, 1977).

13. Johnson, W. Stress Analysis of the Cracked-Lap-Shear Specimen: An ASTM Round-Robin. *Journal of Testing and Evaluation* **15,** 303–324 (1987).

14. Bürger, D. *Mixed-mode fatigue disbond on metallic bonded joints.* PhD thesis (Delft University of Technology, 2015). `http://dx.doi.org/10.4233/uuid:ec4dbcd6-052d-4009-bf9e-cdcbf4614174`.

15. Rybicki, E. F. & Kanninen, M. F. A finite element calculation of stress intensity factors by a modified crack closure integral. *Engineering Fracture Mechanics* **9,** 931–938 (1977).

16. Krueger, R. Virtual crack closure technique: History, approach, and applications. *Applied Mechanics Reviews* **57,** 109–143 (2004).

Chapter 5

Conclusions

In this work, several aspects of fatigue crack growth in adhesive bonds were addressed.

Where possible, we tried to put the fatigue phenomenon into a physical perspective, as it was done for the effect of adhesive thickness on fatigue crack growth.

For the specimens tested in this work, increasing the adhesive thickness resulted in an increase of the crack growth rate. By analysing the driving forces of fatigue crack growth and those which resist to it, it turned out that the crack growth resistance (energy dissipation per unit crack growth) is not affected by changing the adhesive thickness. On the other hand, the energy available for crack growth increases when the adhesive thickness is increased. As a result, increased crack growth rate occurs in a thicker adhesive.

The numerical results confirmed that varying the adhesive thickness does not affect the resistance to crack growth. However, more plastic dissipation was computed in thicker specimens. Thus, we hypothesised that this plastic deformation promotes the formation of micro-cracks around the crack tip, which would explain the increased crack growth and the creation of secondary cracks observed in thicker adhesives.

The results suggest that the effect of adhesive thickness is most likely material-dependant. This should therefore be taken in due consideration when applying the results observed in one adhesive to a different material.

Cohesive zone models proved a useful tool to compute quasi-static crack growth in mode I and mode II. By comparing experimental and numerical results, the double cantilever beam model was shown to give an accurate estimate of the crack growth and of the strain energy release rate. On the other hand, the end-notched flexure model only gave reasonable results for short cracks, while the computed SERR value was underestimated for longer cracks, which was hypothesised to be related to the unstable crack growth

observed in mode II.

Upon observation that the numerical results can be indeed affected by the technique used to stabilize the solution, the effect of viscous regularization was investigated. The viscous solution was shown to differ from the inviscid one. In particular, the constitutive relationship of the cohesive model is directly affected by viscosity. For high values of viscosity, unexpectedly high values of the fracture energy were observed. This produced an artificial stiffening which results in underestimation of the crack growth.

A proof of the convergence of the viscous solution was derived, together with an estimate of the error. Accordingly, it was shown that the value of viscosity must be kept low in order to obtain consistent results.

Finally, the influence of a disbond arrest feature on fatigue crack growth in bonded GLARE was investigated. The effect of bolt geometry was evaluated by comparing flush-headed Hi-loks to flat-headed ones.

For the specimens tested in this research, a moderate decrease of the crack growth rate was observed near the bolt. Since the decreased crack growth was accompanied by cracking of the aluminium plies, it could not be assessed whether complete disbond arrest can be achieved or not.

From what was observed in the experiments, the flush-headed rivets resulted in a longer fatigue life compared to the flat-headed ones, which was ascribed to postponed crack growth in the adherents.

The numerical results showed that the influence of the bolt extends in a small region around it. In this zone, the strain energy release rate changes substantially. Thus, a different mode-mix is attained around the bolt, which resembles pure mode II loading. Outside of the region of influence, a good prediction of the fatigue crack growth could be obtained by combining the strain energy release rate computed according to Brussat's theoretical model with Bürger's modification of Paris' law.

The present results show that fatigue crack arrest in bonded GLARE involves a balance between reduction of adhesive crack growth and cracking of the adherent. Further research should aim to better understand this mechanism and define useful criteria for the design of a bolted disbond arrest feature.

Appendix A

Convergence of Abaqus' viscous solution

In the following we will propose a proof of the convergence of the viscous solution to the inviscid one for Abaqus' viscous regularization scheme [1]. An error estimate is also derived from the expression of the viscous solution.

Let consider the differential equation which defines the damage in the viscous solution, i.e. Equation (3.10):

$$\frac{\mathrm{d}D_\mu}{\mathrm{d}t} = \frac{1}{\mu}\left(D - D_\mu\right) \tag{A.1}$$

The viscous solution tends to the inviscid one if $D_\mu \to D$ as $\frac{t}{\mu} \to \infty$.

In general, damage can be regarded as a continuous function $D\colon [\delta_e^0, \delta_e^c] \to [0, 1]$. The expression of $D = D(\delta_e)$ depends on the specific form of the traction-separation law. From the irreversibility of damage, it follows that $\frac{\mathrm{d}D}{\mathrm{d}t} \geq 0$, i.e. damage is a non-decreasing function of time. Specifically, let separation be a continuous function $\delta_e\colon [t_0, t_c] \to [\delta_e^0, \delta_e^c]$; we denote as t_0, t_c the time instants corresponding to separations δ_e^0 and δ_e^c respectively. Hence, it follows:

$$D\colon [t_0, t_c] \to [0, 1] \tag{A.2}$$

For most practical cases we can assume that the damage increase is sufficiently smooth, i.e. $D \in C^1([t_0, t_c])$. In the following we will use the dot notation for derivatives with respect to time.

The solution of Equation (A.1) is in the form:

$$D_\mu = \frac{e^{-\frac{t}{\mu}}}{\mu} \int_{t_0}^{t} D e^{\frac{\tau}{\mu}}\, d\tau \tag{A.3}$$

107

We can write the following:

$$\frac{1}{\mu} \int_{t_0}^{t} D e^{\frac{\tau}{\mu}} \, d\tau = \left[D e^{\frac{\tau}{\mu}} \right]_{t_0}^{t} - \int_{t_0}^{t} \dot{D} e^{\frac{\tau}{\mu}} \, d\tau \tag{A.4}$$

Since $\dot{D} \geq 0$, the integral in the right-hand side of Equation (A.4) is non-negative. Moreover, using Cauchy-Schwarz inequality:

$$\left| \int_{t_0}^{t} \dot{D} e^{\frac{\tau}{\mu}} \, d\tau \right|^2 \leq \int_{t_0}^{t} |\dot{D}|^2 \, d\tau \cdot \int_{t_0}^{t} |e^{\frac{\tau}{\mu}}|^2 \, d\tau$$

$$\int_{t_0}^{t} \dot{D} e^{\frac{\tau}{\mu}} \, d\tau \leq \left[\int_{t_0}^{t} \dot{D}^2 \, d\tau \right]^{\frac{1}{2}} \cdot \left[\int_{t_0}^{t} e^{2\frac{\tau}{\mu}} \, d\tau \right]^{\frac{1}{2}}$$

Hence we derive:

$$0 \leq e^{-\frac{t}{\mu}} \int_{t_0}^{t} \dot{D} e^{\frac{\tau}{\mu}} \, d\tau \leq \mu^{\frac{1}{2}} \left[1 - e^{2\frac{t_0-t}{\mu}} \right]^{\frac{1}{2}} \left[\frac{1}{2} \int_{t_0}^{t} \dot{D}^2 \, d\tau \right]^{\frac{1}{2}}$$

$$0 \leq e^{-\frac{t}{\mu}} \int_{t_0}^{t} \dot{D} e^{\frac{\tau}{\mu}} \, d\tau \leq \mu^{\frac{1}{2}} \left[1 - e^{2\frac{t_0-t}{\mu}} \right]^{\frac{1}{2}} \varepsilon_D \tag{A.5}$$

where ε_D is a finite, non-negative constant (with respect to μ) and can be computed knowing the specific form of the traction-separation law.

Together, (A.3), (A.4) and (A.5) result in the inequality:

$$D \left[1 - e^{\frac{t_0-t}{\mu}} \right] - \mu^{\frac{1}{2}} \left[1 - e^{2\frac{t_0-t}{\mu}} \right]^{\frac{1}{2}} \varepsilon_D \leq D_\mu \leq D \left[1 - e^{\frac{t_0-t}{\mu}} \right] \tag{A.6}$$

Letting $\frac{t}{\mu} \to \infty$ gives:

$$D - \mu^{\frac{1}{2}} \varepsilon_D \leq D_\mu \leq D \tag{A.7}$$

We observe that, from Equation (A.2), D is defined only for $t \in [t_0, t_c]$. Hence, $\frac{t}{\mu} \to \infty$ implies $\mu \to 0$. The double inequality (A.7) thus becomes $D_\mu = D$, which concludes our proof.

Inequality (A.6) gives an upper and a lower bound on the value of D_μ. This expression can be used to estimate the error introduced by the viscous regularization scheme compared to the inviscid case.

References

1. Dassault Systèmes. *Abaqus Analysis User's Manual, Version 6.7* (2007). http://130.149.89.49:2080/v6.7/books/usb/default.htm.